A Study of the τ Lepton Polarization in Z^o Decays

Butrus Youkhana Altoon

Department of Physics and Astronomy
The University of Glasgow
Glasgow Scotland

Thesis submitted for the degree of Doctor of Philosophy

September 1991

Abstract

A study is presented of tau polarization observed in the channel $Z^0 \rightarrow \tau^+\tau^-$ and the subsequent tau decay $\tau \rightarrow \pi\nu_\tau$, using the ALEPH detector at the LEP collider at CERN.

The polarization is a result of parity violation in the neutral and charged weak interactions. Experimentally it can be measured from the energy spectrum of the tau decay product. The detector started collecting data in 1989 and the data were taken in a range of energy in the vicinity of the Z^0 pole.

$$P = \frac{\sigma_R^\tau - \sigma_L^\tau}{\sigma_R^\tau + \sigma_L^\tau} = -0.140 \pm 0.070 \pm 0.049 \tag{0.1}$$

Observation of a non-zero polarization confirms that parity is violated in weak interactions, extending its proven existence in neutral weak currents to tau lepton interactions in agreement with the universality of the electroweak theory.

Tau polarization is directly related to the ratio of the vector and axial vector couplings of the tau lepton to Z^0 and hence to the effective electroweak angle

$$sin^2\bar{\theta}_W \ = \ 0.2316 \pm 0.006 \tag{0.2}$$

Using the partial width of the Z^0 decays to the tau lepton measured by this experiment, the τ couplings to the Z^0 were found to be $a_\tau = -0.4969 \pm 0.0173$ and $v_\tau = -0.035 \pm 0.0119$.

Preface

Tau polarization in the decay $Z^0 \rightarrow \tau^+\tau^-$ channel is studied in this work. Z^0 events were collected by the ALEPH detector at the LEP collider at CERN, Geneva. The data collected by the detector were in a range of energy in the vicinity of the Z^0 pole.

Data analysis in the ALEPH Collaboration is achieved through the contribution of many people from various institutes spread all over the world, since the idea of LEP was born. The author's contributions to the experiment include work on the construction and testing of the electromagnetic calorimeter modules built at Glasgow University, as well as the analysis presented here.

The analysis presented in this thesis is the individual work of the author within a team in the ALEPH Collaboration. No portion of this thesis has been submitted in support of an application for another degree or qualification in this University, or any other institution of teaching.

Acknowledgements

In the course of my life in the last three years I met many friends and colleagues, without whose help I would not have come to present this thesis.

Firstly, I thank my family, for their support throughout the years of my studies at Glasgow University, and ask their forgiveness for any hard time they passed through especially my daughter Noor.

It is my pleasure to thank my supervisor Ken Smith, for his teaching and supervision during the period of this work. I thank the Physics Department of Glasgow University under the direction of Professors Hughes and Ferrier, for providing me with the opportunity to undertake this this research. I would like to thank the leaders of Glasgow High Energy Physics group Professors I.Skillicorn and D.Saxon, for their support, interest and encouragement.

I would like to thank the Iraqi Ministry of Higher Education for financial support. Also my thanks go to Glasgow University for enrolling the Iraqi students last year following the Gulf crisis, although some of their letters gave us a hard time and diverted my mind from the original cause of being a student.

I would like to thank the members of the tau group-in particular I would like to express my gratitude to Steve Snow. Thanks to the staff of Rutherford Appleton Laboratory and CERN for their assistance in carrying out this research. I would like to thank all the members of the High Energy Physics group at Glasgow, in particular BIG Stan for his computing advice and assistance and I. Knowles for reading the theory part of this thesis and for his helpful comments. During my studies I enjoyed the friendship of Owen, Andy, Ingrid, John and Simon. I would like to thank Alan Flavell, David Martin and the staff of the computing system for their excellent help and support. Also I would like to thank the department administration for their support during the period of my work, especially Catherine McIntyre and Linda McLaughlin.

Finally, I would like to thank my wife and children to whom I dedicate this work.

Above all, thanks to God to whom I believe we owe our existence.

Contents

Chapter 1

A Theoretical Review of Electroweak Interactions

1.1 Introduction

In the last two centuries physicists around the world have reached a wide ranging understanding of the universe both from probing into very long distances in the universe and from the study of the tiny structure of elementary particles. Whereas about five centuries ago Galileo Galilei was investigating the force of gravity on matter through freely falling bodies, today's scientists are building large accelerators accompanied by huge detectors to study internal structure of the matter. The study of the ultimate constituents of matter and the nature of the interaction between them is the principle purpose of High Energy Physics. Through the study of the behaviour of matter at very short distance scales the ultimate constituents of matter can be determined and the force between them discovered. To probe into such distance scales and to be able to produce heavy elementary particles, high energies are necessary.

The elegant unification of electric and magnetic theories into the theory of electromagnetism by James Clerk Maxwell in 1867 was the basis for a new understanding of light and the beginning of new physics. This theory, in which light was described as an electromagnetic wave subsequently led to the discovery of the other parts of the electromagnetic spectrum. The failure to detect the medium needed for wave propagation led Einstein to propose the theory of special relativity. These developments in theoretical physics were accompanied by experimental discoveries including natural radioactivity, X-radiation, the electron and Rutherford's nuclear atom. The revolutionary quantum theory of Planck grew to its maturity in the quantum mechanics of Bohr, Schrödinger and Heisenberg, aimed at describing the nuclear atom. Dirac laid the foundations of quantum field theory by combining Einstein's ideas of relativity and the quantum theory.

The present knowledge of elementary particles starts from the discovery of the electron, proton, neutron, neutrino, and the electromagnetic field quantum (the photon). Results from high energy physics experiments over the last 30-40 years now lead us to believe that the physical world consists of two types of fundamental fermions, (particles with half odd integral spin), called leptons and quarks, which are point-like on a scale of $10^{-17}m$. The leptons are the electron and its heavier partners, the muon and the tau and their associated neutrinos which are electrically neutral, and have very small or zero rest mass. The quarks, which carry fractional electric charge,were introduced from symmetry principles to explain the structure of the large number of experimentally observed hadrons, (strongly interacting particles). The immediate success of the quark model was theoretical in nature, but evidence on the physical properties of the quarks comes from the deep inelastic electron proton scattering experiments carried out at SLAC[1]. The experimental results indicate the existence of substructure in the proton. Further evidence comes from jet formation in e^+e^- interactions. Members of the three symmetry generations of quark and lepton families are listed in table 1.1 below. Each particle has an antiparticle, identical to the particle except for the reversal of their quantum numbers. According to quantum

Type	Particle name	Symbol	Spin	Charge	Baryon Number	Lepton Number
Quarks	up, charm, top	u, c, t	$\frac{1}{2}$	$+\frac{2}{3}$	$\frac{2}{3}$	0
	down, strange, beauty	d, s, b	$\frac{1}{2}$	$-\frac{1}{3}$	$\frac{1}{3}$	0
Leptons	electron, muon, tau	e, μ, τ	$\frac{1}{2}$	-1	0	1
	lepton neutrinos	ν_e, ν_μ, ν_τ	$\frac{1}{2}$	0	0	1
Gauge Bosons	photon	γ	1	0	0	0
	weak bosons	$W^\pm, Z^0$	1	$\pm 1, 0$	0	0
	gluons	$g_i\,(i = 1\ldots 8)$	1	0	0	0
	Higgs	H	0	0	0	0

Table 1.1: Elementary particles in the Standard Model

field theory, all the forces in nature are a result of particle exchange. It is believed that the quark and lepton interactions are governed by four forces. The electromagnetic force describes the interactions of electrically charged particles, the weak force describes interactions like β-decay and μ-decay, the strong force describes how quarks interact and the gravitational force governs how the masses interact.

The theory of quantum electrodynamics(QED) is concerned with the electromagnetic interactions. The validity of QED was established through measurements of the anomalous magnetic moment of the electron and muon and the measurement of the photon mass. For example the anomalous magnetic moment of the electron has been measured to an accuracy of better than one part in 10^{10}[2] and is in good agreement with the QED predictions[3]. QED is based on a U(1) gauge group described in section 1.5, so that the theory is invariant under phase transformations. It is a renormalizable theory and this is related to the fact that the coupling constant is dimensionless and that the photon is massless. Ideas of renormalization as a way of dealing with infinities in the theory were taken as a basis for the development of other physical theories.

The theory of quantum chromodynamics(QCD) describes the strong or "colour" force which governs the quark interactions. The concept of colour as an extra quantum number was introduced to solve the problem of violation of the Pauli principle by the need for three identical u quarks in the ground state of the Δ^{++} baryon. The quantum number gives an extra degree of freedom to the quarks so that the three quarks are no longer identical. Each quark is given three colour states, red, green and blue. The combination of colour and anticolour or of the three complementary colours gives colour neutral states.

QCD is a gauge theory similar to QED in certain aspects but not identical to it. It describes the interactions between the quarks via the exchange of massless gluons. Colour in QCD plays a similar role to that of charge in QED. Gluons themselves carry a colour charge, and can interact directly with other gluons. This possibility is not available in QED, as the photon does not have an electric charge. QCD is a non-abelian gauge theory with SU(3) symmetry. This means that there are eight gluons. Colour objects are strongly bound into colourless states by the gluons so that they cannot exist as free entities. The colour force is the strongest force, having a coupling strength (α_s), the equivalent of the fine structure constant in QED, which is not constant but increases as the distance between the charges increases. It is believed that the confinement of the quarks is related to this behaviour. The fine structure constant also changes with the scale, but in the opposite way to (α_s).

The gravitational force is much weaker than the weak force and hence is not an important effect in particle physics at accelerator energies.

1.2 Weak Decays and Gauge Theories

The original model for the weak interaction of β-decay, proposed by Fermi [7], was based on the interaction between two vector currents. The model later failed to explain the experimental observation of non-conservation of parity in weak decays[8]. The developments in the field of gauge theories in the late sixties led to a successful unification of electromagnetism with the weak interaction into the Weinberg-Salam-Glashow electroweak theory now known as the "Standard Model"[6]. It is also believed that QCD interactions can be described. The GSW model, a gauge theory with $SU(2) \times U(1)$ symmetry and two corresponding couplings (g and g'), is described in section 1.5. The weak interaction is mediated by the heavy intermediate bosons W and Z^0. The electroweak theory was supported by the observation of neutral currents in 1974 [4]. The discovery of the W was announced in January 1983, and of the Z^0 five months later [5], with the masses predicted by this theory. As this theory forms the theoretical basis for this thesis it is described in more detail later in this chapter.

1.3 U(1) Gauge Invariance and Electrodynamics

In this section we will describe how local gauge symmetries can be used to generate interactions by introducing massless gauge bosons. These ideas were the cornerstone for the development of the electroweak model to be described later in Section 1.5. Using the U(1) gauge theory, QED, we will try to demonstrate important properties of gauge symmetries. Standard notations have been used in this chapter. A comprehensive description of gauge theories and the Standard Model can be found in[13].

Consider a field $\psi(x)$ described by the Lagrangian density

$$\mathcal{L} = \mathcal{L}(\psi, \partial_\mu \psi) \tag{1.1}$$

(in practice itself often called the Lagrangian). The Lagrangian formulation is based on the " principle of least action" i.e. the Lagrangian satisfies the Euler-Lagrange equations

$$\frac{\partial \mathcal{L}}{\partial \psi} - \partial_\mu \frac{\partial \mathcal{L}}{\partial(\partial_\mu \psi)} = 0 \tag{1.2}$$

The Lagrangian for spin $\frac{1}{2}$ particles is given by

$$\mathcal{L}_o = i\bar{\psi}\gamma^\mu \partial_\mu \psi - m\bar{\psi}\psi \tag{1.3}$$

where $\bar{\psi} = \psi^\dagger \gamma^o$. This can be substituted into equation 2 to give the Dirac equation:

$$(i\gamma^\mu \partial_\mu - m)\psi = 0 \tag{1.4}$$

We are interested in phase transformations of the following type:

$$\psi(x) \rightarrow \psi'(x) = e^{i\alpha}\psi(x) \tag{1.5}$$

where α is real. These are called $U(1)$ field-phase or gauge transformations [$U(1)$ because $e^{i\alpha}$ is a 1×1 unitary matrix]. The quantity α may be constant, in which case the transformation is said to be global, or may vary from point to point in space-time i.e. $\alpha = \alpha(x)$, in which case we have a local gauge transformation. Equation 1.3 invariance under the phase transformation described by equation 1.5 implies a conserved current $\partial_\mu J^\mu = 0$ (Noethers theorem), with the current of the form:

$$J^\mu_{em} = e\bar{\psi}\gamma^\mu \psi \tag{1.6}$$

representing the electromagnetic charge current density of an electron of charge e. The case of a local $U(1)$ gauge transformation, where $\alpha = \alpha(x)$, is more relevant, due to the fact that some physical quantities such as electric charge or colour are conserved in local regions of space. Therefore a more general form of local phase transformation can be obtained from equation 5 as first proposed by Yang and Mills:

$$\psi(x) \rightarrow e^{i\alpha(x)}\psi(x) \tag{1.7}$$

The Lagrangian is no longer invariant under such a local gauge transformation, because the derivative term transforms as:

$$\partial_\mu \psi \;\rightarrow\; e^{i\alpha(x)}\partial_\mu \;+\; ie^{i\alpha(x)}\,\psi\partial_\mu\alpha \tag{1.8}$$

However, invariance may be restored by adding an extra term to the Lagrangian.

$$\mathcal{L}_I \;=\; e\bar{\psi}\gamma^\mu A_\mu\psi \tag{1.9}$$

where A_μ is a vector field satisfying the condition that when $\psi \rightarrow e^{i\alpha}\,\psi$ and $\bar{\psi} \rightarrow e^{-i\alpha}\,\bar{\psi}$, we have:

$$A_\mu \;\rightarrow\; A_\mu \;+\; \frac{1}{e}\partial_\mu\alpha(x) \tag{1.10}$$

so that $\mathcal{L}_o \;+\; \mathcal{L}_I$ is invariant. Of course $\mathcal{L}_I$ is the familiar minimal interaction of electrodynamics and (1.10) is the well-known gauge transformation for the vector potential A_μ. To obtain the full Lagrangian of electrodynamics, a gauge invariant term which describes the radiation itself has to be added:

$$\mathcal{L}_R \;=\; -\frac{1}{4}F_{\mu\nu}F^{\mu\nu} \tag{1.11}$$

where

$$F_{\mu\nu} \;=\; \partial_\mu A_\nu \;-\; \partial_\nu A_\mu \tag{1.12}$$

is the antisymmetric electromagnetic field tensor. Note that equation 1.11 describes a field whose quanta (photons) possess zero mass. If the photon mass m_γ were greater than zero, we would have to add a gauge non-invariant mass term and equation 1.11 would then be:

$$\mathcal{L}_R \;\rightarrow\; -\frac{1}{4}F_{\mu\nu}F^{\mu\nu} \;+\; \frac{1}{2}m^2 A_\mu A^\mu \tag{1.13}$$

which would defeat the purpose for which A_μ was introduced. [This has important repercussions when attempting to form a model of weak interactions where the force is mediated by massive gauge bosons]. Thus the full QED Lagrangian is given by:

$$\mathcal{L}_{QED} \;=\; \bar{\psi}(i\gamma^\mu\partial_\mu \;-\; m)\psi \;+\; e\bar{\psi}\gamma^\mu\psi A_\mu \;-\; \frac{1}{4}F_{\mu\nu}F^{\mu\nu} \tag{1.14}$$

which is invariant under local $U(1)$ gauge transformations provided that $A_\mu \rightarrow A_\mu + \partial_\mu \frac{\alpha}{e}$. That is achieved by replacing ∂_μ by a covariant derivative $\mathcal{D}_\mu$ where $\mathcal{D}_\mu$ transforms under local gauge transformations in the same way :

$$\mathcal{D}_\mu\psi \;=\; e^{i\alpha(x)}\,\mathcal{D}_\mu\psi \tag{1.15}$$

and the covariant derivative of ψ is defined by

$$\mathcal{D}_\mu\psi \;=\; (\partial_\mu \;+\; ieA_\mu)\psi \tag{1.16}$$

Then the QED Lagrangian can be written in a covariant form as:

$$\mathcal{L}_{QED} \;=\; \bar{\psi}\,[i\gamma^\mu\mathcal{D}_\mu \;-\; m]\,\psi \;-\; \frac{1}{4}F_{\mu\nu}F^{\mu\nu} \tag{1.17}$$

The success of the implementation of local gauge invariance in QED was behind the extension of gauge theories to describe weak interactions and their application to Glashow's $SU(2)_L \times U(1)_Y$ gauge group in the electroweak model described in section 1.5.

1.4 Electroweak Interactions

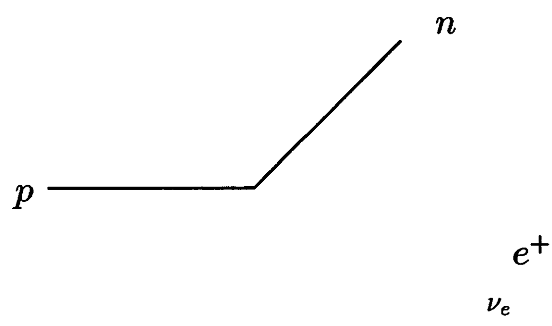

Figure 1.1: β decay in the Fermi model

Weak interactions were first observed in the "slow" process of nuclear β-decay. Although leptons and hadrons experience weak interactions, and hence can undergo weak decays, the latter are often hidden by much more rapid colour or electromagnetic decays.Weak interactions are responsible for pion and muon decays as well as for the beta-decay of atomic nuclei, which involve the transformation of a proton to a neutron (or vice versa). Fermi proposed the first model of the weak interaction inspired by the structure of the electromagnetic interaction[7]. His model was based on the interaction between two vector currents Fig.1.1, $J^+{}_\mu$, $J^-{}_\mu$. For the process

$$n \rightarrow pe^-\bar{\nu}_e \tag{1.18}$$

the invariant amplitude for β-decay is given by

$$\mathcal{M} = G_F J^+{}_\mu J^-{}_\mu. \tag{1.19}$$

where G_F is the weak coupling constant (also known as the Fermi constant), and the currents $J^+{}_\mu$, $J^-{}_\mu$ are defined as:

$$J^-_\mu = \bar{u}_{\nu_e}\gamma_\mu u_e \tag{1.20}$$

$$J^+{}_\mu = \bar{u}_n\gamma^\mu u_p \tag{1.21}$$

where u_n, u_p, u_{ν_e}, and u_e are the Dirac spinors of the particles and γ^μ are the Dirac matrices. In this four particle contact interaction model for the weak interactions Fermi assumed that parity is conserved. The general Lagrangian for β-decay can be written as

$$\mathcal{L}_\beta = \frac{G_F}{\sqrt{2}}\left[\bar{\psi}_p\gamma_\mu\psi_n\bar{\psi}_e\gamma^\mu\psi_{\nu_e} + \bar{\psi}_n\gamma_\mu\psi_p\bar{\psi}_{\nu_e}\gamma^\mu\psi_{\nu_e}\right] \tag{1.22}$$

It was hinted by Fermi and discussed in detail by Gamow and Teller[11] that there is a more general way to construct the β-decay Lagrangian, linear in ψ_p, ψ_n, ψ_e, ψ_{ν_e} and their conjugates and containing no derivatives of these fields, by taking a linear combination of bilinear covariants.

$$\mathcal{L}_\beta = \frac{G_F}{\sqrt{2}}\left[\sum_{j=S,V,T,A,P} \bar{\psi}_p \mathcal{O}_j \psi_n \bar{\psi}_e \mathcal{O}_j \psi_{\bar{\nu}} + h.c.\right] \tag{1.23}$$

where G_F is the Fermi coupling constant and the ψ's are single-particle Dirac spinors. The S, V, T, A, P stand for scalar, vector, tensor, axial and pseudoscalar respectively, and

$$\mathcal{O}_j = 1, \gamma^\mu, \sigma^{\mu\nu}, \gamma^\mu\gamma^5, \gamma^5 \tag{1.24}$$

where γ's are the usual gamma matrices and σ is defined as

$$\sigma^{\mu\nu} = \frac{i}{2}(\gamma^\mu\gamma^\nu - \gamma^\nu\gamma^\mu) \tag{1.25}$$

1.4.1 Parity non-conservation and the V-A current structure

Lee and Yang proposed that parity was not conserved in weak interactions, as a result of the observation of two opposite parity states in decays of particles having the same mass and lifetime[10]. This was confirmed by the direct observation of a forward-backward asymmetry in β-emission from polarized Co^{60} nuclei[8]. An extension of the model by Feynman and Gell-man[9] proposed a V-A form for the weak current. In this form the weak interaction could be described in terms of vector and axial-vector interactions. The Lagrangian above is rewritten as

$$\mathcal{L}_\beta = \frac{G_F}{\sqrt{2}}\left[\bar{\psi}_p\gamma^\mu(C_v - C_a\gamma^5)\psi_n\right]\left[\bar{\psi}_e\gamma_\mu(1 - \gamma^5)\psi_\nu\right] \tag{1.26}$$

where C_v and C_a are constants describing how the hadron current deviates from pure V-A due to strong interaction effects. In this scheme the charged weak current consists of two parts, a leptonic and a hadronic portion. The leptonic part is a straightforward generalization from β-decay which can be written as :

$$\mathcal{J}_l = \sum_{i=e,\mu,\tau,..} \bar{\psi}_i\gamma_\mu(1 - \gamma^5)\psi_{\nu_i} \tag{1.27}$$

which describes transformations of the kind:

$$\nu_l \to l^- \quad \text{and} \quad l^+ \to \bar{\nu}_l \tag{1.28}$$

The hadronic portion for reactions like neutron β-decay which occur because of the quark transformation $d \to u$ can be written as

$$\mathcal{J}_h = \bar{\mathcal{D}}\gamma_\mu(1 - \gamma_5)\mathcal{U} \tag{1.29}$$

where $\mathcal{D}$ and $\mathcal{U}$ are up and down quark field operators, respectively. Strangeness changing decays like $K^+ \rightarrow \mu\nu$, $\Lambda^o \rightarrow p\pi^-$, $\Sigma^- \rightarrow ne^-\bar{\nu}$ ...etc., where ($|\Delta S| = 1$), correspond to a quark transformation of the form $u \rightarrow s$ N. Cabibbo[14] showed that such transformations can be accounted for by assuming that these components enter into the hadronic currents as:

$$\mathcal{J}_h = \bar{\mathcal{D}}_c\gamma_\mu(1 - \gamma_5)\mathcal{U} \tag{1.30}$$

where $\mathcal{D}_c = cos\theta_c\mathcal{D} + sin\theta_c\mathcal{S}$ and $\theta_c \simeq 13^o$ is the "Cabibbo angle". Glashow, Illiopoulos, and Maiani[6] generalized the Cabibbo hypothesis to include the charm quark in what is known as the GIM model. The GIM model forms one of the main bases of the electroweak model to be discussed later in section 5. It is further generalized to take into account six quarks in the Kobayashi-Maskawa model, details of which can be found in[15]. The formulation above includes terms like $(1 - \gamma^5)\psi_\nu$ which allows only left-handed helicity state particles (or right-handed anti particles) to take part in weak interactions. Helicity is defined for a particle having spin $\frac{1}{2}\sigma$ and momentum P as

$$\mathcal{H} = \frac{\sigma \cdot P}{2|P|} \tag{1.31}$$

Weak interactions, where only left-handed neutrinos(or right-handed antineutrinos)take part, are said to be maximally parity violating.

1.4.2 Difficulties of Fermi type theories and the alternatives

The Fermi model described above is still not renormalizable, as various processes at high energy (for example the reaction shown in Fig.1.3 below) lead to a violation of renormalizability. The Fermi constant has the dimensions of $\frac{1}{E^2}$ and the cross section depends on G_F^2. In natural units ($\bar{h} = c = 1$) the total cross section has units of $\frac{1}{E^2}$ and hence we expect:

$$\sigma \propto G_F^2 s \tag{1.32}$$

where s is the centre of mass energy squared.

To absorb these divergences an infinite number of parameters is needed, unlike QED where the divergences are absorbed in the mass and charge terms, when they are replaced by their experimentally measured values, and the wave function renormalization.

1.4.3 The Intermediate Vector Boson model(IVB)

One aproach to the problem of divergence is to assume that the weak interaction is not a four particle contact interaction but is instead mediated by the exchange of a heavy Intermediate Vector Boson (IVB), $W^\pm$, (Fig.1.4) having dimensionless coupling g[12].

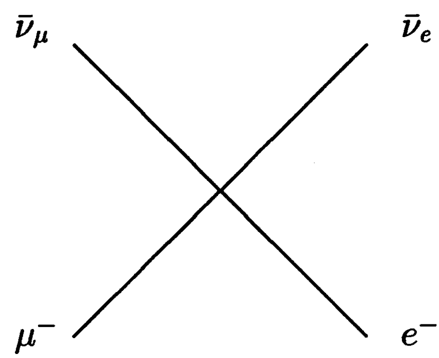

Figure 1.2: The reaction $\bar{\nu}_\mu + \mu^- \rightarrow \bar{\nu}_e + e^-$ in the Fermi model

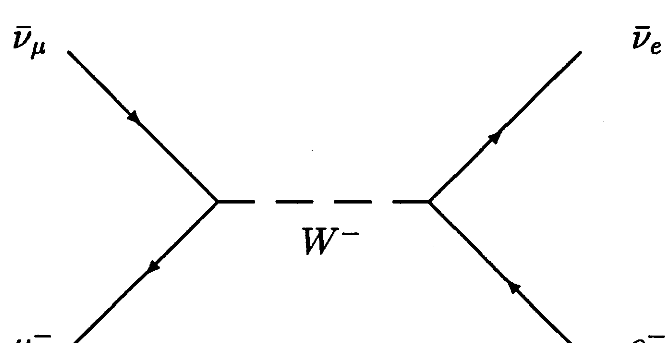

Figure 1.3: The reaction $\bar{\nu}_\mu + \mu^- \rightarrow \bar{\nu}_e + e^-$ via heavy vector boson

According to the scheme proposed by Feynman and Gell-Man[9], the amplitude for the muon decay mode, $\mu^- \rightarrow e^- \nu_\mu \bar{\nu}_e$ is:

$$\mathcal{M} = \frac{G_F}{\sqrt{2}} \bar{u}_e \gamma_\mu (1 - \gamma_5) v_{\nu_e} \bar{u}_{\nu_\mu} \gamma^\mu (1 - \gamma_5) u_\mu \tag{1.33}$$

where u_e,u_μ,u_{ν_μ}, and v_{ν_e} are single-particle Dirac spinors for electron, muon, ν_μ, and $\bar{\nu}_e$, respectively. In the IVB theory, the amplitude instead takes the form

$$\mathcal{M} = -g \bar{u}_e \gamma_\lambda (1 - \gamma_5) v_{\nu_e} \frac{g^{\lambda\sigma} - (\frac{1}{m_W^2}) q^\lambda q^\sigma}{q^2 - m_W^2} g \bar{u}_{\nu_\mu} \gamma^\sigma (1 - \gamma_5) u_\mu \tag{1.34}$$

where $g\gamma_\lambda(1 - \gamma_5)$ is a "semiweak" vertex factor and q the 4 vector momentum transfer (see Fig.1.4) and $g^{\lambda\sigma}$ is the $[4 \times 4]$ metric tensor. For very small momentum transfer $| q^2 | \ll m_W^2$ the amplitude reduces to

$$\mathcal{M} = \left(\frac{g^2}{m_W^2} \right) \bar{u}_e \gamma_\lambda (1 - \gamma_5) v_{\nu_e} \bar{u}_{\nu_\mu} \gamma^\lambda (1 - \gamma_5) u_\mu \tag{1.35}$$

Comparing the amplitudes of IVB and V-A models gives:

$$\frac{G_F}{\sqrt{2}} = \frac{g^2}{8 m_W^2} \tag{1.36}$$

The above formula shows that the weakness of the weak interactions is related to the heavy masses of the IVB. At high energies, then, we expect that the cross-section $\sigma \propto G_F^2 m_W^2$. Higher-order terms in the cross section diverge strongly because of the term proportional to $\frac{1}{m_W^2} q^\lambda q^\sigma$ term in the propagator, so the IVB model like the Fermi theory violates unitarity at high energies and is non-renormalizable. The problem is caused by the $W^\pm$ longitudinal polarization states in interactions such as $\nu_\mu \bar{\nu}_\mu \rightarrow W^+ W^-$. [The corresponding unitarity violation in QED, caused by the photon's longitudinal polarization, did not arise since photons do not have such polarization due to gauge invariance]. The need for a renormalizable theory to describe weak interactions opened the way to the Standard Model of electroweak interactions to be described in section 5.

1.4.4 Neutral currents and the Higgs mechanism

The search for a theory to describe the weak interactions continued and again was inspired by the success of the QED gauge structure. There remained the questions of what gauge group should be used for the theory and of how the gauge bosons acquire masses. Glashow[16] gave the answer to the first question through his development of the $SU(2) \times U(1)$ symmetry. A boson triplet coupling to the weak current can be associated with a $SU(2)_L$ where L denotes that the weak vector bosons only have left-handed coupling and hence retain the V-A structure of the charged weak currents. Since the photon has right as well as left handed coupling, to introduce the photon into the theory for the unification of the weak and electromagnetic interactions Glashow introduced the $U(1)_Y$ group of gauge transformations such that

$$Q = T_3 + \frac{Y}{2} \tag{1.37}$$

where Q is the electric charge, T_3 is the third component of the weak isospin and Y is the weak hypercharge associated with the $U(1)_{em}$, $SU(2)_L$, and the $U(1)_Y$ groups respectively. However, rather than a single unified symmetry group, there are now two groups, each one with an independent coupling strength, so in addition to g for the $SU(2)_L$ another one, the g' for the $U(1)_Y$, is needed to specify fully the electroweak interaction. Four gauge bosons are required for the model to be locally gauge invariant under $SU(2)_L \times U(1)_Y$. W^+, W^- give the charged currents of the weak interactions, the photon the electromagnetic interaction, and finally Z^0 is the weak neutral boson. The gauge symmetries are broken once mass terms are introduced into the Lagrangian.

To generate the particle masses and to incorporate the mass of the weak boson, while retaining renormalisability[16], the Higgs mechanism of spontaneous symmetry breaking is invoked[17]. In a spontaneously broken gauge theory the symmetry is, in a sense, still present; it is merely "hidden" by the choice of ground state about which the field theory is built, which does not possess this symmetry.

The theory can now remain renormalizable. With this mechanism the masses of the gauge fields are generated, (as well as of the fermions), insuring that one of them (the photon) remains massless. It also generates unwanted massless scalar particles, however massless scalars are absorbed under local gauge invariance by the vector bosons, giving them the additional degree of freedom they require to be massive. An additional, massive scalar boson still remains, the "Higgs particle". A curious feature is that, although these Higgs particles are required, no definite prediction is given for their mass, which could be anywhere within the range of 7 to $1000 GeV/c^2$. A natural, worthwhile goal is to search for Higgs bosons, as this is a direct manifestation of the simplest way to cause the $SU(2)_L \times U(1)_Y$ breakdown to $U(1)_{em}$. Such searches are going on at LEP, and have extended the lower limit to the Higgs mass to $\simeq 48 GeV/c^2$.

1.5 The Electroweak Model

On the bases of Glashow's ideas described in section 1.3 and the Higgs mechanism, Weinberg and Salam[6] built their gauge theory to describe the electromagnetic and weak interactions. This handles the divergences encountered in calculations of higher order corrections to a given process, so that sensible answers for these corrections can be obtained. The theory was proved to be renormalizable in 1971 by G. 't Hooft[18]. An essential feature of the new theory in imparting mass to the intermediate bosons is spontaneous symmetry breaking. This, together with local gauge invariance, forms the cornerstone of the theory. The model originally developed by Glashow which successfully describes the weak interactions is based on an $SU(2)_L \times U(1)_Y$ gauge group. Lagrangian invariance introduces the requirement of fermion-gauge boson interactions. The $SU(2)_L$ group contains a boson triplet, where L denotes that that the couplings of the weak bosons are left-handed only and preserve the parity violating V-A structure, hence it describes the interactions of left-handed fermion doublets χ_L

$$\chi_L = \begin{pmatrix} e^- \\ \nu_e \end{pmatrix}_L, \begin{pmatrix} \mu^- \\ \nu_\mu \end{pmatrix}_L, \begin{pmatrix} \tau^- \\ \nu_\tau \end{pmatrix}_L, \begin{pmatrix} u \\ d \end{pmatrix}_L, \begin{pmatrix} c \\ s \end{pmatrix}_L, \begin{pmatrix} t \\ b \end{pmatrix}_L \tag{1.38}$$

via a triplet of fields $W_\mu^{1,2,3,}$ with couplings g. The $U(1)_Y$ group is based on the charge of the fermion and it describes the interactions of the left-handed doublets and the right-handed singlets ψ_R

$$\psi_R = e_R^-, \mu_R^-, \tau_R^-, u_R^-, d_R^-, c_R^-, s_R^-, t_R^-, b_R^- \tag{1.39}$$

via a neutral vector boson B_μ with coupling g'. Extending the local gauge invariance of the $U(1)$ group described in section 1.4, the gauge transformations of the group $SU(2)_L \times U(1)_Y$ can be written as:

$$\begin{aligned} \chi_L \to \chi_L' &= e^{i\alpha(x)\mathbf{T} + i\beta(x)\mathbf{Y}}\chi_L \\ \chi_R \to \chi_R' &= e^{i\beta(x)\mathbf{Y}}\chi_R \end{aligned} \tag{1.40}$$

where $\mathbf{T}$ and $\mathbf{Y}$ are the generators of the two gauge groups respectively. The quantum numbers are assigned such that the charge generator of $U(1)_{em}$ is

$$Q = T_3 + \frac{Y}{2} \tag{1.41}$$

(see section 1.4), so that the electromagnetic current can be recovered from the Lagrangian. Lepton quantum numbers are listed in table 1.2. below. [Imposing $U(1)_{em}$

Lepton	**T**	T_3	Y	Q
ν_e, ν_μ, ν_τ	$\frac{1}{2}$	$\frac{1}{2}$	-1	0
e_L^-, μ_L^-, τ_L^-	$\frac{1}{2}$	$-\frac{1}{2}$	-1	-1
e_R^-, μ_R^-, τ_R^-	0	0	-2	-1

Table 1.2: Electroweak quantum numbers of the leptons

local gauge invariance gives the QED Lagrangian equation (1.17)]. Similarly an electroweak Lagrangian which requires $SU(2)_L \times U(1)_Y$ invariance gives:

$$\begin{aligned} \mathcal{L} = \bar{\chi}_L\gamma^\mu \left[i\partial_\mu - g\mathbf{T}\cdot\mathbf{W}_\mu - g'\frac{Y}{2}B_\mu\right]\chi_L + \bar{\psi}_R\gamma^\mu\left[i\partial_\mu - g'\frac{Y}{2}B_\mu\right]\psi_R \\ - \frac{1}{4}\mathbf{W}_{\mu\nu}\cdot\mathbf{W}^{\mu\nu} - \frac{1}{4}\mathbf{B}_{\mu\nu}\cdot\mathbf{B}^{\mu\nu} \end{aligned} \tag{1.42}$$

The last two terms are the kinetic energy and self-coupling of the W_μ fields which come from a non-abelian $SU(2)$ group:

$$W_{\mu\nu} = \partial_\mu W_\nu - \partial_\nu W_\mu - gW_\mu \times W_\nu \tag{1.43}$$

while the B_μ is like the photon field A_μ, and the tensor $B_{\mu\nu}$ is similar to the tensor $F_{\mu\nu}$ described in section 1.3. g, g' are the fermion couplings to the fields W_μ and B_μ respectively. These two terms result from interactions between the weak vector bosons because the Ws are the gauge bosons of a group where generators do not commute. At this point the theory can be proved to be renormalizable, assuming zero mass for the gauge bosons and fermions. Imparting mass to the Z^0 and $W^\pm$ while keeping the photon massless and the theory renormalizable is achieved by the Higgs mechanism, introducing four real scalar fields ϕ_i which must belong to $SU(2) \times U(1)$ multiplets. The four fields are arranged in a complex doublet with weak hypercharge $Y = 1$:

$$\phi = \frac{1}{\sqrt{2}} \begin{pmatrix} \phi^+\sqrt{2} \\ \phi^o \end{pmatrix} = \frac{1}{\sqrt{2}} \begin{pmatrix} \phi_1 + i\phi_2 \\ v + \phi_3 + i\phi_4 \end{pmatrix} \quad \text{where} \quad \phi_{vac} = \begin{pmatrix} 0 \\ \frac{v}{\sqrt{2}} \end{pmatrix} \tag{1.44}$$

The scalar field ϕ is described by the Lagrangian :

$$\mathcal{L}_H = \left| \left(i\partial_\mu - g\mathbf{T} \cdot \mathbf{W}_\mu - g'\frac{Y}{2}B_\mu \right) \phi \right|^2 + \mu^2(\phi^\dagger\phi) - \lambda(\phi^\dagger\phi)^2 \tag{1.45}$$

which describes a scalar particle, the Higgs boson, with a mass μ and contains the mass term of the vector boson. ϕ_o is the particular vacuum chosen where ϕ_1, ϕ_2, and ϕ_4 are zero and $\phi_3 = \phi_{vac} = v$, where $v = \sqrt{\frac{-\mu^2}{\lambda}}$. Choosing a particular vacuum breaks the symmetry of the Lagrangian and gives the boson mass. Then equation 1.44 can be rewritten in terms of the perturbations about the vacuum

$$\phi(x) = e^{i\theta(\mathrm{x})\cdot\mathbf{T}} \frac{1}{\sqrt{2}} \begin{pmatrix} 0 \\ v + h(x) \end{pmatrix} \tag{1.46}$$

where θ_1, θ_2, θ_3, and h are four real fields. The Lagrangian is locally SU(2) invariant and the field $\theta(x)$ can be gauged away leaving only one massive scalar Higgs field.

Adding the Higgs Lagrangian to the Lagrangian of equation 1.42 would give mass to the bosons, with the mass of the charged boson $W^\pm$ given by

$$M_W = \frac{1}{2}vg \tag{1.47}$$

The physical terms :

$$\begin{aligned} W^+ &= \frac{1}{\sqrt{2}}\left(W_\mu^1 - iW_\mu^2\right) \\ W^- &= \frac{1}{\sqrt{2}}\left(W_\mu^1 + iW_\mu^2\right) \end{aligned} \tag{1.48}$$

result from the substitution of ϕ in the Lagrangian of eq.1.42. The neutral fields Z_μ and A_μ identified with Z^0 and the photon fields respectively result from the linear combination of W_μ and B_μ characterized by the mixing angle θ_W, the " Weinberg angle" :

$$\begin{aligned} A_\mu &= cos\theta_W B_\mu + sin\theta_W W^3_\mu \\ Z_\mu &= cos\theta_W W^3_\mu - sin\theta_W B_\mu \end{aligned} \tag{1.49}$$

where

$$e = g' cos\theta_W = g sin\theta_W \tag{1.50}$$

relates the strength of the weak interactions to the electromagnetic couplings of QED, and

$$M_A = 0 \quad \text{and} \quad M_Z = \frac{1}{2} v \sqrt{g^2 + g'^2} \tag{1.51}$$

The combination of the last two equations gives

$$cos\theta_W = \frac{M_W}{M_Z} \tag{1.52}$$

In a similar way the fermion mass can be given by the Higgs mechanism by introducing another term to the Lagrangian. The quantization of the classical Lagrangian and the extraction of the Feynman rules for the theory are beyond the scope of this thesis: details can be found in[19]. In the reaction $e^+e^- \to \tau^+\tau^-$ and subsequent decay of the τ-lepton, two essential parts of the Lagrangian are relevant to the study of the τ polarization in Z^0 decays, the subject of this thesis. These are the neutral current Lagrangian:

$$\mathcal{L}_{NC} = -e\bar{\psi}\gamma^\mu\psi A_\mu - \frac{g}{cos\theta_W}\bar{\psi}\gamma^\mu \left(\left(1-\gamma^5\right) T_3 - 2Q sin^2\theta_W \right) \psi Z_\mu \tag{1.53}$$

and the charged current Lagrangian which was described briefly in section 1.5. The interaction $e^+e^- \to \tau^+\tau^-$ is mediated at LEP energies mainly by the exchange of a real Z^0 gauge boson while at low energies by photon exchange. The next chapter describes the production of the τ-lepton in e^+e^- interactions, the predictions of the Standard Model and possible tests, including the τ polarization measurement, which currently provides the best test of the electroweak model.

Chapter 2

The Standard Model Physics at LEP

2.1 Electron-Positron Interactions

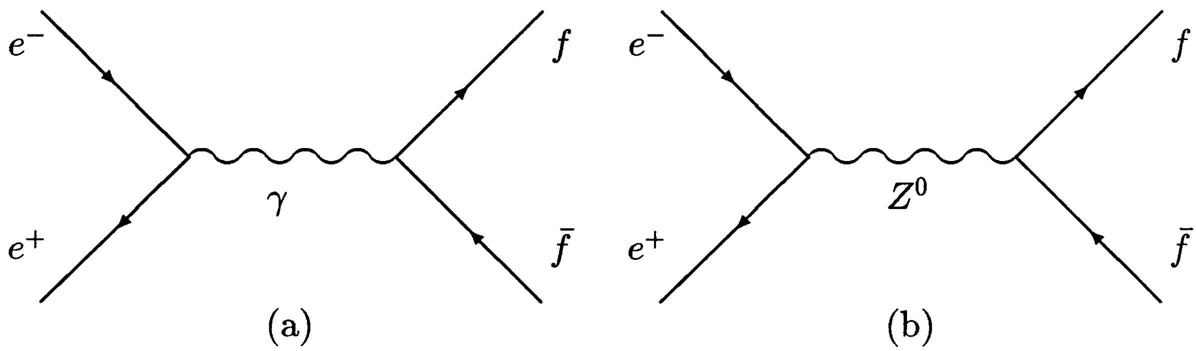

Figure 2.1: Lowest order Feynman diagrams for the reaction $e^+e^- \rightarrow f\bar{f}$.

The process $e^+e^- \rightarrow f\bar{f}$ proceeds at tree level either by photon or Z^0 exchange, Fig.2.1.

The fermion f may be a charged lepton e, μ, or τ ; a neutrino ν_e, ν_μ, or ν_τ; or one of the five quark flavors u, d, s, c, or b. γ exchange dominates at low energy via an electromagnetic process, which is viewed as the formation of a virtual photon which decays into a fermion pair. Particle kinematics are described in Fig.2.2 where θ is the scattering angle between the the incoming electron and the outgoing fermion.

At high energies near the Z^0 resonance, the cross-section locally increases and the process is dominated by the weak interaction through the formation of the Z^0. Many measurements of interference effects between the two diagrams have been performed[20]. At high energies, $s >> M_Z^2$, where s is the centre-of-mass energy, the two diagrams have approximately the same strength.

The energy region $\sqrt{s} = (10 - 40)$ GeV is covered by experiments at PEP, PETRA and TRISTAN. Results from these experiments confirm the validity of QED where the

e^+e^- interactions are mediated by photon exchange. The study of e^+e^- interactions at high energies is of great importance to the confirmation of the electroweak model due to the dominance of Z^0 exchange at such energies.

2.1.1 Production of τ lepton pairs in e^+e^- interactions

At tree level τ lepton pairs can be produced via γ or Z^0 exchange, as shown in Fig.2.1. The calculation of the cross-section for the process requires the propagators and couplings of the photon and Z^0. The vertex factor for the electron is $-ieQ\gamma^\mu$ for particles of charge eQ. Combining equations 1.49 of section 1.5 the vertex factor for the Z^0 couplings to fermions can be derived:

$$Z_\mu = \frac{1}{cos\theta_W}\left(W_\mu^3 - A_\mu sin\theta_W\right) \tag{2.1}$$

Since W_μ^3 of the $SU(2)_L$ couples only to left-handed particles, with coupling constant g one can rewrite the vertex factor as:

$$V = \frac{1}{cos\theta_W}\left(\left(-i\gamma^\mu\left(\frac{1-\gamma^5}{2}\right)gT_3\right) - (-i\gamma_\mu eQ sin\theta_W)\right) \tag{2.2}$$

where $(\frac{1-\gamma^5}{2})$ is the chirality projection operator, and T_3 is the third component of the weak isospin. Using the relationship in equation 1.50 the vertex factor can be written as:

$$V = -\frac{ie}{sin\theta_W cos\theta_W}\gamma^\mu\left(\left(\frac{1-\gamma^5}{2}\right)T_3 - Q sin^2\theta_W\right) \tag{2.3}$$

and in terms of couplings to right and left handed particles as:

$$V = -\frac{ie}{sin\theta_W cos\theta_W}\gamma^\mu\left(g_L\left(\frac{1-\gamma^5}{2}\right) + g_R\left(\frac{1+\gamma^5}{2}\right)\right) \tag{2.4}$$

where

$$\begin{aligned} g_L &= T_3 - Q sin^2\theta_W \\ g_R &= -Q sin^2\theta_W \end{aligned} \tag{2.5}$$

In the Standard Model the vector and axial vector couplings to the Z^0 are defined as follows

$$\begin{aligned} 2v_f &= g_L + g_R = T_3 - 2Q sin^2\theta_W \\ 2a_f &= g_L - g_R = T_3 \end{aligned} \tag{2.6}$$

For negatively charged leptons $T_3 = \frac{1}{2}$ and $Q = 1$, the values of the vector and axial vector couplings for fermions are listed in table 2.1.

Using the photon and Z^0 propagators and the above vertex factors the differential cross-section for fermion pair production at tree level via photon and Z^0 exchange can be derived, ignoring lepton mass terms m_l, giving:

Particle	T_3^f	Q^f	a_f	v_f	$a_f^2 + v_f^2$
ν_e, ν_μ, ν_τ	$+\frac{1}{2}$	0	+1	+1.00	+2.00
e, μ, τ	$-\frac{1}{2}$	−1	−1	−0.08	+1.101
u, c, t	$+\frac{1}{2}$	$+\frac{2}{3}$	+1	+0.39	+1.15
d, s, b	$-\frac{1}{2}$	$-\frac{1}{3}$	−1	−0.69	+1.48

Table 2.1: Summary of the Standard Model couplings ($sin^2\theta_w = 0.230$)

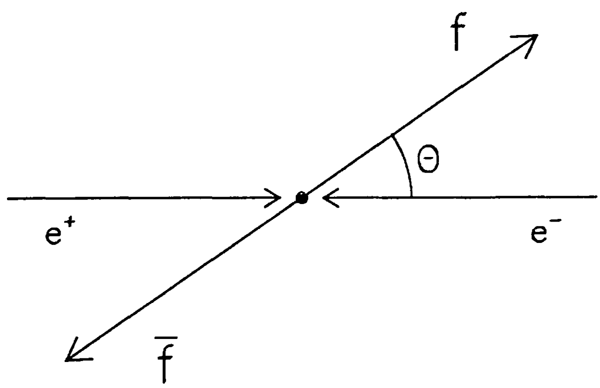

Figure 2.2: Particle kinematics conventions

$$\frac{d\sigma}{d\Omega} = \frac{\alpha^2 N_c^f}{4s}\left[F_1(s)(1 + cos^2\theta) + F_2(s)cos\theta\right] \tag{2.7}$$

$$\begin{aligned} F_1(s) &= Q_e^2 Q_f^2 + 2Q_e Q_f v_e v_f \mathrm{Re}(\chi_0) + \left(a_e^2 + v_e^2\right)\left(a_f^2 + v_f^2\right) \mid \chi_0 \mid^2 \\ F_2(s) &= 4Q_e Q_f a_e a_f \mathrm{Re}(\chi_0) + 8a_e a_f v_e v_f \mid \chi_0 \mid^2 \\ \chi_0 &= s/(s - m_Z^2 + im_Z\Gamma_Z) \end{aligned} \tag{2.8}$$

χ_0 is the Breit-Wigner resonance [66], $\Gamma_Z = \sum_f \Gamma_f$ is the total width of the Z^0, N_c^f is the number of QCD colour degrees of freedom, Q_f and Q_e are the fermion and electron charge respectively, and a_f, v_f are the axial and vector couplings to the intermediate boson.

The first term in $F_1(1)$ is due to pure photon exchange, the last term, which includes $\mid \chi_0 \mid^2$, to pure Z^0 exchange, and the intermediate term is the interference between the two. The cross-section near the Z^0 peak is dominated by the Z^0 exchange $\mid \chi_o \mid^2$ term, while at low energies the first term is dominant and the deviation from QED is only about 1%.

2.1.2 The τ - Lepton

τ-lepton pairs have been detected in e^+e^- interactions for some considerable time[21]. Their most salient features were successfully predicted to a remarkable degree of precision by Y.S.Tsai[22]. They were exhaustively studied theoretically well ahead of their first experimental discovery by M.Perl et al.[22, 23], in the study of e^+e^- interactions at the SPEAR storage ring at SLAC in 1975. The observed events were of the form

$$e^+e^- \rightarrow e^\pm + \mu^\pm + \text{missing energy} \tag{2.9}$$

in which no other charged particles or photons are detected. The only tenable interpretation of such an observation is that a heavy lepton and its antiparticle are being produced. The threshold for tau pair production and decay to electrons and muons was found to be 3.5 GeV, leading to a tau mass of 1.78 GeV/c^2.

The tau decays weakly into an odd number of charged tracks, although decays with more than five charged tracks have not yet been reported. The one charged track topology (B_1) is the sum of the branching ratios of tau decays to leptons, (e and μ's), and the single charged hadronic decays (single charged hadron + neutrals) which includes decays like K, $\pi^\pm$, $\pi^\pm\pi^o$ (via ρ), and $\pi^\pm n\pi^o$ +neutrino. The three and five charged track topology (B_3 and B_5) are composed of charged hadrons (π's and K's) with or without additional neutrals. The 7 prong branching ratio is less than 0.019%, at 90% C.L.[31]. Measurements of the topological branching ratios are listed in table 2.2 below[27]. Discussions are still

1 Prong	3 Prong	5 Prong	Experiment
$84.7 \pm 0.7 \pm 0.8$	$15.2 \pm 0.7 \pm 0.8$	$< 0.5 (95\% C.L.)$	CELLO
$84.7 \pm 1.1 \pm^{1}.6_{1}.3$	$15.3 \pm 1.1 \pm^{+1.3}_{-1.6}$	$< 0.7 (95\% C.L.)$	TASSO
84.7 ± 1.0	15.1 ± 1.0	< 0.3	TPC
$87.9 \pm 0.5 \pm 1.2$	$12.1 \pm 0.5 \pm 1.2$		DELCO
$86.9 \pm 0.2 \pm 0.3$	$13.0 \pm 0.2 \pm 0.3$	0.3 ± 0.04	HRS
$86.1 \pm 0.5 \pm 0.9$	$13.6 \pm 0.5 \pm 0.8$	$0.3 \pm 0.1 \pm 0.2$	JADE
	$13.3 \pm 0.3 \pm 0.6$	< 0.17	MAC
	$12.8 \pm 0.5 \pm 0.8$	$0.16 \pm 0.08 \pm 0.04$	MARK2
$87.8 \pm 1.3 \pm 3.9$	$12.2 \pm 1.3 \pm 3.9$		PLUTO
85.45 ± 0.88	14.35 ± 0.48	0.1 ± 0.05	ALEPH [40]
86.5 ± 0.3	13.4 ± 0.3	0.14 ± 0.04	world average

Table 2.2: Measurements of the percentage topological branching ratios

going on about the 1-prong branching ratio , where the sum of the exclusive branching ratios for exclusive 1 prong final states is less than the topological 1 prong branching ratio. This could be because of a common systematic bias in different experiments or due to the existence of the channel $\tau \rightarrow \nu\pi\eta$[24], as reported by the HRS collaboration[25].

An independent confirmation is needed because the existence of such a channel is of importance due to its violation of the Standard Model expectations. No other information up to now would place the τ lepton outside the standard frame as a third lepton .

The tau neutrino has never been observed, an upper limit to its mass being poorly bounded to some 35 MeV at 95% C.L.[26].

The study of τ-lepton pairs from e^+e^- interactions not only allows the establishment of lepton universality as mentioned above, but also the study of hadronic weak interactions in the semi leptonic decay modes of the τ-lepton. Most important of all it provides a test of the Standard Model of electroweak interactions via measurements of τ- polarization in Z^0 decays, which is the topic of this analysis. More details are given in section 2.3.

2.1.3 The τ - lepton decays

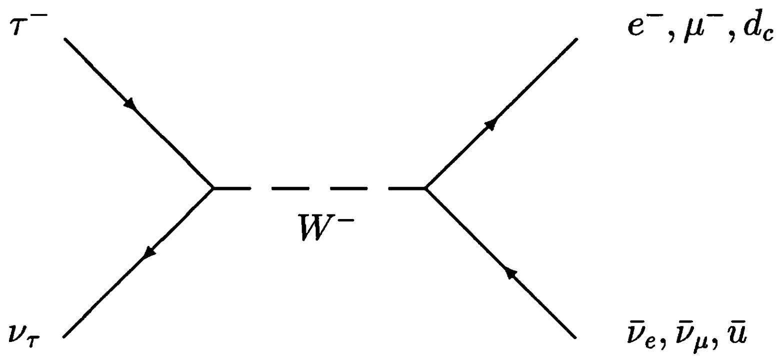

Figure 2.3: First order Feynman diagram for τ decay in the Standard Model

The tau lepton decays via the charged weak interaction into final states with an odd number of charged particles plus neutrals as shown in Fig.2.3, with branching ratios (86.5 $\pm$ 0.3)% into 1 charged track, (13.4 $\pm$ 0.3)% into 3 charged tracks and (0.14 $\pm$ 0.04)% into five charged tracks[27]. The most important tau decay modes are listed in Table 2.3 below. As shown in Fig.2.3 the two distinctive decay types are:

1. **The leptonic decays:** The tau lepton was discovered by the so-called anomalous $\mu - e$ events, in the reaction $e^+e^- \rightarrow \tau^+\tau^-$, in which the μ and e were regarded as the visible part of the subsequent decays $\tau \rightarrow \mu\bar{\nu}_\mu\nu_\tau$ and $\tau \rightarrow e\bar{\nu}_e\nu_\tau$ respectively.

2. **The hadronic decays:** Due to the three quark colours the branching ratios Br($\tau \rightarrow e$):Br($\tau \rightarrow \mu$): Br($\tau \rightarrow$ hadrons) are expected to be approximately in the ratio 1:1:3. The differences in particle masses and final state hadronic decay modes lead to slight deviations from these values.

τ-properties have been extensively studied at more than one experiment, e.g. at DORIS, PETRA, SPEAR and KEK[34] and recently by all four LEP experiments. Some of its properties are already well studied and measured (mass, life time, branching ratios ....), see for example[27, 28, 29]. The current world average for the tau mass τ_m is $(1.784 \pm 0.0032) GeV/c^2$. The current best value for the tau lifetime is $(3.03 \pm 0.08) \times 10^{-13}$ s[30].

Table 2.3 includes preliminary results from the ALEPH detector [40] on exclusive branching ratios, which are compared with the world average and theoretical expectations based on the Standard Model.

Decay channel	ALEPH	World av.	Theor. exp.
$\tau \to e\nu_\tau \bar{\nu}_e$	18.09 ± 0.63	17.9 ± 0.4	18.9 ± 0.5
$\tau \to \nu_\tau \mu \bar{\nu}_\mu$	17.35 ± 0.56	17.8 ± 0.4	18.4
$\tau \to h\,\nu_\tau$	13.32 ± 0.56		
$\tau \to h\,\nu_\tau (K^*$ subtracted)	12.55 ± 0.56	11.6 ± 0.6	12.6
$\tau \to h\,\pi^0$	25.02 ± 1.1		
$\tau \to \pi\pi^0\nu(K^*$ subtracted)	24.56 ± 1.1	22.6 ± 1.1	23.2
$\tau \to h\,2\pi^0\nu$	10.53 ± 1.1		
$h\,2\pi^0(K^*$ and $\pi\omega$ subtracted)	10.23 ± 1.1		
$\tau \to \pi\pi^0\nu_\tau$	9.85 ± 1.1	7.5 ± 0.9	
$\tau \to h\,\nu_\tau \geq 3\pi^o$	1.53 ± 0.61	3.0 ± 2.7	
$\tau \to 3h\,\nu_\tau$	9.49 ± 0.73		
$\tau \to 3\pi\nu_\tau$	8.93 ± 0.75	6.7 ± 0.6	
$\tau \to 3h\ \geq 1\pi^0\nu_\tau$	4.95 ± 0.71	4.6 ± 1.0	
$\tau \to 5\pi \geq 0\pi^0\,\nu_\tau$	0.10 ± 0.05	0.113 ± 0.027	

Table 2.3: Measurements of the exclusive branching ratios of the τ lepton

2.1.4 The decay $\tau \to \pi\nu_\tau$

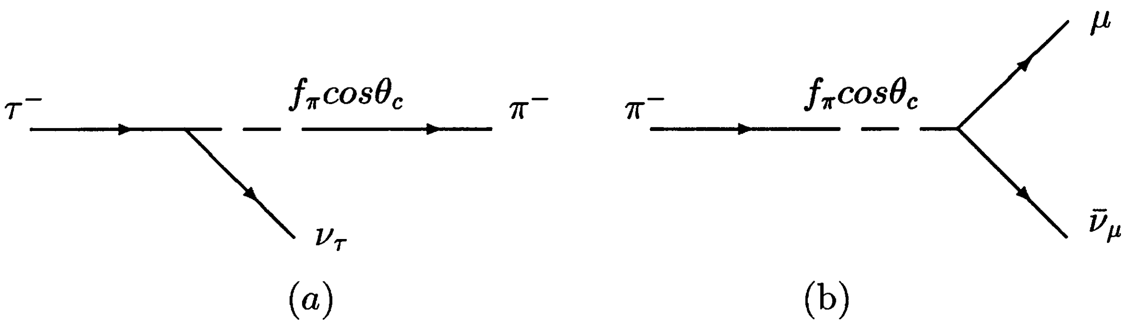

Figure 2.4: Feynman diagram of the decay $\tau \to \nu_\tau\pi$

The decay $\tau \to \pi\nu_\tau$ is the simplest decay mode of the τ-lepton where it decays to a stable hadron and a tau neutrino, via a weak charged current. The intermediate vector bosons involved are the W^+ and W^-. The pion decay constant $f_\pi cos\theta_c$, measuring the strength of the pion coupling of the axial-vector current cannot be derived from the theory, but can be obtained from the decay $\pi \to \mu\nu$ Fig.2.4(b). Taking the reverse process of the diagram in Fig.2.4(b) and replacing the τ charged current by the μ charged current, from the formula for pion decay:

$$\Gamma(\pi \to \mu\bar{\nu_\mu}) = \frac{G_F^2}{8\pi} f_\pi^2 cos^2\theta_c m_\pi m_\mu^2 \left(1 - \frac{m_\mu^2}{m_\pi^2}\right)^2 \tag{2.10}$$

and the measured values for θ_c, Γ_π, the masses of the μ and π and G_F, a value for the pion decay constant can be derived:

$$f_\pi = 0.943 m_\pi \tag{2.11}$$

Then the width for the decay $\tau \to \pi\nu_\tau$ can be obtained using time reversal invariance.

$$\Gamma(\tau \to \pi\nu_\tau) = \frac{G_F^2}{16\pi} f_\pi^2 cos^2\theta_c m_\tau^3 \left(1 - \frac{m_\pi^2}{m_\tau^2}\right)^2 \tag{2.12}$$

Defining R_π as

$$R_\pi = \frac{\Gamma(\tau^- \to \nu_\tau\pi^-)}{\Gamma(\tau^- \to \nu_\tau e^- \bar{\nu_e})} \tag{2.13}$$

then

$$\begin{aligned} R_\pi(\tau \to \pi\nu_\tau) &= \frac{12\pi^2}{m_\tau^2} f_\pi^2 cos^2\theta_c \left(1 - \frac{m_\pi^2}{m_\tau^2}\right)^2 \\ &= 0.601 \end{aligned} \tag{2.14}$$

The branching ratio of the pion decay is

$$\mathrm{Br}(\tau \rightarrow \nu_\tau \pi) = R_\pi \mathrm{Br}(\tau \rightarrow e\nu_\tau \bar{\nu}_e) = 10.6 \pm 0.3\% \tag{2.15}$$

The error is dominated by the branching ratio of the tau into an electron, while the error in R_π is negligibly small. This prediction is in excellent agreement with the results in table 2.3.

2.2 Establishment of the Standard Model

In addition to the high accuracy tests of the SM described below, earlier attempts have been made by many groups to prove the validity of the model, for example through elastic neutrino scattering off electrons and deep inelestic neutral current neutrino scattering in nuclei. The first experiments suffer from a small rate while the latter are less theoretically pristine but have much larger rates. Results from these experiments are compared with those of ALEPH in chapter 7.

In the Standard Model three measurable asymmetries are predicted: the Forward-backward asymmetry (A_{FB}), Left-right asymmetry(A_{LR}), and Polarization asymmetry (A_{pol}).

The forward-backward asymmetry results from the $F_2(s)$ term described in section 2.1.1. It depends strongly on the centre of mass energy and is very small. This asymmetry is relatively less sensitive to the $\tau - Z^0$ coupling constant, hence to $sin^2\theta_W$. All fermions can be used for its measurement although the muon is the best candidate thanks to its clean experimental identification. Some previous measurements of the asymmetry are mentioned below.

The Left-right polarization asymmetry (A_{LR}) is a true parity violating effect due to its linear dependence on the product $v_f a_f$. The measurements of A_{LR} will provide the relative sign of the vector and axial couplings to the Z^0. It is also less dependent on centre of mass energy, so less affected by initial/final state bremsstrahlung interference. The short term disadvantage of the A_{LR} measurements is that the required polarized beams do not yet exist.

The final state longitudinal polarization asymmetry, A_{pol} is similar to the A_{LR} in its linear dependence on the vector coupling, and its slow variation with energy.

A parity violating weak decay, which reacts differently for different spins is an excellent environment for the measurement of the polarization. Since electrons do not decay, they cannot be used. Of the other fermions which can be used, the muons, quarks and taus, the first has a long life time and so needs a giant detector[32]. For the second option the hadronization mechanism is not well known [33], so the best candidate is the tau lepton. In summary, of the SM tests accomplished by measurements of the above asymmetries, the A_{pol} measurement provides the best test of the SM in the short term.

Experiments at SLC and LEP offer an opportunity for precision tests of the electroweak sector of the Standard Model, since at such energies the dominant interaction is the weak interaction due to the production of the Z^0 boson. Some Standard Model tests have already been made using the reaction $e^+e^- \to \tau^+\tau^-$ e.g. at PETRA[20] over a c.m. energy range of (38.3 - 46.8) GeV. Attempts were also made to study the τ-polarization at low energies[34]. The results show that the interference of the photon and the Z^0 pole leads to a substantial forward-backward asymmetry in the differential cross-section of the tau pair although the effect of the Z^0 exchange on the total cross-section is very small, and the total cross section measurements in the above energy range provide a clear test of QED. The forward-backward asymmetry was measured to an accuracy of 2% at PETRA, while the measured value for the polarization reported by the MAC and CELLO Collaborations in previous work are -0.02 ± 0.06 and -0.01 ± 0.22 respectively[34].

The general principle of electroweak tests is to use three well known observables α, G_μ, and M_z as inputs to determine the values of some precisely measurable quantities and compare them with predictions which include $O(\alpha)$ electroweak corrections. Agreement constitutes positive experimental evidence for the validity of the Standard Model (SM) beyond the tree level. Any sizeable discrepancy would provide evidence for new physics, beyond the SM.

2.3 Polarization in τ-lepton decays

A crucial test of the electroweak model is to verify that the interaction of the weak current with the τ lepton is correctly described. A longitudinal polarization of the final state fermions in e^+e^- interactions is predicted by the Standard Model. The polarization is proportional to the product of vector and axial vector couplings of the fermions involved.

The final state polarization of the τ-lepton is a parity violating variable defined by:

$$P = \frac{d\sigma_R - d\sigma_L}{d\sigma_R + d\sigma_L} \tag{2.16}$$

where σ_R and σ_L are the cross-sections for the production of right-handed and left-handed τ-leptons, respectively.

The polarization dependence of the cross-section is[35]

$$\begin{aligned} \frac{d\sigma}{dcos\theta}(s, cos\theta; p) &= (1 + cos^2\theta)F_1(s) + 2cos\theta F_2(s) \\ &+ p\left[(1 + cos^2\theta)F_3(s) + 2cos\theta F_4(s)\right], \end{aligned} \tag{2.17}$$

where p is the the helicity of the τ, and the the form factors are defined as follows

$$\begin{aligned} F_1(s) &= \frac{\pi\alpha^2}{2s}\left(q_e^2 q_\tau^2 + 2Re\chi(s)q_e q_\tau v_e v_\tau + \mid \chi(s) \mid^2 (v_e^2 + a_e^2)(v_\tau^2 + a_\tau^2)\right), \\ F_2(s) &= \frac{\pi\alpha^2}{2s}\left(2Re\chi(s)q_e q_\tau a_e a_\tau + \mid \chi(s) \mid^2 2v_e a_e 2v_\tau a_\tau\right), \\ F_3(s) &= \frac{\pi\alpha^2}{2s}\left(2Re\chi(s)q_e q_\tau v_e a_\tau + \mid \chi(s) \mid^2 (v_e^2 + a_e^2)2v_\tau a_\tau\right), \\ F_4(s) &= \frac{\pi\alpha^2}{2s}\left(2Re\chi(s)q_e q_\tau v_e a_\tau + \mid \chi(s) \mid^2 2v_e a_e(v_\tau^2 + a_\tau^2)\right) \end{aligned} \tag{2.18}$$

and

$$\chi(s) = \frac{s}{s - M_Z^2 + is\Gamma/M_Z}$$

The q_e, v_e, a_e, q_τ, v_τ, and a_τ are the charges and Z^0 coupling constants of the electron and τ, respectively.

The above form factors are directly related to the Born cross section, the τ-polarization asymmetry A_{pol}, and the angular dependence of the τ-polarization asymmetry:

$$P_L(s,\theta) = -\frac{(1 + cos^2\theta)F_3(s) + 2cos\theta F_4(s)}{(1 + cos^2\theta)F_1(s) + 2cos\theta F_2(s)} \tag{2.19}$$

where θ is defined in section 2.1.1.

The angular dependence of the polarization is displayed in Fig.2.5 where it is shown that the τs produced in the forward direction are strongly polarized, while in the backward direction the polarization is small and approaches zero for $\theta = 180^0$. The polarization asymmetry of the τ-lepton is determined by averaging over the polar angle θ of any

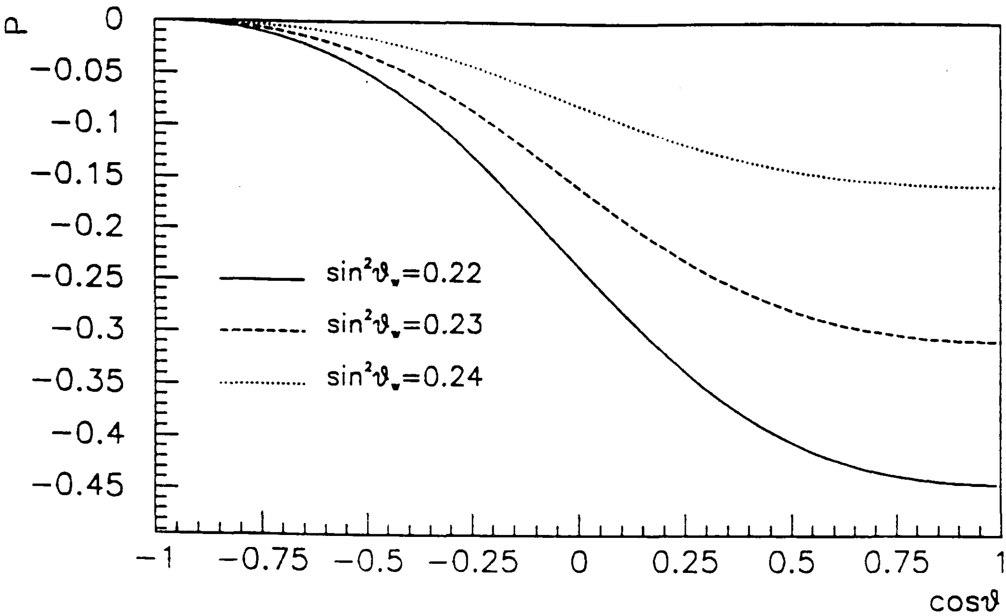

Figure 2.5: Angular dependence of the polarization

forward-backward symmetric detector like ALEPH, for example. The tau angle cannot be determined directly and it has to be estimated from its decay products.

Around the the Z^0 peak, ignoring the contribution of single photon exchange which is very small, the SM predicts an average τ-polarization of

$$\begin{aligned} < P_L > &= -\frac{F_4}{F_2} \\ &= -\frac{2v_\tau a_\tau}{v_\tau^2 + a_\tau^2} = -2\frac{v_\tau / a_\tau}{1 + (v_\tau / a_\tau)^2} \end{aligned} \tag{2.20}$$

where v_τ and a_τ are the axial and vector couplings of the τ. The mean polarization is not sensitive to the mass of the Z^0 as shown in Fig.2.6. It is also clear from the same figure that its dependence on the centre of mass energy is very small near the Z^0 peak, while in Fig.2.7 we can see a stronger dependence of the mean polarization on the value of $sin^2\theta_W$. The ratio v_τ / a_τ in equation 2.20 is related to $sin^2\bar{\theta}_W$ by

$$\frac{v_\tau}{a_\tau} = 1 - 4sin^2\bar{\theta}_W \tag{2.21}$$

$\bar{\theta}_W$ being the effective value of the electroweak mixing angle, which includes the elec-

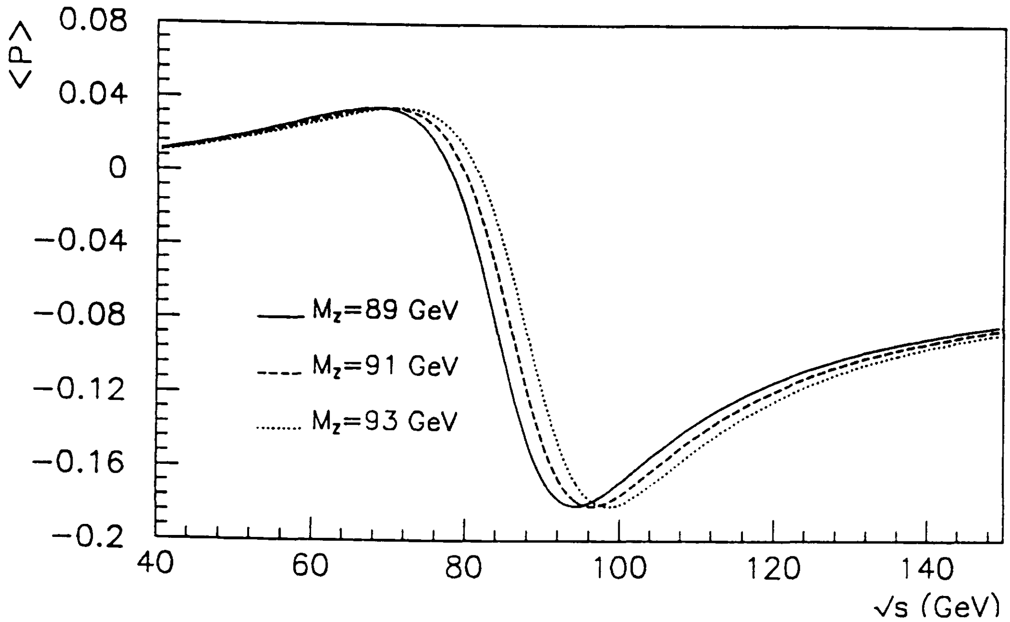

Figure 2.6: Polarization dependence on the Z^0 mass

troweak corrections. For $v_\tau << a_\tau$, the mean polarization can be written as

$$< P > \simeq -2\frac{v_\tau}{a_\tau} = -2(1 - 4sin^2\bar{\theta}_W) \tag{2.22}$$

hence polarization measurements provide direct and precise measurements of $sin^2_{\bar{\theta}_W}$. The average polarization $< P >$, unlike A_{FB}, is independent of the initial state couplings

$$A_{FB}\,|_{\sqrt{s}=M_Z} \simeq \frac{3}{4}\frac{2v_e a_e}{v_e^2 + a_e^2}\frac{2v_\tau a_\tau}{v_\tau^2 + a_\tau^2} \tag{2.23}$$

i.e. A_{FB} is proportional to $v_e a_\tau$. Also the dependence of $< P >$ on $\sqrt{s}$ is very small and accordingly the effect of initial state radiation is very small compared to that in A_{FB}, Fig.2.8.

Experimentally, the way the polarization is measured is by looking at the energy distribution of the decay products of the τ-lepton, since the decay angle of the tau itself is difficult to reconstruct due to the short lifetime of the tau lepton and the missing energy and momenta taken away by the neutrinos. The main emphasis in this analysis will be on the decay $\tau \rightarrow \pi\nu_\tau$, while other decays are mentioned very briefly. In the rest frame of the τ lepton, the decay $\tau^- \rightarrow \pi^-\nu_\tau$ is forbidden for ν's produced along the direction of the tau polarization, as shown in Fig.2.9.

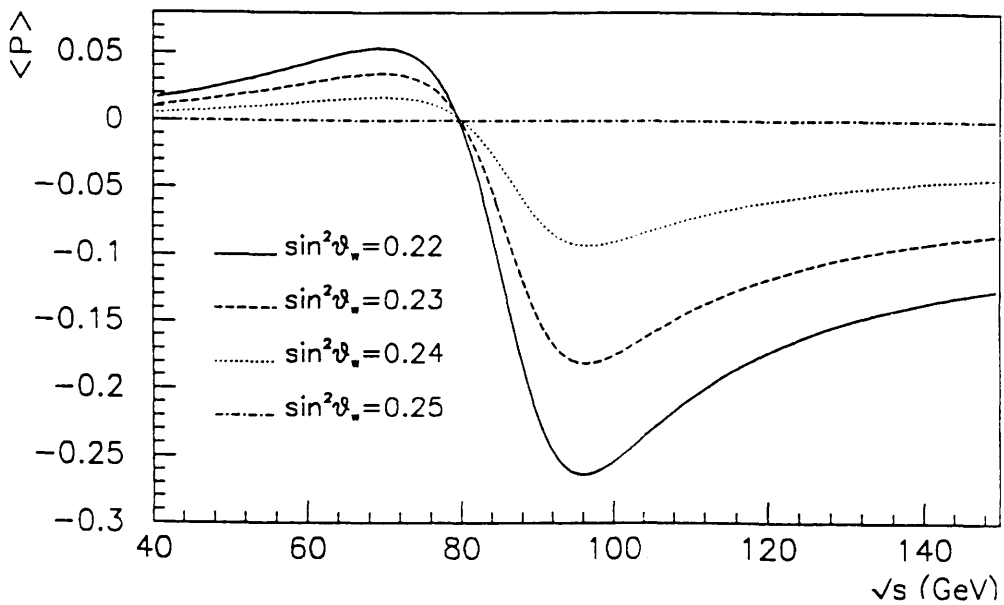

Figure 2.7: Polarization dependence on $sin^2\theta_W$

Assuming the V-A charged current decay structure for the τ, the angular distribution of the emission angle Θ of the $\pi^{\pm}$, Fig.2.10, or $\rho^{\pm}$ with respect to the τ spin direction in the τ rest frame is described by[22]:

$$\frac{1}{N}dN^{\pm} = \frac{1}{2}(1 \pm \alpha P cos\Theta)\, dcos\Theta, \tag{2.24}$$

where α is a measure of the analysis power of the decay, which is related to the spin properties of the decay meson. For spin 0 particles such as the π, $\alpha = 1$,while for spin 1 particles such as ρ and A_1 α is given by

$$\alpha = \frac{m_\tau^2 - 2m_x^2}{m_\tau^2 + 2m_x^2} \tag{2.25}$$

where m_x is the mass of the decay particle.

Since the tau pair helicities are opposite in the final state the emission angles of the decay pions with respect to the $\tau^{\pm}$ flight directions are correlated. This angular correlation leads to positive correlation of the pion laboratory momenta. The angle Θ_π which the pion makes in the τ rest frame, with respect to the τ direction in the laboratory is related to the pion energy by

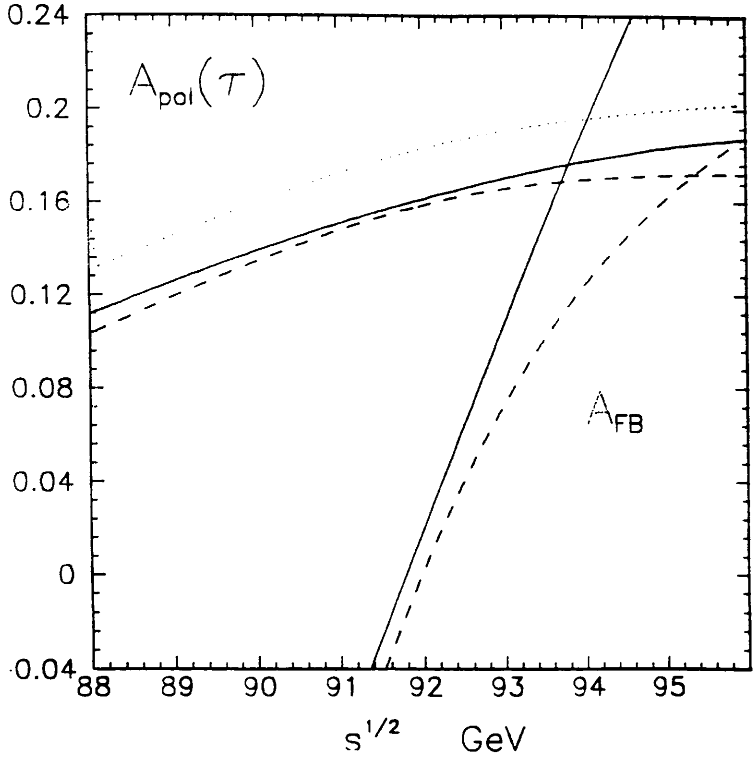

Figure 2.8: Effects of initial state radiation

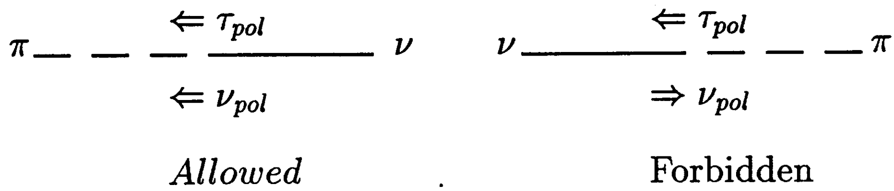

Figure 2.9: Allowed and forbidden configurations in $\tau^- \rightarrow \nu_\tau \pi^-$ decays

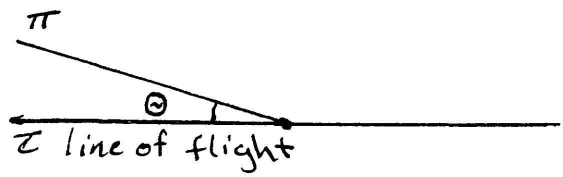

Figure 2.10: Pion angle (Θ_π) with respect to the line of flight

$$x_\pi = \frac{E_\pi}{E_{beam}} = \frac{1}{2}(1 + cos\Theta_\pi) \tag{2.26}$$

By transforming the formula 2.24, appropriately weighted by the two helicity states of the τ^- to account for possible P, to the laboratory system[36]:

$$\frac{1}{N}\frac{dN}{dx_\pi} = 1 + 2\alpha P(x_\pi - \frac{1}{2}) \tag{2.27}$$

The polarization can be determined by measuring the slope of the laboratory energy spectra for the π's and ρ's. In the leptonic decay channels, due to the three-body nature of the decay, the laboratory distributions are more complicated. These are given by

$$\frac{1}{N}\frac{dN}{dx_\pi} = a(x) + Pb(x) \tag{2.28}$$

with[35]

$$\begin{aligned} a(x) &= \frac{1}{3}(5 - 9x^2 + 4x^3) \\ b(x) &= \frac{1}{3}(1 - 9x^2 + 8x^3) \end{aligned} \tag{2.29}$$

Due to the characteristics of the τ lepton pairs at LEP energies, i.e the back-to-back production and CP invariance, both taus have identical spectra and can be used for the purpose of polarization measurements.

2.3.1 Corrections to the first order cross-section

For the measurement of the τ polarization at LEP in the vicinity of the Z^0 peak the Born differential cross-section is used. This was obtained by ignoring the lepton mass terms. Studies of this approximation and of radiative corrections show that they affect the measured polarization value. Such effects are discussed below:

- **Lepton mass effect:** In the derivation of the Born cross-section, neglecting the lepton mass terms which are at most of the order $(2m_\tau/\sqrt{s})$, where s is the centre of mass energy in the e^+e^- interactions, affects the measured value for the tau polarization. The effect is of the order $< 10^{-3}$.

- **QED Corrections:** QED corrections are required for tau polarization measurements in the vicinity of the Z^0 due to initial state and final state bremsstrahlung. These affect the measurements either directly, by changing the spin polarization vector of the tau, or indirectly, by affecting the energy distributions of tau decay products which are used for the extraction of the polarization.

  The corrections to the polarization from initial state photon emission are negligible for two reasons: the weak dependence of the A_{pol} on $\sqrt{s}$ and the smearing of the centre of mass energy close to the top of the Z^0 resonance which is strongly cut off by the Z^0 line shape. The measurements are therefore not affected directly because of both reasons and indirectly (kinematically) due to the second.

  The final state radiation does not affect polarization directly the helicity non-conservation induced by the photon emission being of order $\frac{\alpha}{\pi}A_{pol} \simeq 10^{-4}$[37], but it affects A_{pol} indirectly since the latter is measured from the energy distribution of the decay product. The softening of the energy spectrum by photon emission from the τ prior to its decay or from the decay product, influences the A_{pol} quite significantly. In fact this is the most sizeable effect compared to the other experimental uncertainties.

- **QCD Corrections:** Hadronic QCD corrections to the tau polarization are negligible [38], due to the weak dependence of the A_{pol} on the centre of mass energy, since such effects change the width of Z^0 resonance, hence the initial state bremsstrahlung with negligible influence as mentioned above.

- **Weak Corrections:** These are the most interesting corrections. Heavy particles which cannot be produced directly in the present range of the LEP operating energies, affect all processes through their virtual loop effects in virtual loop diagrams. They depend on the structure of the electroweak model since undiscovered particles give virtual contributions. The corrections depend on all SM parameters, in particular on M_H, M_W and m_t which are not needed in the tree level result. Most parameters are experimentally known except M_H and m_t, while the contribution from M_W can be avoided using the electroweak model relation[39].

$$M_W^2\left(1-\frac{M_W^2}{M_Z^2}\right) = \frac{\pi\alpha}{G_\mu\sqrt{2}}\frac{1}{1-\Delta r} \tag{2.30}$$

  where G_μ is the precisely measured Fermi constant from muon decay. Δr includes corrections to the fine structure constant, α, and depends on m_t and M_H. High precision measurements of the electroweak parameters combined with these corrections will provide an estimate of the masses of particles predicted by the model.

Chapter 3

The Experiment

3.1 The LEP collider

The Large-Electron-Positron(LEP) storage ring is a large octagonal ring with eight straight sections of about 500 metre each, and eight circular sections with a radius of curvature 3300 meters, each of 2840 meters in length Fig.3.1. The ring has a circumference of 26.7 km, and is situated underground in a tunnel with an average diameter of around 4 meters and an average depth of 100 metre. LEP is the largest and highest energy accelerator among the existing e^+e^- storage rings, i.e. Novosibirsk(USSR), Stanford(USA), Hamburg (Ger.), Beijing (China), Cornell(USA) and KEK(Japan). In the LEP magnet ring electrons and positrons circulate in opposite directions with possible head-on collisions at eight points. The beams are kept in orbit by 3400 bending magnets which encompass 19 km of the ring. In addition there are 1902 further focussing correction magnets in the ring. The particles are accelerated at present using conventional RF cavities, which will be replaced by superconducting RF cavities The accelerating system consists of 128 five-cell copper cavities powered by 16 1 Mega-watt klystrons via a complex of wave guides and circulators. The LEP storage ring is the last of five in a chain of accelerators. Positrons are produced by bombarding a tungsten target by 200 MeV electrons from a Linac. The LEP injectors consist of two linacs of 200MeV and 600MeV followed by the Electron-Positron Accumulator(EPA). After accumulating 2×10^{11} positrons per beam in about 11 seconds the beam is then injected into the CERN PS operating as a 3.5 GeV e^+e^- synchrotron. The PS injects into the CERN SPS which operates as a 20 GeV electron-positron injector for LEP. The Proton Synchrotron(PS) and the Super Proton Synchrotron(SPS) are modified to serve this purpose by operating them multimode, using a supercycle which incorporate four cycles of electrons/positrons followed by a cycle of protons. The fact that electrons/positrons are accelerated in the dead time of the proton cycle means that the filling of LEP has had no effect on the 450 GeV SPS stationary target physics which runs in parallel. Electrons and positrons are injected on a 15 second cycle which continuously increases the intensity of the beam bunch up to 2×10^{12} particles; it takes less than 30 minutes for a complete injection into LEP. The two beams are then accelerated to the required energy. Loss of energy due to synchrotron radiation and beam gas interaction reduces the intensity of the beam, and after about 10 to 12 hours a new fill is needed at the present time. During the present operating phase of LEP, the maximum operational

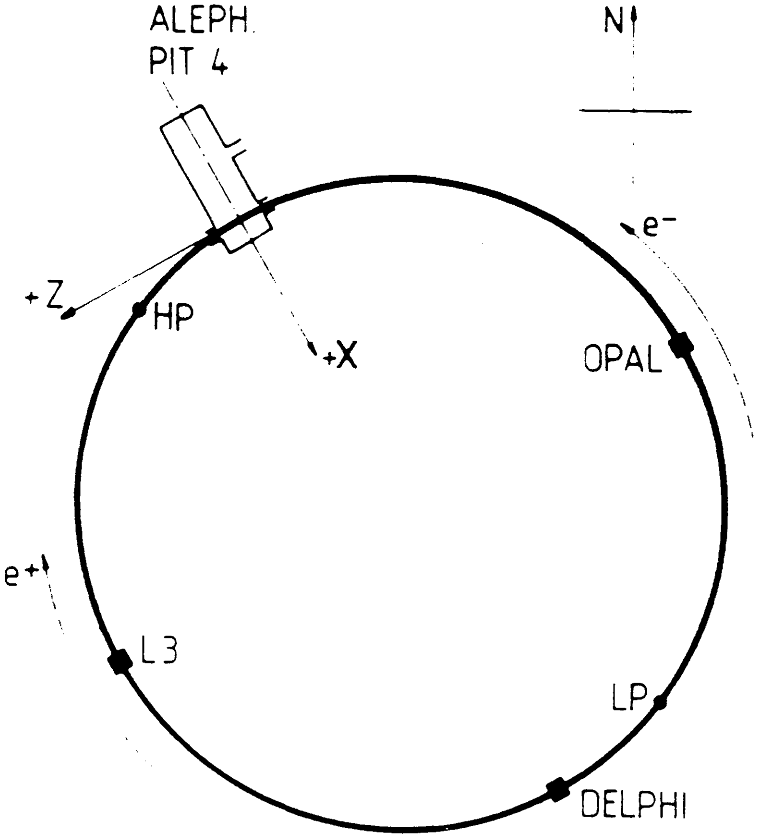

Figure 3.1: Schematic diagram of the LEP Collider.

beam energy is 55 GeV which produces a total C.M. energy of 110GeV with a luminosity of $10^{31}cm^{-2}s^{-1}$, sufficient for the study of e^+e^- interactions around the Z^0 pole. In the second phase of LEP the RF cavities will be replaced by superconducting cavities and the maximum beam energy will reach 2×95 GeV with a luminosity of $10^{32}cm^{-2}s^{-1}$. The motivation behind the construction of the LEP collider was the need to study electroweak interactions, as described in section 2.2. With this aim, four major detectors are located in the middle of four of the straight sections in the LEP ring. These are named ALEPH, L3, OPAL and DELPHI and are installed at the interaction regions 4, 2, 6, and 8 of the LEP ring as shown in Fig.3.1.

All four experiments are provided with an axial magnetic field and have the capability of photon, electron, hadron and muon identification over almost a full 4π solid angle around the interaction point.Different techniques are used in particle identification: for example there is some emphasis on hadron identification in DELPHI through the implementation of Ring Image Cherenkov (RICH) detectors and on lepton identification in L3 by the implementation of a BGO high resolution sampling calorimeter. The OPAL detector is an enhanced version of the JADE detector at PETRA. This has insured a rapid start-up and helped to produce well understood results rather rapidly. Details of the ALEPH detector will be discussed in the next section.

The first injection into the LEP collider took place in July 1989 and on August 13th the first collisions were provided. At the end of the physics run in August 1990 the collider performance had allowed more than 200K Z^0 particles to be detected in the four experiments.

3.2 The ALEPH Detector

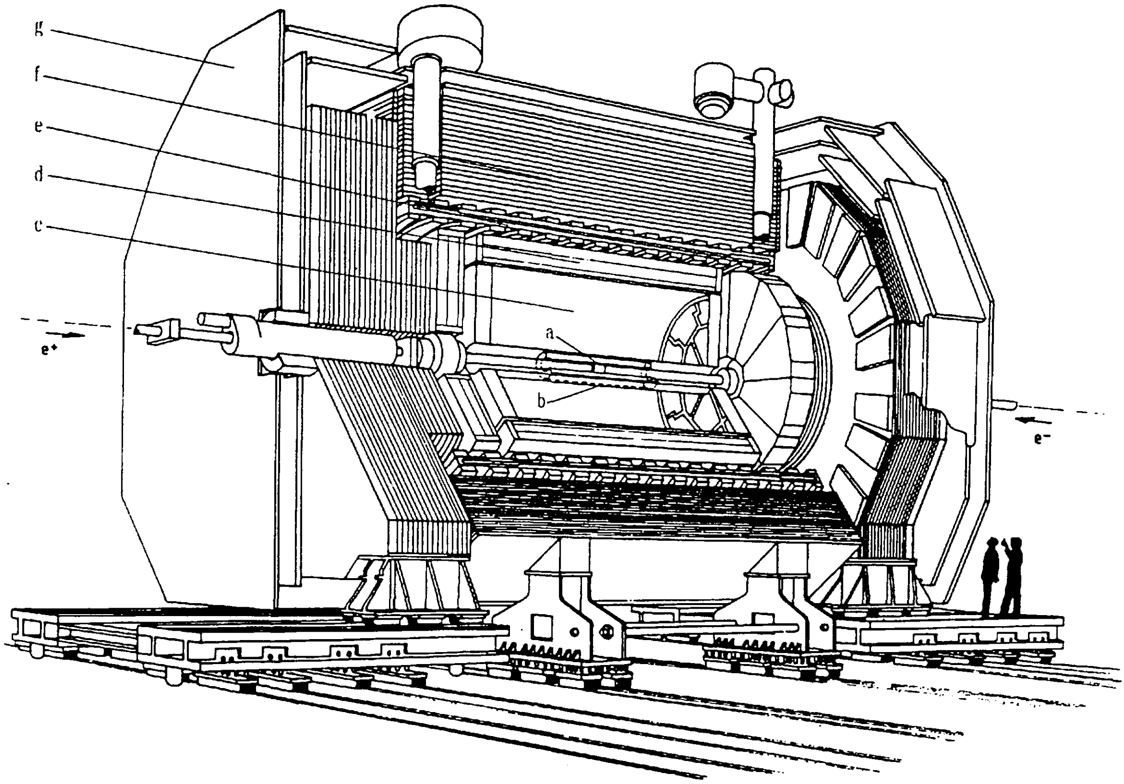

components are labelled as follows : (a) the vertex detector, VDET, (b) the inner tracking chamber, ITC, (c) the time projection chamber, TPC, (d) the electromagnetic calorimeter, ECAL, (e) the superconducting coil, (f) the hadron calorimeter, HCAL, (g) the muon chambers, MUON

Figure 3.2: Cut-away section through the ALEPH detector.

The layout of the ALEPH detector installed in pit 4 of LEP is shown in Fig.3.2. It has a cylindrical shape, 12 m in diameter and 10 m in length, with the axis parallel to the beam line. The ALEPH reference system is defined with the origin at the theoretical interaction point, the positive z-axis along the nominal e-beam direction, the x-axis horizontal and pointing towards the centre of LEP and the y-axis orthogonal to x and z and pointing upwards. The magnetic field is produced by a superconducting solenoid, 5.3 m in diameter and 6.4 m long, which generates an axial magnetic field of 1.5 Tesla. Typical events are complex, with 20 charged particles on average plus a similar number of neutrals, distributed over the entire solid angle. The expected event rate is very low, especially at energies above the Z^0 pole, therefore ALEPH is designed to accumulate for each event as much information over as much of the solid angle as is practical. Of central importance in the detector are the magnetic track detector, designed to permit precise momentum determination of charged secondaries up to the highest energies and the electromagnetic calorimeter with high granularity providing a high spatial resolution, hence good electron identification. Detection is accomplished in consecutive layers, around the beam pipe, starting with the vertex detector used for the location of decay vertices of short lived particles. The Inner Tracking Chamber (ITC) is a multiwire drift chamber providing up to eight r-ϕ points for tracking near the interaction point and is an essential part of the level 1 trigger. The Time Projection Chamber(TPC) is the central tracking chamber of the ALEPH detector. It provides good angular and momentum resolution for charged tracks, and contributes also to particle identification and e-π separation through dE/dx measurements. The TPC together with the ITC provides transverse momentum resolution $\Delta p_T/p_T^2 \simeq 10^{-3}(GeV/c)^{-1}$

The Electromagnetic Calorimeter (ECAL) is a lead/proportional chamber sandwich. It is constructed and read out in 73,728 projective towers, each subdivided into three depth zones.The solenoid has been designed such that, together with the iron yoke, it provides a magnetic field of 1.5 T in the central detector necessary for momentum measurements in the tracking chambers. Outside the solenoid is the Hadron Calorimeter (HCAL). It is an iron/streamer tube sampling calorimeter read out in 4608 projective towers, the iron structure of the calorimeter serving as the main support of the ALEPH detector, the passive part of the HCAL and the return yoke of the magnet. Finally the two double layers of streamer tubes which form the muon chambers are installed outside the iron.

While all the previous parts of the detector serve the purpose of track measurement and identification the luminosity monitors are used to determine the luminosity from the rate of Bhabha events at small scattering angles. For such measurements the Luminosity Calorimeter(LCAL) and the luminosity tracker, the Small Angle Tracking Device(SATR) are installed around the beam pipe. In the following sections, the components of the detector and their performance are discussed more fully.

3.3 The Magnet

The magnet consists of an iron yoke and a solenoid which produces a uniform field parallel to the LEP beam direction and corresponding in uniformity to the requirements of the

TPC.

3.3.1 The Iron Yoke

The iron yoke consists of two parts, the central (barrel) part which is constructed from 24 modules, having a mass of 1680 t and the two end parts, (end-caps) each constructed from 6 modules and having a mass of 450 t. Each of these three parts can be moved individually along the experiment axis. The purpose of the yoke is to shape the longitudinal field, which must be uniform at least in the central region occupied by the TPC, so it is designed to have an axial symmetry. The barrel has a shape of a dodecagonal cylinder, 7.24 m long and 9.37 m wide. The end-caps are shorter, with a length of 1.18 m and a width of 8.7 m. The yoke also accomplishes the function of hadron calorimeter and muon filter. For this the yoke is segmented into 23 slabs of 5 cm thickness except for the outside slab, which is 10 cm thick for mechanical reasons, with 22 mm spacing for the streamer tubes. Being the heaviest and strongest part of the apparatus, it is used as a support for all other elements of the ALEPH detector. The total thickness of the iron used in both the barrel and the end-caps is 120 cm ($7.16\lambda_{abs.}$) at 90^o, but increases to 199 cm at the end of the barrel($\theta = 53^o$). Due to the dodecagonal structure, the overall thickness is modulated in azimuthal angle. moving from 120 cm at the centre of the module to 124 at its edge, after 15^o. The ends of the slabs in each module are soldered to 2.5 cm iron rods. This reduces the sensitive area for full azimuthal angle by 3.4%.

3.3.2 The Superconducting Coil

The solenoid is located between ECAL and HCAL. The solenoid is required to supply the ampere turns with an adequate current distribution for producing, in combination with the laminated iron-yoke structure, a magnetic field of 1.5 T in the central detector with the appropriate field uniformity. A current of 5000 A is needed to provide such a field, and it takes 1h to build up the current. The total energy stored in the magnet is 130 M Joule. Due to the large number of ampere turns ($\simeq 8 \times 10^6$) and the size of the coil, a superconducting winding has been chosen. The conductor used in the coil is made of aluminium around NbTi/Cu. The solenoid with its cryostat weighs 55 tons, and they are located between the electromagnetic and the hadron calorimeters. The solenoid is 7 m long with outer radius 2.92 m and inner radius 2.48 m. The effective thickness of the material used, (coil + cryostat), is $1.6X_o$ and $0.3\lambda_{abs.}$. Another constraint for the mechanical design of the solenoid is the requirement of supporting the central detector and the electromagnetic calorimeter (weight $\simeq$ 130 tonnes) on the inner vacuum tank of the cryostat. The solenoid is cooled in a closed-loop refrigerator and takes 10 days to cool down from 300K to 4.2K. The condition for field homogeneity is expressed as a tolerance on the integral of the radial field component along a line parallel to the beam axis in either half of the TPC, which is 2.2 m long and 3.6 m in diameter. The required condition is

$$\int_0^{220} \frac{B_r}{B_z} dz < 2mm \tag{3.1}$$

The measured field homogeneity is $\frac{\Delta B}{B} = \pm 2 \times 10^{-4}$. This was achieved with more than 900 measuring points inside the magnetic field using Hall probes.

3.4 The Vertex Detector

This kind of detector is used for the location of decay vertices of short-lived particles. It was not fully operational at the beginning of the physics run, so it was not of real interest in the early data and in particular to this analysis. Details of the detector can be found in[41].

3.5 The Inner Tracking Chamber(ITC)

The Inner Tracking Chamber (ITC)[42] has two functions. One is to provide an essential part of the level 1 trigger, the second is to enhance the over-all charged particle tracking of ALEPH, particularly in the critical area close to the beam pipe. A cross-sectional diagram of the detector is shown in Fig.3.3. The chamber is a cylindrical conventional,

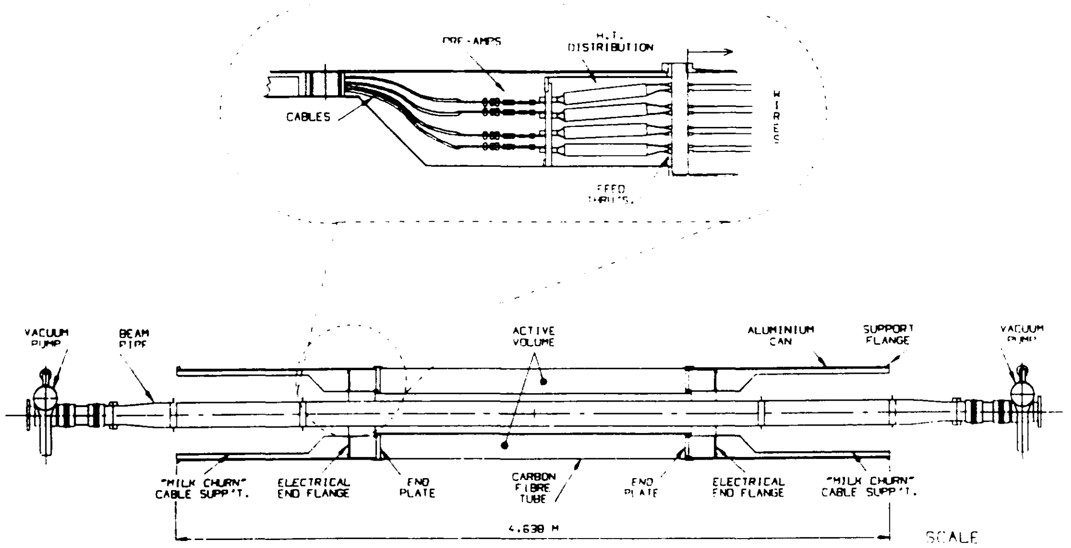

Figure 3.3: Cross-sectional diagram of the ITC.

small cell multiwire drift chamber. The active volume of the chamber is 2m long and 570 mm in diameter. It provides up to 8 accurate r-ϕ points for tracking in the radial region between 160 and 260 mm in radius. This corresponds to an angular acceptance of $-0.97 < cos\theta < +0.97$

The sense wires run parallel to the z (beam) direction. A total of 960 sense wires are strung in 8 concentric layers (96 in each of 4 inner layers, and 144 wires in each of the 4 outer layers), between two aluminium end-plates. Each end-plate has 43 concentric layers of holes,as shown in Fig.3.4, through which the wires are fed . There are 8 sense wire layers , 8 calibration wire layers, and 24 field-wire and 3 guard wire layers. Alternate guard wire holes in the end-plates are left empty to allow gas circulation through the active volume of the chamber. The diameter and quality of the sense wires were chosen so as to give a high gas amplification and to be strong enough to support their own weight over the length of the chamber. To reduce the material used in the tracking volume to the minimum possible amount they have to be light and strong enough to be self supporting. Around each layer of guard wires there is a cage made of 51 hoops of Al wires glued to

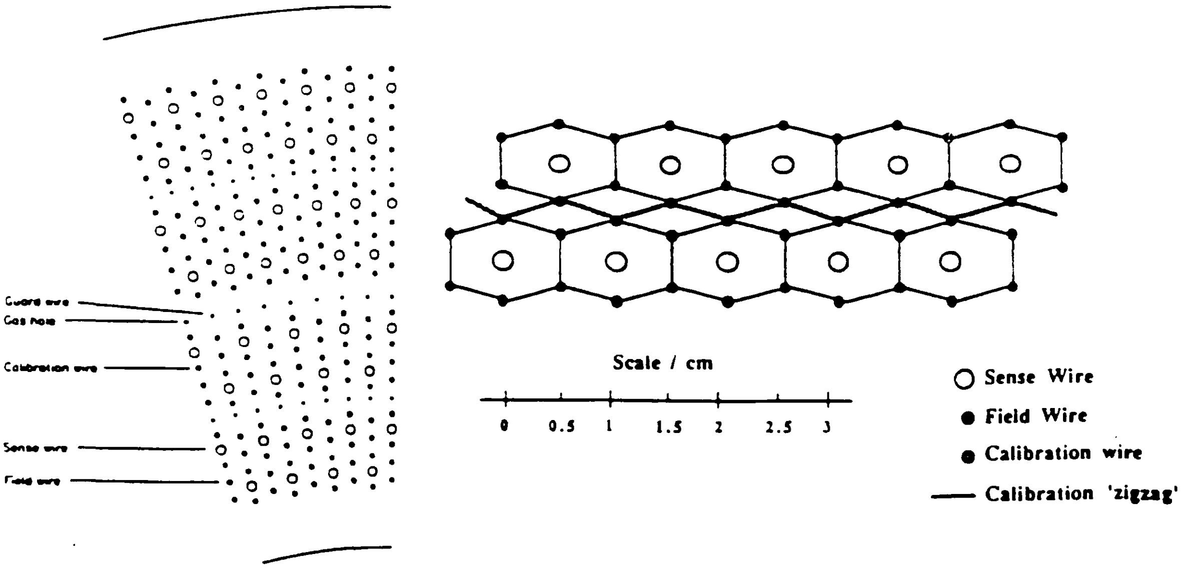

Figure 3.4: Wire cell structure of the ITC.

the guard wires . The cage serves to catch any wires that might break, restricting the damage to one small section of the chamber. Additionally, the high voltage supply is highly segmented so that small groups of cells are able to be switched off independently. A mixture of (50:50) Argone-CO_2 at atmospheric pressure is used to fill the chambers. To prolong the chamber lifetime by inhibiting the formation of polymers and deposition of dirt on the wires small fractions of alcohol or water are added.

The $r - \phi$ coordinates are obtained by measuring the drift time to the sense wires, giving an average precision of $120\mu m$. The z coordinate is found by measuring the difference in the arrival times of pulses at the two ends of each sense wire, with a precision of 3 cm. The drift ITC chambers are hexagonal, formed with a central sense wire surrounded by six field wires Fig.3.4. The sense wires are operated at positive potential in the range (2.0-2.5)kV. The field wires are grounded; one field wire per cell is insulated from the end-plates by a small feed through, and can be used to inject a calibration pulse into the chamber. The remaining field wires are in contact with the end-plates.

3.5.1 The Trigger Processors

Two signals are provided from each sense wire; these signals can be used by the trigger processors. The first, the $r - \phi$ position of the wire hits, is used to search for tracks in radial patterns of wire cells in the $r\phi$ projection.The track is accepted if it gives hits in one cell in four alternative layers and at the junction of two cells in the remaining four layers. The second, (space point processor) still to be installed in ALEPH, is a pulsed output, the arrival time and duration of which represent, respectively, the z-coordinate of the hit and its expected error, providing correlated $r - \phi - z$ information for a fast 3-dimensional track trigger. The track acceptance criteria are the same as for the $r - \phi$ processor and in addition a track candidate must also have all eight hits within a certain $cos\theta$ interval.

3.6 The Time Projection Chamber(TPC)

The TPC is designed to provide good momentum and angular resolution, and it provides good dE/dx measurements for pattern recognition, adding additional resolving power in $e - \pi$ separation to complement the ECAL capability. It is the largest chamber of this kind built so far with an outer diameter of 3.6 m and a length of 4.4 m. The cylindrical structure of the chamber is shown in Fig.3.5. Its axis is parallel to the beam direction and to the magnetic field. It is operated with an Argon-Methane (91 : 9) gas mixture at atmospheric pressure and provides 21 three dimensional coordinates for a fully contained track[47]. The ionization charge is recorded at two end-plates by a system of proportional wire chambers with segmented cathode pad readout. Together with the two cylindrical field cages, they enclose the gas volume of $43m^3$. An end-plate is subdivided into 18 "sectors" of three different types, 6 inner sectors (type K) and 12 outer sectors (type M + W). A striking property of this layout is the radial zig-zag boundary between sectors so that straight tracks never fall completely on the radial boundary, i.e. they are always visible. The most important feature of the end-plate is, however, the arrangement of the pads in 21 concentric circles as shown in Fig.3.6 for 3 dimensional coordinate measurement ($r\phi$ from pad position, and z through drift time). The pads have a radial length of 30 mm and a width of 6.7 mm. The reason behind the choice of long radial pads is the improvement it provides in the $r\phi$ spatial resolution. Each end-plate has a total of 20502 cathode pads and 3168 sense wires. The design of wires and pads is such that up to 21 space points and 320 ionization samples are measured per track. The active area of the end-plate is $\simeq 9m^2$. An electric field of 125 V/cm points from each end-plate towards the central membrane that divides the chamber into two halves either parallel or antiparallel to the magnetic field. Charged particles produce electrons by ionization, electrons drift towards one end-plate, where they induce ionization avalanches in the plane of the wire

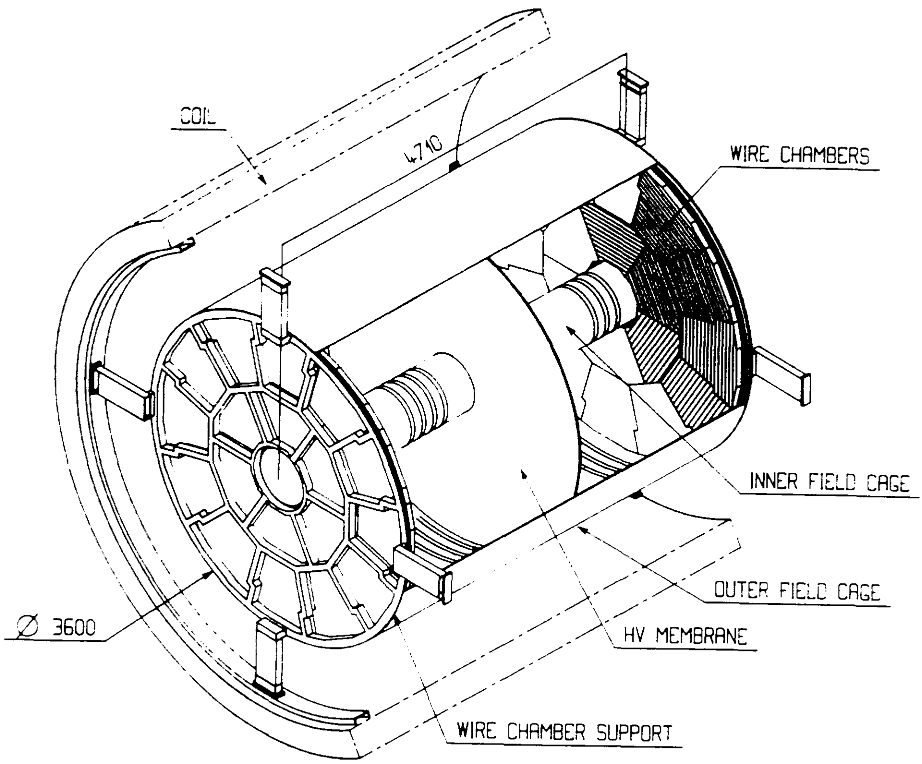

Figure 3.5: An overall view of the time projection chamber TPC.

chambers. These are detected and yield the impact point and the arrival time of the drift electrons. The pulse heights on the proportional wires are a measure of the ionization density dE/dx along the track. The azimuthal coordinates are derived from the $r - \phi$ position of the recorded avalanche,while the z coordinate is measured from their measured drift times. The ions created in the avalanche process are neutralized at a gating grid which is operated in synchronous mode, and prevents the build-up of space charge and related distortion in the drift volume.

The trajectory of a charged particle inside the TPC is a helix, and its projection onto the end-plate is an arc of a circle. Measurements of the sagitta of this arc yields the radius of curvature which is proportional to the modulus of the component of the momentum perpendicular to B. The resolution ΔP_T in transverse momentum $P_T(GeV/c)$ is proportional to the resolution in the measurement of the sagitta Δs (mm).

$$\frac{\Delta P_T}{P_T} = 0.027 P_T \frac{\Delta s}{l^2 B} \tag{3.2}$$

where B(T) is the modulus of the magnetic field and l(m), is the lever-arm over which the

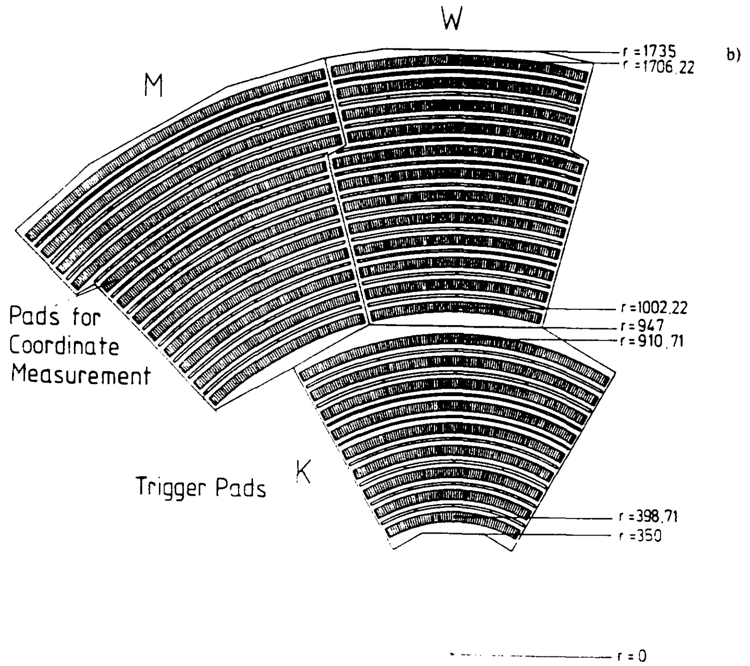

Figure 3.6: Pad arrangements in the 21 concentric circles in the TPC.

track is measured. With the lever arm of l = 1.4 m, a sagitta error of $100\mu m$ corresponds to 10% resolution in transverse momentum for the highest possible momenta, i.e. muon pairs produced at a c.m. energy of 200 GeV.

3.6.1 The performance of the TPC

The performance of the ALEPH TPC has been studied extensively on a test model (TPC 90)[43] and the chamber performance has also been studied using the data taken during the running periods in 1989 and 1990. The results obtained were compatible with the design specification[44]. In the following section the performance of the TPC is briefly discussed.

Single coordinate resolutions

The $r\phi$-spatial resolution is governed by the pad crossing angle α_x, the wire crossing angle α_W and the drift length d_i. In addition the statistics of the drifting electron cloud has to be considered. The longitudinal resolution σ_z is expected to vary with the dip angle λ of the track. An overall $r - \phi$ resolution of $\sigma = 173\mu m$ is measured with Z^0 leptonic decays as shown in Fig.3.7. The longitudinal resolution σ_z is shown in Fig.3.8. A value of $\sigma = 740\mu m$ is achieved for $|\lambda| < 10^o$.

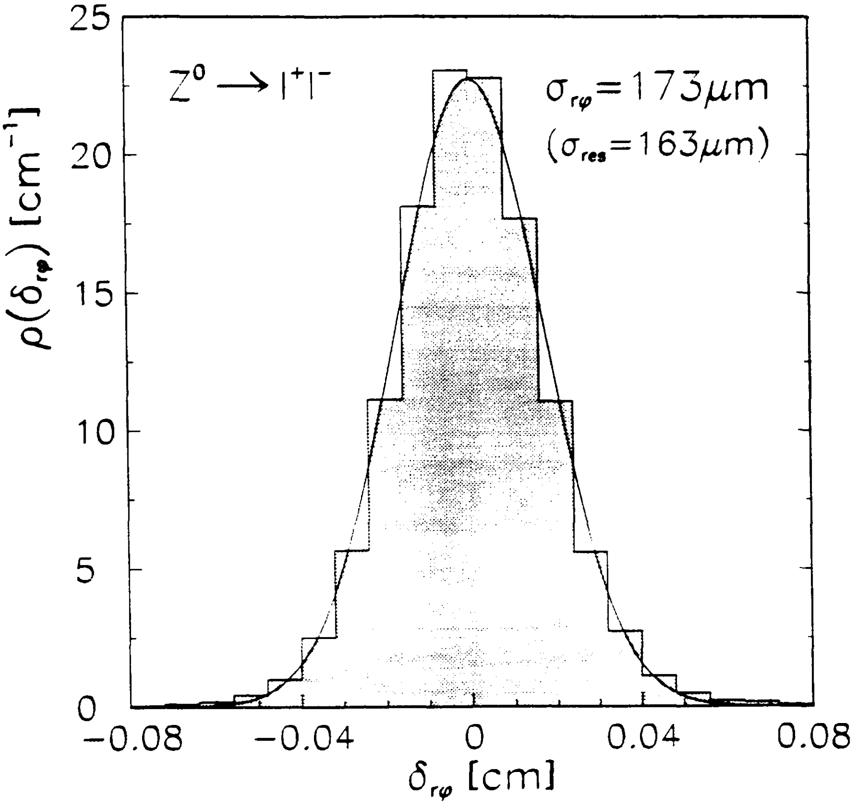

Figure 3.7: The TPC $r - \phi$ resolution measured with Z^0 leptonic decays

The Transverse Momentum Resolution

As mentioned in the previous section the momentum resolution can be calculated from equation 4.1. The limitation to the momentum resolution comes from the distortions in the sagitta measurements caused by the changes in the magnetic and electric fields, the polar angle θ, and the momentum of the track itself. To reduce the systematic errors in the resolution measurements, the TPC is provided with a laser calibration system. It is used to measure and correct residual inhomogeneities of the electric and magnetic fields, to monitor the drift velocity of electrons in the gas and to measure the important parameters used in the coordinate reconstruction. Thirty straight ionization tracks appearing to originate from the centre of the TPC are generated in the TPC. The measured curvature of these tracks is used to correct the sagitta of particle tracks; the drift velocity is measured from the reconstructed polar angles, the differences of which are known to 0.02^o. A distribution of the ratio of the beam energy over the momentum as measured in the TPC from $Z^0 \rightarrow \mu^+\mu^-$ decays is shown in Fig.3.9. A track requires 21 TPC coordinates, and the acollinearity angle between the positive and negative muons is required to be smaller than 0.3^o in order to eliminate radiative events. A momentum resolution of $\frac{\Delta P_T}{P_T^2}$ =

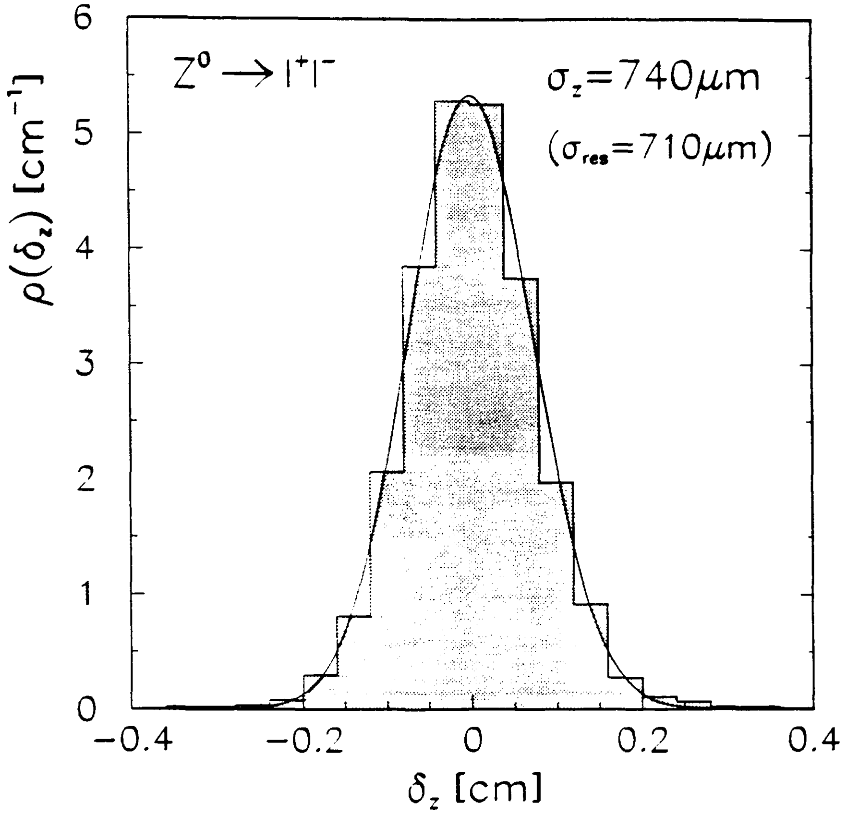

Figure 3.8: The TPC longitudinal resolution.

$0.0012(GeV/c)^{-1}$ for the TPC is achieved, in agreement with the design specification. Together with the ITC the momentum resolution is $\frac{\Delta P_T}{P_T^2} = 0.0008(GeV/c)^{-1}$, also close to the design specification of $\frac{\Delta P_T}{P_T^2} = 0.0007(GeV/c)^{-1}$. The ratio of the beam energy over momentum as measured by the ITC/TPC tracking system for dimuon events is shown separately for positive and negative muons in Fig.3.10 before and after applying the alignment corrections of the TPC sectors.

The dE/dx measurements and resolution

In addition to its main purpose as a tracking device, the TPC is used to separate particle species through their energy loss by ionization, dE/dx. This complements the electromagnetic calorimeter function for electron identification in hadronic events and provides some ability to distinguish among pions, kaons and protons. At most 320 samples of primary ionization, each of projective length 4 mm, corresponding to the wire spacing, can be achieved through the measurement of pulse height on the TPC proportional wires from all sectors traversed by a charged particle. From these measurements the value of dE/dx is determined. Only those wire pulses which match in z with a single track are used in

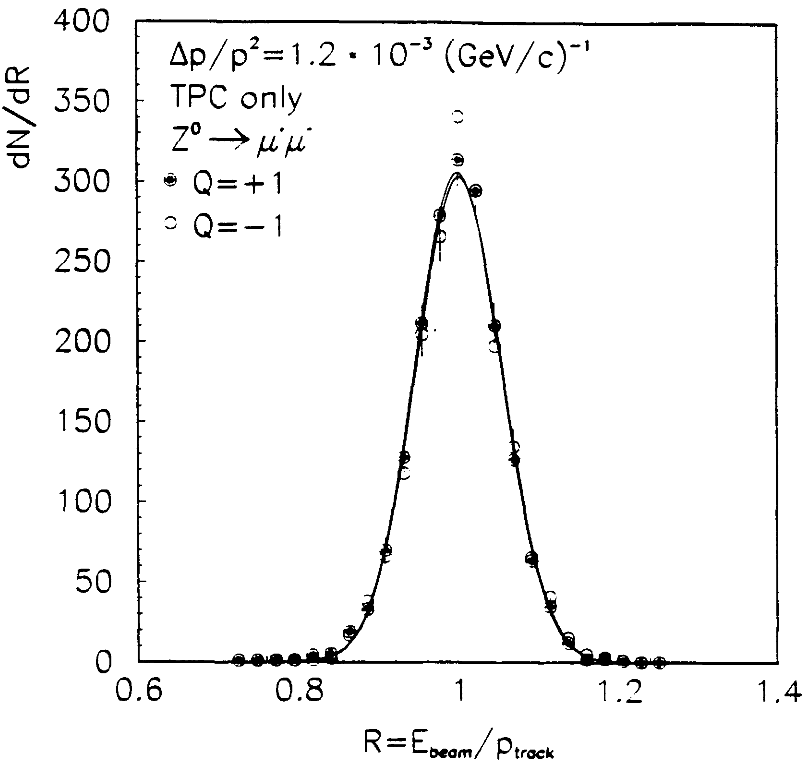

Figure 3.9: The distribution of the ratio of the beam energy over the momentum

dE/dx analysis. The dE/dx of a track is defined to be the mean of those 60% of its wire pulses, or dE/dx samples, with the lowest pulse heights, after applying corrections for the variations of sample length and for attenuation of the charge with drift. Gas pressure and temperature are closely monitored to correct for any variations in gain in the TPC sectors. The r.m.s. variations of gain within each of the 36 TPC sectors is about 3% and is found to be stable with time, with the exception of occasional shifts due to TPC hardware. Fig.3.11 shows a scatterplot of measured dE/dx versus momentum for each of (e, μ, π, K, p). A dE/dx resolution of 4.4% is achieved.

Two track resolution

The two-track resolving capability of the TPC was studied by comparing pairs of tracks from particles with the same or opposite charge as a function of the opening angle α of the pair. It was found that two equally charged "stiff" tracks are fully resolved for opening angles larger than 2.5°.

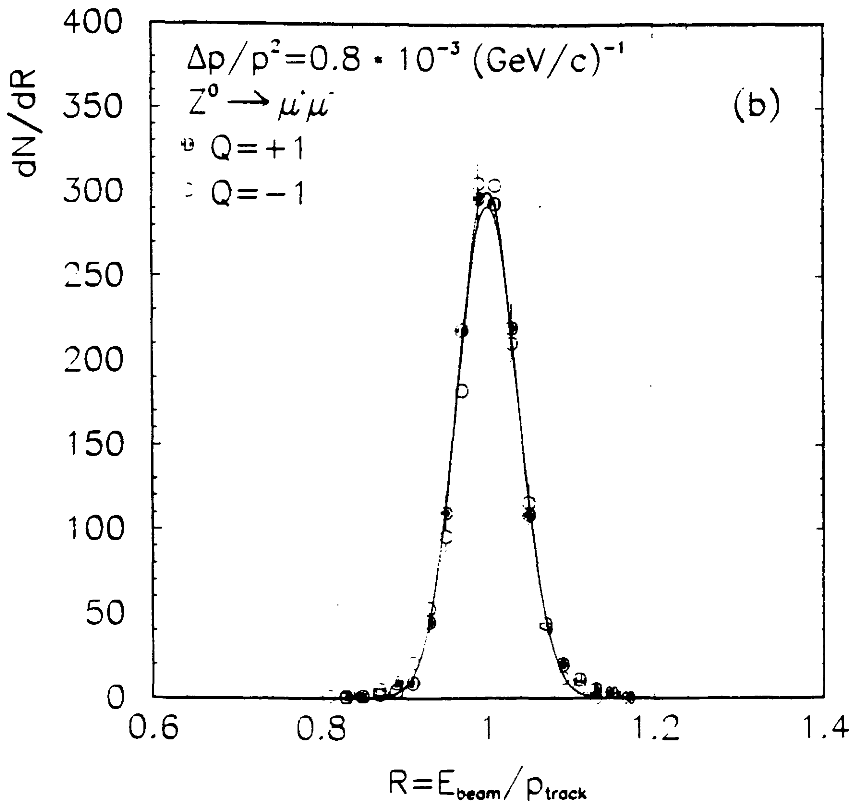

Figure 3.10: The transverse momentum resolution as measured by the ITC/TPC

3.7 The Electromagnetic Calorimeter(ECAL)

The Electromagnetic(e.m.) Calorimeter(ECAL) Fig.3.13 is a multi-layer lead/proportional chamber sandwich. The energy and position of the shower are measured using small cathode pads 30 x $30mm^2$ in dimension. The pads are internally connected to form 73,728 projective towers, each subdivided into three depth zones, or "stacks", of 4, 9, and 9 radiation lengths for the first, the central, and the last zones respectively. The large number of projective towers provides an angular coverage of 3.9π sr. This makes the calorimeter a highly hermetic detector. Dead zones (cracks) represent about 2% of the barrel and 6% of the end-cap surfaces. It provides e.m. energy measurements and e/π separation.

3.7.1 The ECAL construction

The ECAL is constructed in a way that allows a 4π solid angle coverage for events, and it is installed inside the hadron calorimeter. It is able to detect electromagnetic showers coming directly from the interaction point, with a minimum amount of intervening matter and with minimum extrapolation of electron tracks from the TPC. Under these conditions

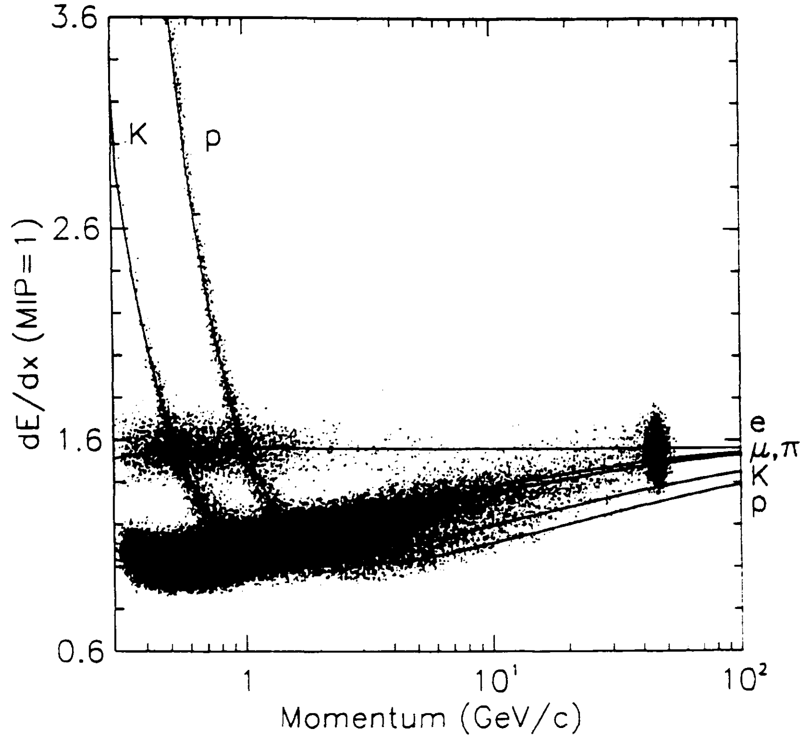

Figure 3.11: A scatter plot of measured dE/dx versus momentum for each of (e, μ, π, K, p).

ECAL achieves the highest possible spatial resolution and electron identification capability. The calorimeter is of the lead/wire-chamber sandwich type, as shown in Fig.3.14. The wire chambers are made of aluminium extrusions, with read-out by segmented cathode pads. The chambers are filled with a mixture of 80% xenon, 20% carbon dioxide and operate at approximately 60 mbar above atmospheric pressure. The high-Z gas is chosen to minimize the contribution of path-length fluctuations to the energy resolution, which are due to δ-rays propagating perpendicular to the shower direction, along the sense wires in the proportional tube. Temperature and pressure are monitored in each module.In addition each module contains a small single-wire chamber, equipped with a ^{55}Fe source. The pulse height information from the latter is used to monitor the gas gain.

The detector is built of two parts, the barrel section surrounding the TPC which is of twelve modules, each 5m long and 30^o in azimuth, closed at both ends with two end-caps each made of twelve 30^o petals, the end-cap modules having a 15^o rotation with respect to the barrel modules. The entire e.m. calorimeter is rotated by (-1.875^o) with respect to the hadron calorimeter to avoid overlapping of crack regions. Towers in the barrel continue in the end-cap, but the sector structure gives a crack pointing to the interaction point, making a 2% dead zone compared to 6% in the end-cap modules. Each

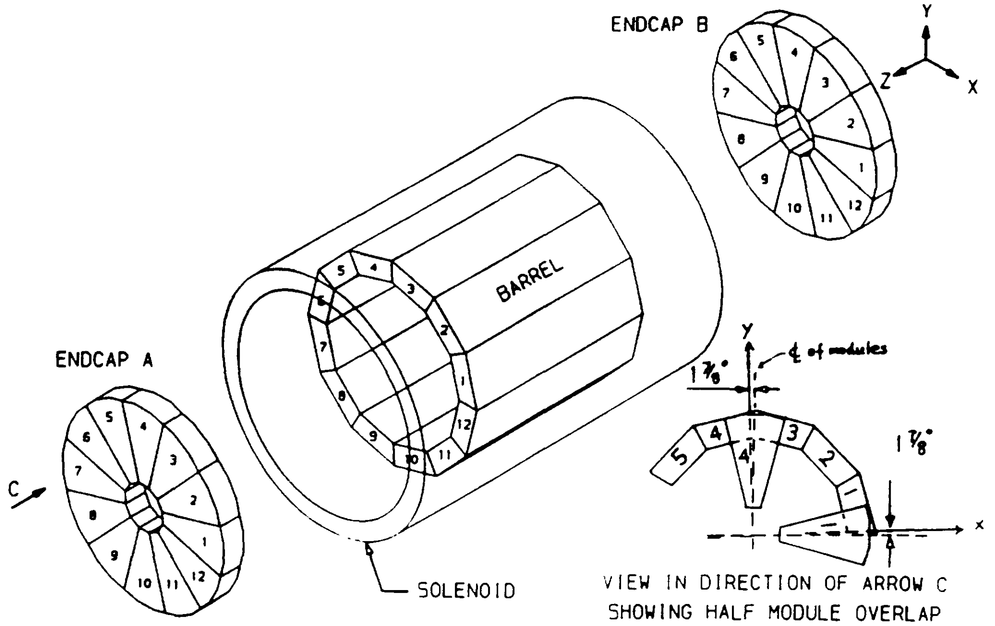

Figure 3.12: ECAL layout

module is made of 45 stack layers, the structure of which is shown in Fig.3.14. Pads from consecutive layers are connected to form towers pointing at the interaction region and allowing a high degree of shower containment. Pad signals are summed in three depth-layers corresponding to the first "stack" ($\simeq 4X_o$ of 10 layers with 2mm lead sampling), the second "stack" ($\simeq 9X_o$ of 23 layers with 2mm lead sampling), and the third "stack" ($\simeq 9X_o$ of 12 layers with 4mm lead sampling). Lead sampling layers of 4 mm thickness are used to economise on the number of layers in the last stack.

The longitudinal segmentation of the e.m. calorimeter has proved the calorimeter $e-\pi$ separation capability in the test beam and on real data. The lateral size of the tower as seen along its axis is typically 3 cm $\times$ 3 cm. In the barrel region, the segmentation in azimuthal angle $\Delta\phi$ is $\frac{360^o}{32\times12} = 0.94^o$, and in polar angle $\Delta\theta$ is $0.93^o sin\theta$. With this segmentation there are 4096 (32 $\times$ 128) towers in each module, making a total of 49125 towers in the barrel. The end-caps are similarly organized. The segmentation in the region overlapping with the barrel uses the same $\Delta\phi$ and $\Delta\theta$ division. The inner region of the end-caps has larger $\Delta\phi$ segments in order to keep the tower size roughly constant at $3\times3cm^2$. The total number of end-caps towers is 24576, i.e. 1024 towers per module. The total of 22 radiation lengths of lead is used to ensure a good containment of the showers at

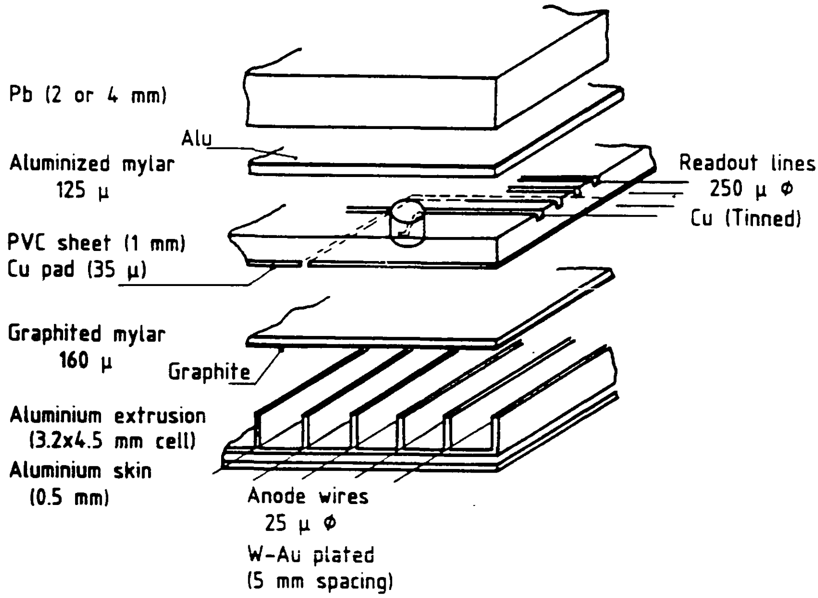

Figure 3.13: The ECAL layer structure

the highest LEP energies, while the total petal depth is less than 0.90 interaction length, i.e. a hadron will typically pass through the module with little deposition of hadron shower energy in the electromagnetic calorimeter. About 90% of the electromagnetic energy is deposited in the first two stacks, and with 70% of of the energy in a single tower when the hit is at the centre of the pad. The difference in longitudinal structure helps with electron-hadron separation and low energy photon measurement. The distribution of the energy between neighbouring towers helps to determine more precisely the centre of gravity of the shower, which provides higher spatial resolution.

3.7.2 The Electronics

The main characteristic of the ECAL electronics is the large number of analogu channels to be read (221,184 pad channels and 1620 wire channels) to obtain the excellent granularity of the detector. This can be achieved by multiplexing the signals directly at the detector modules. Since the signals from the detector are high, low-cost commercial integrating amplifiers and CMOS switches are used as the first stages of the detector for each tower. The above signals are coupled into groups of 32 and read out in turn into a summing amplifier which provides two analogue outputs, a high gain and a low gain output, where the high gain is 8 times the low gain.

The signal from the wire plane is amplified and integrated in a similar way to that of the pads with two level output gain. The signals are then multiplexed in groups of

32. For trigger purposes, the sums of even-and odd-numbered planes are formed at this stage. Signals from the wire planes can be an additional indication to that of the pads for the shower starting point in ECAL.

The signals from 32 channels are carried to one input 8-way multiplexer followed by a 12 bit ADC card working in the successive approximation mode.This ADC sequentially digitizes the analogue signals from the 256 channels connected to it. A total of 1688 ADC channels are needed for all the channels in ECAL. Readout of the channels is by zero suppressed ADC modules through Readout Controllers (ROCs). These feed the subdetector data into local event builders.

3.7.3 The Stack Layer Structure

Each of the 45 stack layers of a module is composed of two parts, the Wire Planes and the Lead Pad Board Layers.

Wire Plane

The proportional tubes formed along the plane are 3.8 mm high, 3.2 mm deep and 4.7 mm wide. Gold-plated tungsten anode wires of 25 microns in diameter run through the centre of the tubes. Wires are strung with a tension of 65g. In the end-caps every adjacent pair of the (210) wires per plane is protected by 0.125 amp fuses to avoid a wire break by excessively high current. This arrangement also allows the isolation of broken wires within the complete module. In barrel modules every wire is protected by such a fuse. The planes will withstand 2 kV on the anode wires without sparking or leakage. The anode sense wires are operated at a working voltage $\simeq$ 1400 volts in the proportional mode.

Lead Pad Board Layer

The segmented copper pads are $35\mu m$ thick with $8\mu m$ tin/lead electro-plating bonded to a printed circuit board . The pads are isolated from the wires by a graphite-coated mylar layer, and from the 2 mm or 4 mm thick lead converter by a 0.125 mm thick aluminised mylar layer. This sandwich, together with a wire plane and lead sheet forms a stack layer. The barrel modules have rectangularly shaped pads.There are 184,320 in each barrel module ($45 \times 320 \times 128$); within one tower, the first 10, the middle 23, and the last 9 layers are connected, resulting in 12,288 readout channels. Each anode wire plane has 195 to 233 sense wires which run parallel to the main component of the magnetic field. In the end-cap modules, the wire layer contain 210 sense wires and the wires run in a plane perpendicular to the magnetic field.

3.7.4 The ECAL performance

The calorimeter was tested using different techniques, the aim was to ensure the calorimeter performance and check for faults in the construction procedure such as missing pads, missing towers, broken wires. A check for faults was achieved through wire pulsing and also it provides a preliminary view for the calorimeter uniformity. Later the calorimeter was subjected to further studies to asses the uniformity and for the calorimeter abssolute energy calibration. First a relative calibration of the ECAL modules was made using cosmic rays and radioactive Krypton gas spectra. Secondly some of the ECAL modules were tested using beams of electrons and pions in a range of energy (10-70) Gev for electrons and (10-30) for pions, and later wide angle Bhabha events were used. The calorimeter shows good uniformity and an energy resolution $\frac{\Delta E}{E}$ of $\frac{0.18}{\sqrt{E}}$ and a spatial resolution of 2-4 mm[46, 45]. The construction of the calorimeter provides a tower-to-tower uniformity of (1-1.6)% (r.m.s.). ECAl energy clusters in the three stacks provide some cluster estimators (see section 4.5) which yield an electron identification efficiency of 95% while retaining pion contamination of less than $\sim$ 0.1%[46].

3.8 The Hadron Calorimeter(HCAL)

The hadron calorimeter (HCAL) is used to measure the flux of hadronic energy. It is an iron/streamer tube sampling calorimeter read out in 4608 projective towers. The iron structure of the calorimeter serves as the main support of the ALEPH detector, the passive part of the HCAL, and the return yoke of the magnet. The rolled steel plates are interleaved with gaps of 2.2 cm which accommodate the active part of the detector, consisting of planes of streamer tubes with an outer cross-section of $\phi_{tube} = 1 \times 1cm^2$, and an active cross-section of $0.9 \times 0.9cm^2$. A 100 μ m wire runs at 4 mm from the lower wall and is kept in place every half metre by plastic supports. The gas used is one part of argon, two parts of CO_2, and one part of n-pentane. Each tube layer is equipped with pad readout on one side for integrated energy flux measurements, and with strips parallel to each tube on the other side, for digital reconstruction of the pattern of individual events. Each strip is 0.4 cm wide, with a pitch of 1 cm. This digital information, which is read also on two double layers positioned outside the magnet, is the basic tool for muon identification. The structure of the active layer is shown in Fig.3.15. The streamer tubes are differently arranged in the barrel and the end- caps due to the geometrical shape of the iron. The 7m long tubes are grouped in 24 modules of 23 layers in the barrel. The first layer of each module contains 71 tubes and the last one 110 tubes. For mechanical reasons and for simplicity of gas flow, several tubes are grouped into larger boxes. The mixing of boxes with 7 tubes and with 8 tubes allows the intermediate layers to be filled completely, with an accuracy always better than 1 cm. Each module contains 2324 tubes for a total of 55776 tubes in the barrel. In the end-caps, tubes of decreasing length are arranged into sextants of the iron structure, as shown in Fig.3.16. The 2 cm spacers which

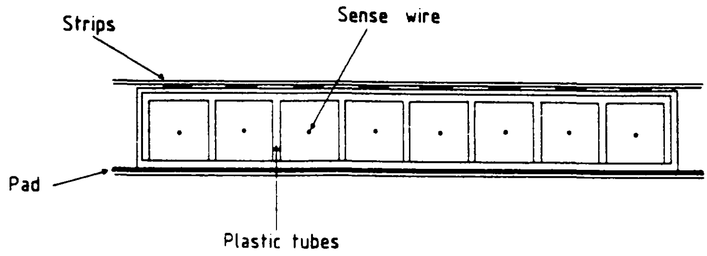

Figure 3.14: The Structure of an active layer in HCAL

couple successive iron sheets every 92 cm define the lateral dimension of the boxes. Due to the geometry of the magnet, tubes can not be installed in several regions, leading to dead regions.

The pulse height is read from pads of consecutive layers which are connected in a projective geometry pointing to the vertex. The barrel module is subdivided into 144 towers. A single tower covers the angular range $\Delta\phi = 3.75^o$ and $\Delta\theta = 2.7^o$. A total of 2688

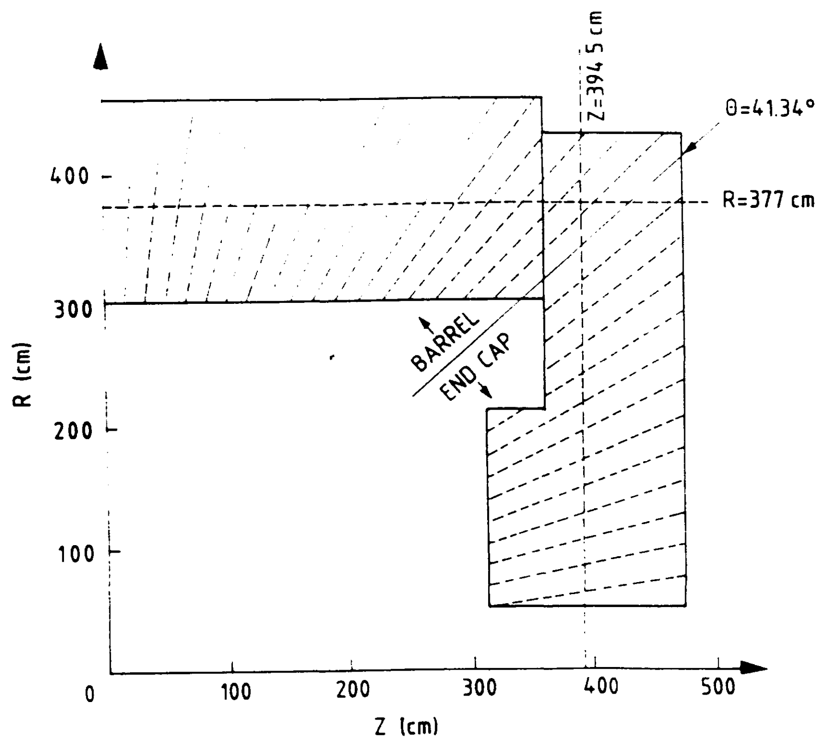

Figure 3.15: The HCAL tower geometry

towers are fully contained in the barrel itself ($\theta > 50^o$), while 384 towers on each side of the barrel module continue smoothly into similar towers, with crossed geometry, in the outer part of the end-caps ($40^o < \theta < 50^o$). These also define, therefore, the tower dimensions in the end-caps, except for the innermost four rings, where the angular granularity becomes larger to avoid towers of too small dimensions ($\Delta\phi = 7.5^o$ for $18^o < \theta < 34^o$, and $\Delta\phi = 15^o$ for $6^o < \theta < 18^o$). Pads which are interrupted by the reinforcement spacers are reconstructed at the electronic level, by summing the signals of the two parts. A total of 1320 are fully contained in the end-caps, in addition to the 768 towers shared with the barrel.

The HCAL has an energy resolution of $\frac{78\%}{\sqrt{E}}$. It is worse at energies greater than 40 GeV, where it is non linear by $\simeq 4\%$, and also at large angles where it is $\simeq \frac{82\%}{\sqrt{E}}$ (for $\theta = 60^o$). The muon/hadron separation is achieved from the pattern of fired wires produced by the strips from the digital readout.

3.9 The Muon Detector

The digital information on individual strips in the HCAL is already an essential part of the muon detector. In addition to it, external to the magnet, both the barrel and the end-caps, two double layers of streamer tubes (50 cm apart for the barrel and middle-angle chambers and 40 cm for the end-caps) are installed to identify tracks crossing the full thickness of iron and to measure their angle with an accuracy 0f 10-15 mrad. The readout strips are arranged in two projections each with an effective pitch of 5 mm as shown in Fig.3.17. In the barrel the projections are orthogonal; in the end-caps the strips cross at

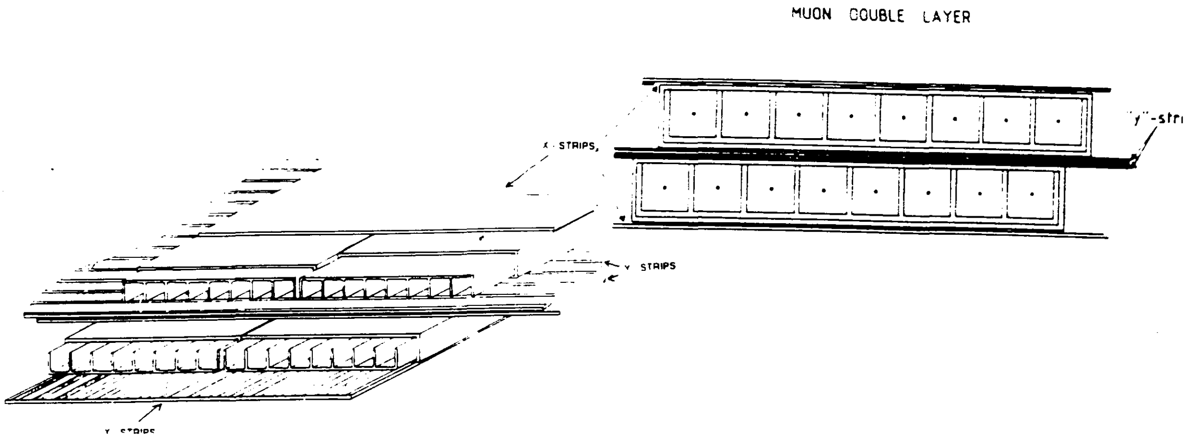

Figure 3.16: The double active layers of the muon chamber

60^o. The muon layer around the barrel is structured in 12 parts, corresponding to the decagonal shape of the magnets. Two out of the twelve modules are specially segmented to allow the passage of the magnet legs, causing 3.5% dead space in the coverage of both muon layers. In addition, the bottom module of the second layer has reduced length to avoid interference with chariots and rails. In the end-caps the muon chambers are structured in quadrants, instead of sextants as in the HCAL. In this way the number of tubes is reduced, together with the dead zones at the tube ends. Moreover, whilst the two upper quadrants are shaped as 90^o circular sectors, the lower two have rectangular shape, running down to the floor. This allows the reduction of the dead space caused in the coverage by the end-cap legs in the so called " middle-angle-muon detector" around $\theta = 45^o$. Since layers backing the barrel and the end-caps reproduce the structure of the hadron calorimeter, additional tubes are needed to cover the gaps left open in the boundary region. The total fraction of solid angle not covered by at least one double layer of muon chambers is approximately 5%.

3.10 The Luminosity Monitors

Luminosity at LEP is measured from the rate of Bhabha events at small angles. There the interference between the γ and Z^0 is negligible and the cross-section is well known from pure QED. A systematic uncertainty below 1% is achieved at LEP, so that the error in the annihilation cross-section is not dominated by the uncertainty of the luminosity. To achieve such a precision, measurement of the energy is essential to reject background both in the trigger and in the off-line analysis. In addition a precise measurement of the angles is necessary since the Bhabha cross-section is a steep function of the scattering angle.

The main luminosity monitor consists of a luminosity calorimeter (LCAL) and the luminosity tracker SATR. In fact it has now been shown, however, that LCAL alone can measure $\mathcal{L}$ to $\simeq$ 1%.

For the purpose of fast, relative luminosity measurements a Very Small Angle Luminosity Monitor (SALM) is installed. It counts Bhabhas at a rate 20 times higher than the main luminosity measurements with a minimum detection angle of 5 mrad.

A combination of the LCAL and SATR is shown in Fig.3.17 below. LCAL and SATR are briefly described individually in the following sections.

3.10.1 The Tracking Device (SATR)

The detector is arranged in four quarters, two quarters mounted on each side of the interaction point. Each quarter consists of nine planes each made up of four 45^o sectors. The planes are also subdivided into groups of three planes in depth, each with the same mechanical structure. A structure of separated tubes is used, because they behave better than MWPC's in a high background. Successive layers of planes are rotated with respect to each other to avoid dead regions. The successive planes also have three different wire orientations for ϕ position calculations. The tubes are of brass, with cross-section $9.95 \times 9.95 mm^2$ and 0.3 mm wall thickness. Anode wires are 25 μm gold plated tungsten. The wire lengths vary from place to place from 76.8 mm to 192.7 mm due to the construction geometry. To minimize dead zones between two adjacent sectors, the wires are fixed to a "pertinax comb" at the end of the tubes. In this way the dead space between the sectors due to the mechanics is reduced to 6 mm. There is, however, a wider dead space due to

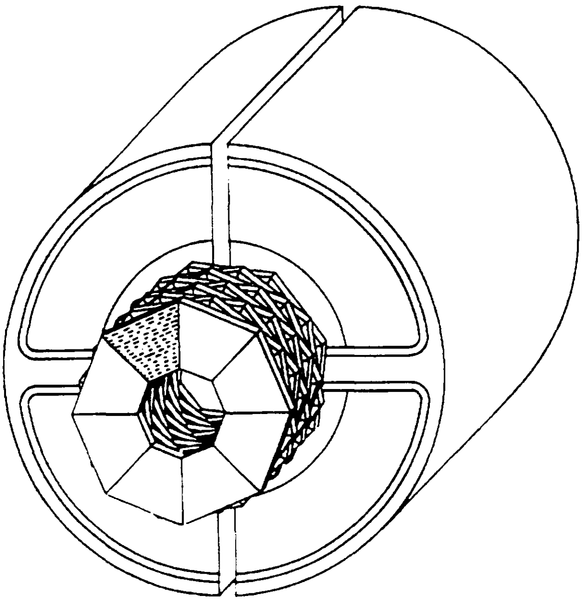

Figure 3.17: Schematic diagram of the combination of LCAL and SATR

the fact that the tubes are not cut perpendicular to the wires, giving a loss of sensitivity close to the end.

A gas mixture of Ar (90%) and CO_2 (10%), 5 mbar above atmospheric pressure, is used . To extend chamber life time by reducing the charge deposited on the wires, 1% isopropyl alcohol is added. The spatial resolution of the chamber is $\simeq 200\mu m$. The r.m.s. of the θ distribution is 0.05 mrad and that of the ϕ distribution 11.5 mrad.

3.10.2 The Luminosity Calorimeter (LCAL)

The LCAL consists of two symmetrical parts on each side of the interaction point. Each part is split into two half cylinders with outer radius 52 cm and inner radius 10 cm. The LCAL is a lead/wire chamber sampling calorimeter similar in design to that of ECAL. It consists of 38 layers of wire tubes ($4.5 \times 3.5 mm^2$), interspersed between lead converter sheets of 2.8 mm, (stack 1 and 2), and 5.6 mm thickness (stack 3). The readout is by segmented pads which are arranged in a projective tower geometry ($\simeq$ 0.2 msr) as seen from the interaction region. LCAL is segmented in depth into three sections, stack 1 (9 layers- 4.77 X_o), stack 2 (20 layers-10.6 X_o) and stack 3 (9 layers-9.24 X_o). A gas mixture of 80% Argon and 20% carbon dioxide 60 mbar above atmospheric pressure, is used . The anode wires operate with a voltage of 1450 V. Inside, the tower signals are added separately to improve the π/e rejection. Only the four innermost rings of the towers are used for luminosity measurement and triggering.

The first stage electronics used in LCAL are similar to those used in the ECAL. The total number of channels per shower counter is $\simeq$ 900, of which $\simeq$ 360 are part of the luminosity trigger and counter.

The LCAL has a resolution of $\frac{0.20}{\sqrt{E}} GeV^{-1/2}$ with a spatial resolution of $\sigma_x = \sigma_y = 2.5mm$

Chapter 4

Data Flow in ALEPH

The flow of information in the ALEPH experiment is schematically described in Fig.4.1. ALEPH has over 70K electronic channels and generates over 500 Mbytes of data per second. The trigger system reduces the rate of data to a manageable level, for DAQ processing.

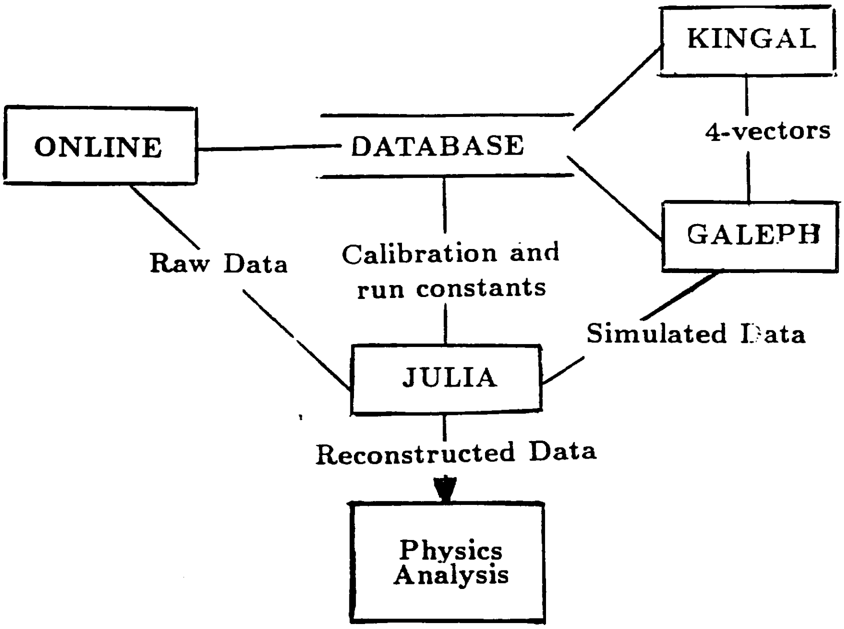

Figure 4.1: Data flow in ALEPH

4.1 The ALEPH Data Acquisition System (DAQ)

For an experiment like ALEPH which consists of hundred of thousands of subdetector elements, which deliver 500 Mbytes of raw data per second, a highly sophisticated DAQ system is required: capable of formatting and reducing the data flow to an acceptable level to be written on tape, minimize the dead time, and finally synchronizing the data from the same event.

Data reduction is achieved simultaneously by the implementation of the trigger system described in section 4.2, and by a process known as "zero suppression" i.e. only those channels which have signals above certain pre-loaded thresholds are read out. Another opportunity for data reduction comes where formatting and calibration are done.

The DAQ has a modular structure with "strong hierarchy"[48], built specifically to match that of the detector. This allows the independent readout of subdetectors, in such a way that when parallel activities take place all components match together. To achieve the best functioning of such a system in the ALEPH detector and keeping the option of component development open, a tree level architecture is adopted with a strong hierarchy. Components on the same level do not communicate with each other.

In such a structure the processing elements are masters towards the detector, and slaves in the down-stream direction towards the main computers Fig.4.2. This principle of functioning allows:

1. the skipping of a missing processing element by joining its input and output and by transferring the function to the next highest layer.
2. multiple parallel data streams to be established optimizing processing and buffering to equalize the data flow.
3. synchronization on the detector side, achieved by connecting all readout controllers to the same timing signals and at the computer level by only accepting data from the same event.
4. spy channels to allow data handling in parallel with the main data stream.

The other key feature of the architecture is " partitioning ", where the data flow from various subdetectors can be achieved, which can be triggered independently of the main DAQ. Several such data pipelines may function at a time. Components of the DAQ system are displayed in Fig.4.3. It is based on FASTBUS[49], and the tree structure transmitting cables are controlled using Fan In/Fan Out (FIO) modules. These allow the partitioning process described above. The following components process the data/control flow from the bunch crossing point to the storage device:

- **The timing unit:** Timing, Trigger and Main Trigger Supervisor synchronise the readout electronics to the accelerator, inform the ROCs via FIOs about the availability of data, keep track of the proper protocol and synchronization of all controllers and measure the dead time of the experiment.

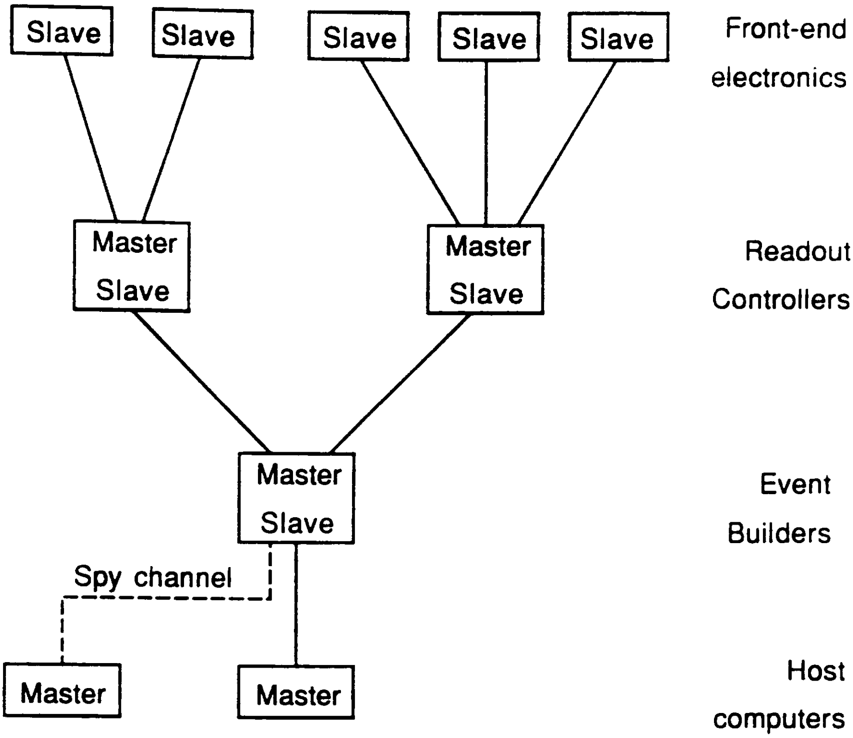

Figure 4.2: Schematic view of the ALEPH DAQ architecture

- **The readout controllers(ROCs):** After the triggering process, initialize the front-end modules, read them out, format the data into standard banks and do a first calibration.

- **The Event Builders (EBs):** Build a sub-event at the level of the subdetector, do formatting if needed, provide a "spy-event" to a sub-detector computer. This is displayed in Fig.4.3 which shows how the input/output data flow within the EBs is performed by different tasks. The producer task is responsible for reading portions of an event from the previous stage and putting these data into a buffer. The consumer task is activated when an event is written into the buffer. The consumer task releases the space occupied by an event as soon as it is transferred to the next stage of the readout. The data then are formatted and rewritten to the buffer.

- **The Main Event Builder (MEB):** Collects the pieces of an event from various

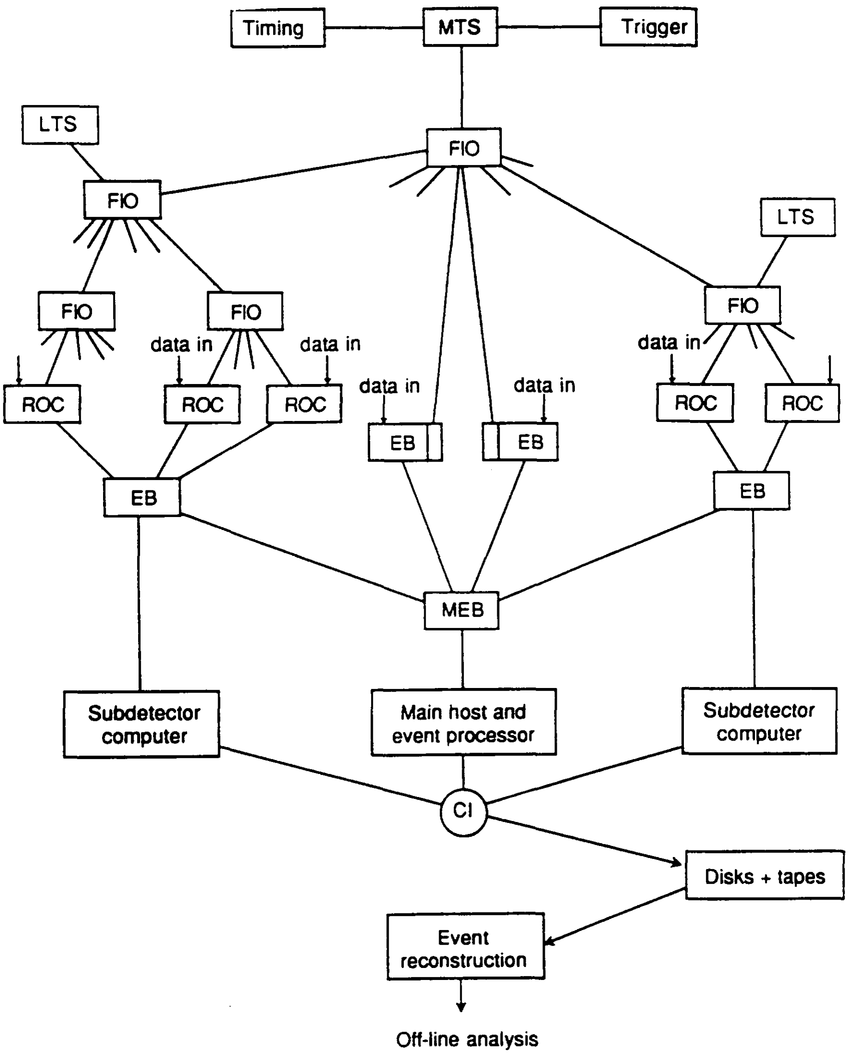

Figure 4.3: General control and data flow in the ALEPH DAQ system

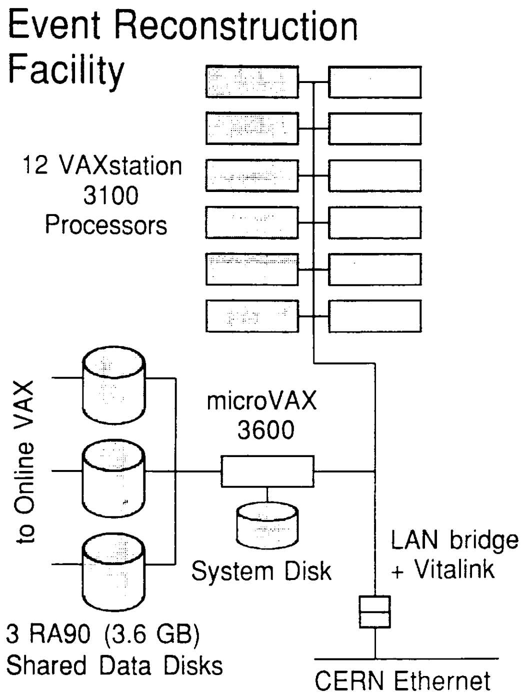

Figure 4.4: Local Area VAXCluster

EBs, ensures synchronization and completeness.

- **The Event Processor:** Also called the 3rd level trigger is a data reduction facility, limiting the volume of data written to tape.

- **Main Host and sub-detector computers:** The main machine collects all data for storage, on-line analysis, event display, etc. The sub-detector computers get the "spy-event" and perform the monitoring of the sub-detectors.

- **Event Reconstruction:** The event reconstruction described in section 4.3 is normally done "off-line", but in ALEPH "quasi-online". Events are handled by different processors using the same code as that used off-line. This is achieved by a Local Area VAXCluster with one boot node and 12 processing nodes. ALEPH uses a bank format for the structure of the events (based on the BOS memory management system[49]. The data are then stored on disk before storage on tape at the CERN computer centre and at the homelabs.

The operating conditions of the subdetectors such as voltage, temperatures, power supplies, gas control etc., are controlled and monitored using a "Slow Control" system. It is based on a microprocessor system using a G64 bus. In addition the system can detect any faults from the subdetectors and the associated electronics during the physics runs. All such information is recorded and stored in special banks, which are then added to the rest of the event information.

During the 1989 and 1990 physics runs the DAQ system handled the data with relatively small dead time $\sim 2\%$. The event volume varied from 30 Kb to several 100 Kb for large hadronic events while the detector "up-time" was $\geq 80\%$. The quality of the system was demonstrated by the number of events collected by the ALEPH detector, $\sim 2 \times 10^5$ events (higher than any other LEP experiment).

4.2 The Trigger System

The trigger system in ALEPH is part of the online system, synchronising the DAQ using the time protocol unit (TPU) and main trigger supervisor (MTS). The purpose of the trigger is to reduce the volume of data processed by the DAQ. It must be capable of retaining as far as possible any "good" e^+e^- events, while reducing the rate of background to a manageable level ($\sim 1Hz$), acceptable for gating, refresh and read out of subdetectors like the TPC and ECAL, and causing minimal dead time in the DAQ. In addition the trigger system is designed not to reject any new physics processes. This is achieved through the acceptance of any significant charged or neutral energy anywhere in the detector, unlike other experiments which search for correlations between the tracks or energy deposits. The above goals for the trigger system are achieved using a three-level trigger scheme.

- **Level1 Trigger:** This is a fast trigger, $\sim 5.5\mu s$, to achieve a total rate $\leq$ 100Hz up to the input of the TPC gating system from the beam crossing rate of 40 kHz. It serves to open the TPC gates and to initialize the level2 trigger.

- **Level2 Trigger:** This trigger checks for the presence of charged-particle trajectories in the TPC in the regions predicted by the level-1 decision. It reduces the rate to below 10 Hz. The trigger time is dictated by the full TPC drift time of $\sim 50\mu s$ so the TPC can not contribute to the level-1 trigger.

- **Level3 Trigger:** This is a slow software trigger applied after complete readout. It reduces the rate to ($\sim 1Hz$), and it verifies genuine e^+e^- interactions, separates them from background triggers, and validates them for storage.

The observed rates after each level in 1989 and 1990 data are less than those expected due to the lower luminosities delivered by LEP combined with the unexpectedly low background.

Available Trigger signals and performance

Each of the HCAL, ECAL, ITC, LCAL, and TPC subdetectors is divided into 60 segments from which the signals for physics triggers are taken, with 32 possible decisions, Fig.4.5. More details on the structure of the ALEPH trigger system can be found in[45].The

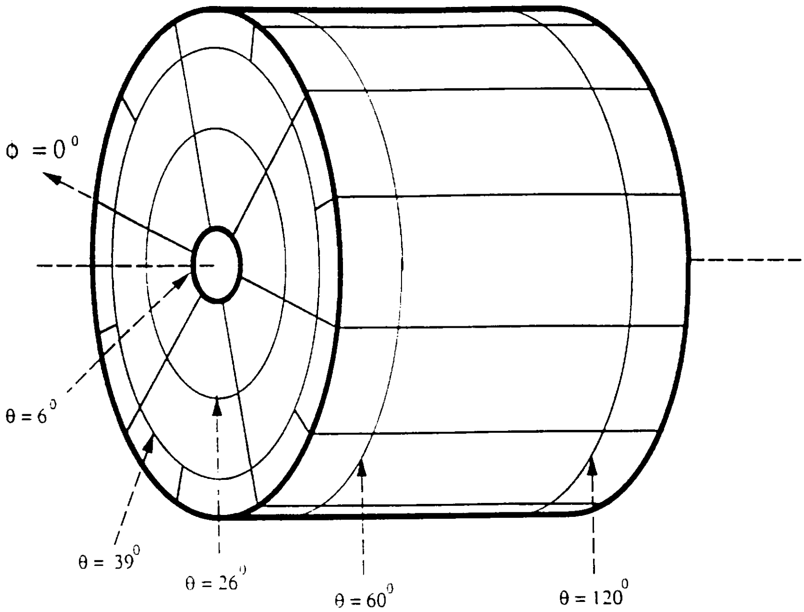

Figure 4.5: A overview of the division into trigger segments

available triggers are listed in table 4.1.

Trigger Inputs	General Trigger Description
ECAL and ITC	Total energy greater than 6.5 GeV in the ECAL barrel.
	Total energy greater than 3.8 Gev in either of the ECAL endcaps.
	Total energy greater than 1.6 GeV in both end caps in coincidence.
	Track candidate in the ITC and at least 1.3 GeV in ECAL.
HCAL and ITC	Track candidate in the ITC and four out of 12 HCAL planes fired.
LCAL	A coincidence of 20 GeV on one side with 16 GeV on the other.
	A single arm deposition of 31 GeV on either side.
	Lower energy requirement single arm trigger for background tests.

Table 4.1: General description of the available triggers.

In addition other special triggers are also available, such as triggers for electromagnetic and hadronic energy deposition. In general an event is triggered by more than one trigger.

The measured trigger efficiencies for the data accumulated throughout 1989 and 1990 is 100% for hadronic and lepton pair events and 99.7% for Bhabha events.

4.3 Event reconstruction

The official program used for event reconstruction at ALEPH is JULIA[50]. The program was written and tested well before its implementation in the physics analysis. Reconstruction is achieved in three stages.

- At subdetector level, code was written and used for the application of offline calibration and reconstruction of the data.
- The second stage is the reconstruction of basic quantities essential for data analysis such as: reconstructed track parameters, calorimeter energy clusters (LCAL, ECAL, HCAL), dE/dx information and vertex parameters.
- Finally, the reconstructed quantities are used for particle identification in physics analysis.

In this section the the algorithms relevant to the topic of this thesis are discussed with some details.

4.3.1 Track reconstruction

The track reconstruction is performed in the ITC and TPC using certain JULIA algorithms to calculate the track coordinates(r, θ, ϕ) where r is determined by the radial pad or wire position. The TPC measures the charge and the drift time of an ionization cloud produced by a charged track traversing the gas volume.

The pad "hits" include the pad address, the arrival time of the pulse, the length of the pulse in time, and the digitized pulse-heights per time-slice "bucket".

The first reconstruction step is the formation of two dimensional clusters on a given padrow by the pad numbers versus the drift time. An example is shown in Fig.4.6. A good cluster has to have ($2 \leq$ number of pads ≤ 20) and ($5 \leq$ number of buckets ≤ 35). Clusters outside these limits are rejected and are not used in track fitting.

Subsequent steps separate these pulses and clusters into subpulses and subclusters. A sub-pulse is a set of samples within a pulse which has only one significant local maxima and is sufficiently isolated from other peaks. For each sub-pulse, a charge estimate and a time estimate are calculated. Sub-clusters are sets of subpulses within a cluster from which the charge and the time estimators are used to calculate a single coordinate. In a cluster there might be more than one subcluster, hence more than one coordinate, but this does not happen at the subcluster level. When the number of pads in a subcluster is greater than three and less than six then the subcluster is divided in $r\phi$ into two or more

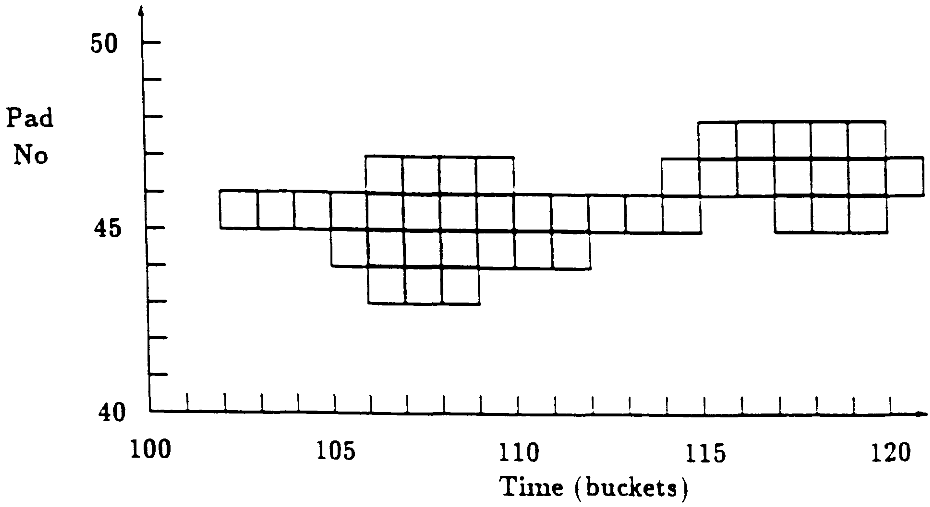

Figure 4.6: Pad clusters formed by two nearby tracks

subclusters provided that a local maximum is greater than four times the height of both significant minima.

A time estimator is defined as the time midway between threshold crossing on the leading and trailing edges of the subpulse, where the threshold is taken to be quarter of the average sample pulse height within the subpulse.

A charge estimator is defined to be the sum of all samples above the low threshold of 2 ADC counts. Other checks are made on the dead channels within the subcluster and also on the so called "half-pads" which are treated separately due to their special geometry and connections.

If subclusters pass all the requirements for a good subcluster, each is used to calculate a z and $r\phi$ coordinate.

The z coordinate is calculated by the average of individual subpulse times weighted by the charge.

The $r\phi$ coordinate depends on the number of pads in the subcluster except for long clusters.The pad response is described by a Gaussian function for the 2 and 3 pad clusters. For subclusters with more than three pads the position is determined from the charge-weighted average of pad position.

The ITC is a multiwire drift chamber which gives 3-D coordinates. The $r\phi$ coordinate is obtained from measurements of the drift time. The z coordinate is obtained from measurement of the time difference of the signals reaching the ends of the same anode wire.

Track finding in the TPC is done in three stages, by associating the coordinates to helices. This is done by adding small track segments or "chains" together. Chains are radially ordered sets of TPC pad coordinates which are consistent with the hypothesis of lying on the same helix. In the first stage chains are found. These are combined to form the "track candidate", defined as a set of chains which is consistent with being caused by the same particle. The third step is the fitting of all first half arcs of the track candidate. As a result a TPC track is formed.

The fitted helix parameters and their definitions are listed below:

1. $R =$ Inverse radius of curvature in (X, Y).
2. $D0 =$ Closest point of approach to the beam in (X, Y).
3. $Z0 =$ Z position at the point of closest approach on the Z-axis.
4. $\phi_o =$ initial angle of the track in the (X, Y) plane.
5. tan $\lambda = dZ/dS_{xy} =$ tangent of the dip angle. (S_{xy} is the length of the projected track in the x-y plane from the point where $x^2 + y^2 = D_0^2$)

A track appears as a circle in the (X, Y) or (r, ϕ) planes, while in the (S_{xy}, Z) projection it is a straight line as shown in Fig.4.7. The TPC tracks are associated to the ITC

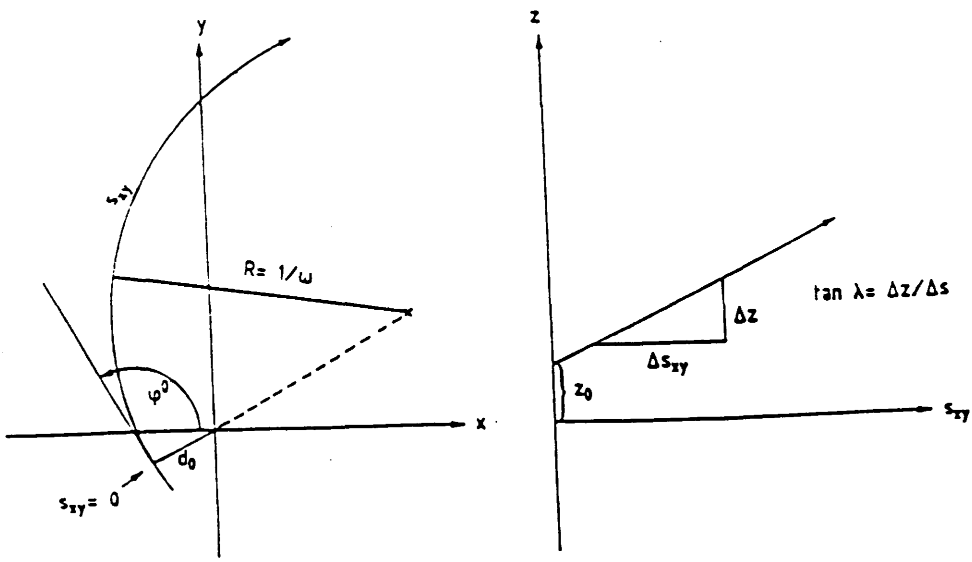

Figure 4.7: Helix parameters and notation for fitting TPC tracks

hits by searching the outer 2 layers of the ITC for a specific trajectory. If no suitable ITC hits are found the search is abandoned. If more than 3 hits out of 8 are found then a fit is performed and the ITC track is accepted if it satisfies a χ^2 cut.

The other important piece of track information which is relevant to this work is the ionisation loss $\frac{dE}{dx}$. This information is provided by the wire hits of the TPC associated with the corresponding track. A truncated mean of associated pulses is then calculated after normalizing to the projected track length seen by the wire.

4.3.2 Calorimeter Reconstruction

During the construction of the calorimeters, they were tested to study noise effects and also to search for dead pads, dead storeys and dead wires as a preparation for data taking. From such studies off-line corrections have to be made to the tower energy measurements which include noise subtraction on a tower by tower basis.

The offline corrections are applied to the calorimeter reconstruction procedures namely finding the topological clusters, assigning the tracks to clusters and finally establishing the relationship between ECAL and HCAL objects.

Cluster Finding

The algorithms used to form ECAL and HCAL clusters require two connected storeys to have at least one corner in common, giving ECAL-clusters and HCAL-clusters, treated separately at this stage. For the clustering algorithms two different thresholds t_{high} and t_{low}, set to 90 MeV and 30 MeV respectively, are applied to the energy deposited in a storey. A cluster must have at least one storey with an energy above t_{high}. An alternative strategy is to fix the value of both thresholds at 30 MeV and apply an additional cut of 90 MeV on the total energy of the cluster.

Object Formation

A stepwise helix extrapolation of each good TPC track towards the ECAL is performed. The ECAL geometry package is used to determine which storey is intersected by the track. The extrapolation road size is 3 cm, the size of an ECAL storey, so one point of the track must lie on the cluster storey or share a corner with one of its storeys. This means that more than one cluster can be associated with a track. The correspondence between ECAL clusters and ECAL objects is not necessarily direct. The main difference is that only one ECAL object is related to a track.

The formation of HCAL objects is performed in a similar way. If a track traverses ECAL and has an energy consistent with that of a minimum ionizing particle, then the track is extrapolated to the end of the ALEPH detector including HCAL and the muon chambers, taking into account the magnetic field and the energy loss. In the HCAL as in the ECAL, the storey energies above a certain threshold are summed for a given distance from the extrapolated track. Clusters are formed from these storeys and are associated to the track.

In the muon chambers a search for hits in the chamber layers is performed for the purpose of muon identification. Association of ECAL and HCAL objects is performed on the basis of cluster energy and the transverse momentum of the HCAL object with respect to the track.

Finally it is worth mentioning that throughout the reconstruction process the measured values of the parameters used in the reconstruction are kept in BOS banks for ease of access during physics analysis.

4.3.3 Event Simulation program GALEPH

GALEPH is the ALEPH simulation program. The generator used for the τ events is KORALZ which depends on two libraries, the τ decay library and the library of electroweak corrections. The KINGAL event generator described in section 4.4, uses the kinematics of the primary particle momenta and type then produces the decay particle kinematics. The output from the event generator is fed into the GALEPH program which performs the detector simulation.

GALEPH is interfaced with the ALEPH geometry package library where all the details of the geometry and materials used in all ALEPH subdetectors are stored, the GEANT and GHEISHA packages, and the TPCSIM package which is used specially for TPC simulation. TPCSIM is called after the tracking and digitization mentioned below are completed. GALEPH provides GEANT3 with all the information about the detector geometry and the materials of the detector , and all the coefficients related to the material used in the detector. In addition it also provides the output data from the KINGAL generator. The primary particle is followed (tracked) through the detector together with the secondaries produced in the detector. The particles generated in the detector depend on the primary particle and the material with which it interacts. Processes such as ionization, bremsstrahlung, and Compton scattering are simulated. Electromagnetic and nuclear interactions are simulated using the GEANT and GHEISHA packages respectively. The simulation is done in steps, starting from the interaction point, through the exchange of information between GALEPH and the interfaced packages. Then the response from the sensitive parts of the detector, HITS, is passed back to GALEPH for digitization and stored in BOS banks. The simulated data are saved in the same way as real data and so can be reconstructed using the official ALEPH reconstruction program JULIA.

GALEPH has also some internal facilities for event generation, which can be chosen from data cards, i.e. the generator can be run inside GALEPH as a "user kinematics" triggered by data cards. This is accomplished by interfacing the KINGAL package.

4.4 Monte Carlo Simulation of Events

In the ALEPH collaboration Monte Carlo data are produced using more than 50 generators. This work is made possible because of the existence of the interface package, called KINGAL, between the physics generators and the rest of the ALEPH software. The KINGAL program is used in "stand-alone mode" or directly inside GALEPH, the detector simulation program through the dummy GALEPH routines ASKUSI, ASKUS, and USCJOB. (More details are available in the KINGAL and GALEPH user guides)[51].

4.4.1 The MC program KORALZ

The KORALZ program was originally written to simulate tau pair production, although its new versions are capable of producing other fermion pairs at LEP/SLC energies[52]. Monte Carlo simulation of τ pair production is necessary for many purposes:

- Comparison of data with the standard electroweak model,
- Calculations of QED bremsstrahlung effects,
- Removing detector inefficiencies,
- Studies of background and systematic effects.

An important property of the process $e^+e^- \rightarrow \tau^+\tau^-$ is the possibility of measuring the longitudinal polarization of the tau lepton as described in section 2.3. This can be done by looking at the energy distribution of tau decay products. The weak interaction of the tau lepton makes it a powerful tool for the establishment of the electroweak model, since it is a parity violating interaction which produces the polarization, while the data analysis is more difficult because of the complexity surrounding the determination of its decay channel. The program includes the production and subsequent decays of the lepton pair in e^+e^- interactions. The latest version of the program incorporates the following characteristics:

1. Multiple QED bremsstrahlung from the initial $e^\pm$ and single photon bremsstrahlung from the final state, but not the interference between the initial and final states in the case of hard bremsstrahlung in the initial state.
2. $O(\alpha)$ radiative corrections from the Standard Model. $O(\alpha)$ corrections to the tau decay are also included in leading logarithmic approximation, except for the multi pion decay modes.
3. Only longitudinal spin polarization for the incoming $e^\pm$ and outgoing $\tau^\pm$ are included.
4. The most frequent decay modes of the tau lepton, $\tau^\pm \rightarrow \bar{\nu}\nu e^\pm$, $\bar{\nu}\nu\mu^\pm$, $\nu\pi^\pm$, $\nu\rho^\pm$, $\nu K^\pm$, $\nu K^{*\pm}$, $\nu 5\pi^{\pm,o}$, $\nu 6\pi^{\pm,o}$ are included.
5. Single bremsstrahlung in the most important tau decay modes: $\bar{\nu}\nu e^\pm$, $\bar{\nu}\nu\mu^\pm$, $\nu\pi^\pm$, $\nu\rho^\pm$, $\nu K^\pm$, $\nu K^{*\pm}$ (in the leading logarithmic approximation). This is of great importance due to the fact that polarization is extracted from energy measurements of the tau decay products.

The program is "flexible" in the sense that it allows the production of events with different properties, forcing a certain decay mode, spin state, with or without radiative corrections. This is done by changing parameters in the CARD FILE of the generator such as

- Energy of incoming $e^{\pm}$ and their spin state,
- $sin^2\theta_W$ either calculated by KORALZ in terms of other parameters or inserted by hand in the card file,
- Z^0 and W masses. Since the W mass is not well measured, it is determined inside KORALZ in terms of the Fermi constant and other parameters.
- Width of the Z^0, with crude $O(\alpha)$ radiative corrections.

Other parameters such as M_H and m_t, the Higgs and the top quark masses, are fixed to values of 100 GeV. In addition in this program the number of neutrino families can be changed and the neutrinos can be given mass.

4.5 The Physics Analysis Program ALPHA

The Physics Analysis package (ALPHA) is used to analyse the data collected by the ALEPH detector. The package is a set of routines aimed to simplify the programs for physics analysis. It is written to analyse the output (POT, DST, or MDST) of the ALEPH reconstruction program JULIA, although all ALEPH data types can be analysed. All the input/output is done by ALPHA by providing the input/output data cards. Also it provides access to physical variables such as energy and momentum and ALPHA routines can be used to extract the other variables (e.g. kinematics, event shape, etc.) This allows the user to analyse the data without detailed knowledge of ALEPH data structure (tabular BOS banks). Three Fortran routines have to be supplied to run the program, job initialization, event processing, and job termination. Reconstructed objects (track vertices,calorimeter objects) in the events can be accessed by simple DO loops. Simulated data are accessible in the same way.

4.5.1 Particle identification with the ALEPH detector

One of the most important properties of the detector for τ decay modes is the ability to identify e, μ, hadrons and photons. Electrons are identified by the shower pattern in the ECAL, and the total energy match with the momentum measured in the TPC. Muons are identified by hits in the muon chambers accompanied by a minimum ionising shower pattern. All other particles are regarded as hadrons. The discrimination between pions and kaons is done in the TPC. The efficiency depends on the particle momentum. Photons are detected as electromagnetic showers in the ECAL without any associated track in the TPC. A more complete description can be found in[53]. The following sections give details of the algorithms used for particle identification of the most interesting particles in this work.

4.5.2 Electron Identification

Electron identification in the ALEPH detector is based on the combined information from the charged track detectors ITC and TPC and the electromagnetic calorimeter ECAL,with charged track momentum, track extrapolation and energy loss (dE/dx) from the TPC and position and energy of the fired storeys of the ECAL clusters associated with the charged track.

Two independent measurements are used for electron identification. The energy deposition in the ECAL is most effective at high momentum, (above 5GeV), while the dE/dx measurements are most useful at low momentum.

The high granularity of the electromagnetic calorimeter provides the precise position and amount of energy deposition in the neighbourhood of the extrapolated track. The longitudinal segmentation of the read out allows a good e/π separation. Using the shape and energy of the electromagnetic shower in the three storeys, the total energy deposited in the ECAL and the energy loss in the TPC, a set of variables (estimators) is defined which allows comparisons with those expected for an electron, as follows:

Momentum-energy balance(R_1)

R_1 measures the difference between the track momentum P and the charged cluster energy E normalized to $\sigma(E,P)$, of their resolution $\sigma(P)$ and $\sigma(E)$.

$$R_1 = \frac{E-P}{\sigma(E,P)} \tag{4.1}$$

Transverse estimator(R_2)

R_2 compares the measured momentum to the energy deposited in the four towers closest to the extrapolated track. From the test beam data it was found that around 83% of the electron energy is deposited in the 4 central towers, with no dependence on angle and energy of the electron for $P > 2GeV/c$. In ALEPH the tracks are bent by the magnetic field and a variable (X) is defined as:

$$X = \frac{E_0}{P} \quad \text{with} \quad \mathrm{E}_0 = \sum_{\mathrm{i}=1}^{3} \mathrm{E}_\mathrm{i} \tag{4.2}$$

where E_i is the energy deposited in the closest storeys to the charged track extrapolation in stack number (i), Fig.4.8.

The variable has a Gaussian distribution for an electron of given energy (c.f. Fig.4.9). The mean, $< X >= 0.83$ is independent of angle and momentum for $P > 2GeV/c$, while the parameterization of the variance $\sigma^2(X)$, with respect to momentum is obtained from test-beam measurements. Thus for electrons, the variable

$$R_2 = \frac{X - < X >}{\sigma(X)} \tag{4.3}$$

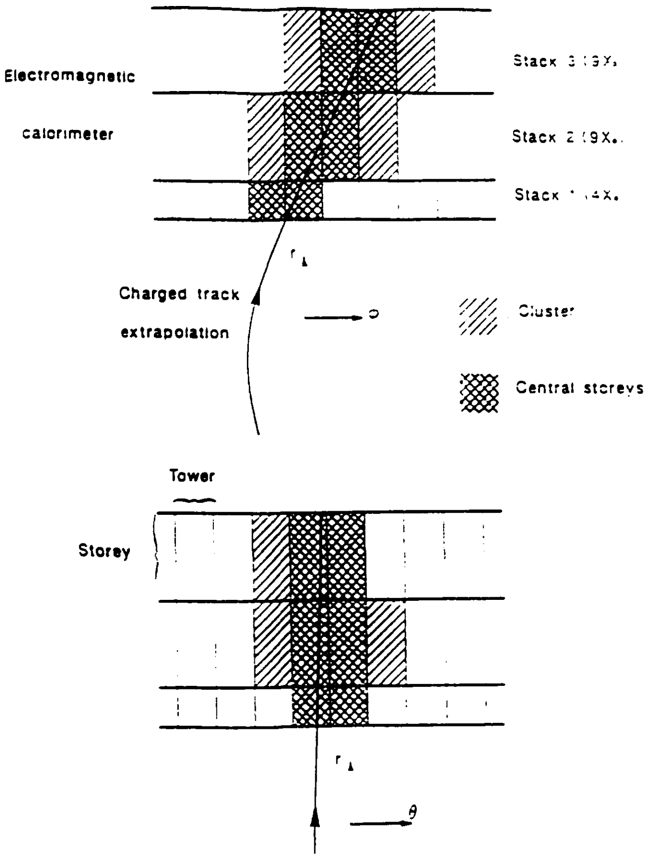

Figure 4.8: Definition of central storeys

is normally distributed with zero mean and unit variance. Due to the high granularity of the ECAL, this variable reflects the compactness of an electromagnetic shower as well as giving a measurement of the momentum-energy balance R_1.

Longitudinal estimator(R_3)

R_3 provides a measure of the degree to which the longitudinal shower profile matches that expected for an electron. It is related to the inverse of the mean position (A) of the longitudinal energy deposition:

$$A = \frac{E_0}{\sum_{i=3}^{3} E_i S_i} \tag{4.4}$$

where S_i is the mean longitudinal position of the shower in stack i. Results from the test data show that for electrons of given energy, A has a Gaussian distribution. The estimator R3 is then defined in terms of the parameterization of $< A >$ and $\sigma(A)$ from the test-beam measurements:

$$R_3 = \frac{A - < A >}{\sigma(A)} \tag{4.5}$$

which, for electrons, is normally distributed with zero mean and unit variance.

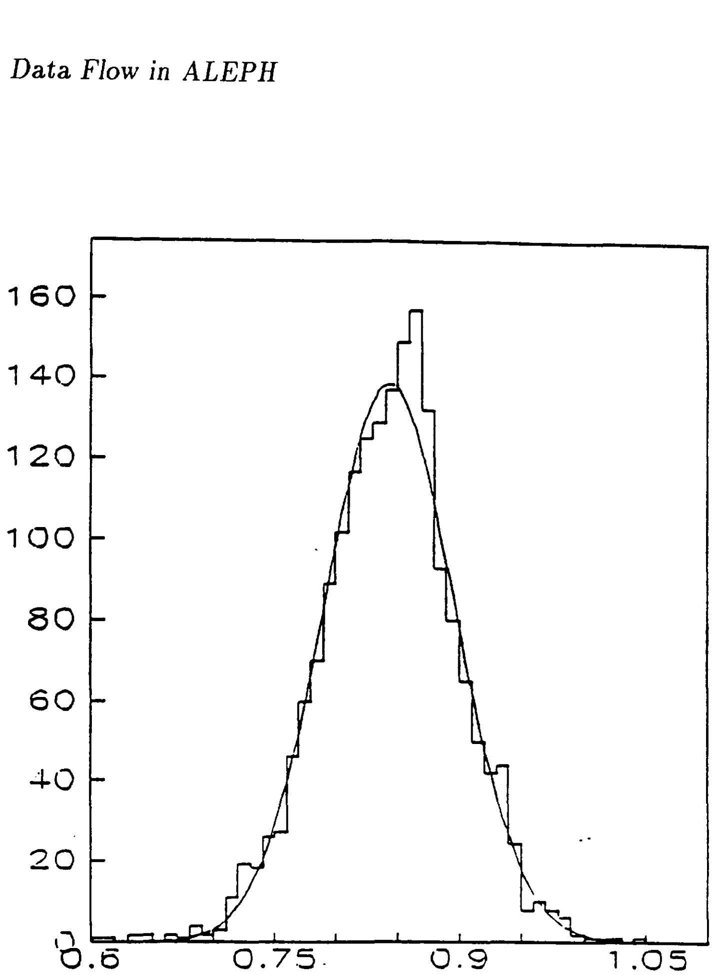

Figure 4.9: The X spectrum for 10 GeV no radiative electrons

Energy loss estimator(R_4)

The dE/dx information from the TPC is used as a supplementary tool for electron identification using ECAL. The measured dE/dx, I_m, is defined to be the 60% truncated mean of the individual wire measurements. Only tracks associated with at least 80 isolated wire hits are considered in the dE/dx analysis.

The dependence of the mean value of I_m on particle velocity is measured from data. The momentum region of interest in the measurement is on the relativistic rise for pions and kaons, while electrons are always distributed about the plateau position $< I_e >$, lying a factor of 1.58 above the minimum. By taking the difference of the measured dE/dx and that expected for an electron, an estimator is defined which is normally distributed for electrons:

$$R_4 = \frac{I_m - < I_e >}{\sigma(I)} \tag{4.6}$$

Z^0 hadronic decay data are used to obtain a parameterization of $\sigma(I)/I$, which depends only on the number of wire samples.

The dE/dx measurement significantly reduces the background of hadron misidentification by requiring the electron candidate to satisfy $R_4 > -2.5$ as well as the ECAL cuts. The main source of misidentification using dE/dx is the requirement of at least 80 isolated wire hits.

4.5.3 Muon Identification

Muon identification is based on high penetration capability and minimum ionizing particle compatible showering measured by the calorimeters. Thus almost all ALEPH subdetectors supply information for this purpose, namely hits in the x and y strips of the muon chambers, hits from the digital read-out of the streamer tubes of the hadron calorimeter, shower characteristics in ECAL plus the hits and dE/dx in the TPC.

To be considered a muon candidate, the track must satisfy the following criteria. First, the track is extrapolated through the subdetectors up to the muon chambers. The extrapolation up to the coil is done through the uniform magnetic field. The iron yoke is subdivided into parts and the magnetic field considered homogeneous inside each part. There must be at least one muon chamber hit within a distance from the extrapolated trajectory compatible with multiple scattering. If hits from two layers of chambers are associated with the track then the observed exit angle from the iron should match the angle from the extrapolation within multiple scattering.

Second, the digital pattern of the hadron calorimeter tubes must be compatible with that of a non-interacting and penetrating particle.

Hence, for muon identification the "muon digitizings" of muon chambers, the reconstructed data for the HCAL tubes and a reconstructed track in the TPC are needed. To determine whether the track is consistent with being a muon in the HCAL, a search is made in a 20 cm wide road around the extrapolated track position in HCAL for hits in the digital readout. A track is considered as muon if

$$\left(\frac{N_{fired}}{N_{expected}}\right)_{allplanes} > 0.5 \tag{4.7}$$

and

$$\left(\frac{N_{fired}}{N_{expected}}\right)_{last10planes} > 0.3 \tag{4.8}$$

For 1989 data the muon chamber information was not available and only HCAL information was used. The last three planes then have to be fired for a muon candidate. For the 1990 data, hits in the last two planes are required in addition to the wire chambers. When two tracks share the same pattern of HCAL hits the one with MUON chamber hits is selected. If both have muon chamber hits the closer one is selected and, if there are no hits for both, the closest to the HCAL pattern is chosen. $20 \pm 2\%$ of candidates are found to be shadowed, with good agreement between MC and real data. To eliminate cosmic ray muons and decay in flight of π and K a cut of $|D_0| < 1cm$ is applied.

4.5.4 Photon Identification

Photons are detected from the neutral clusters of the electromagnetic calorimeter not associated with any charged track. They are also included in charged hadronic clusters or produced by an electron undergoing bremsstrahlung. About 70% of such clusters are isolated inside a module and the rest are near a crack or in the overlap area between the barrel and the end-caps. The two groups are separated using the position of the tower with maximum signal. This provides an approximation of the line of flight and also allows the calculation of the widths of the crossed stacks in radiation lengths. The neutral clusters are studied through the energy deposited in each of the three stacks and the materialization depth in the direction of the line of flight.

The following methods were adopted for the study of neutral clusters and their recognition

- **Longitudinal configuration probabilities:** The contents of the three stacks 1, 2, and 3 are compared to thresholds of 50, 70 and 100 MeV, respectively. Using this information with the total signal and the stack widths, a probability is deduced from a tabulated parameterization that the neutral cluster is due to a photon.

- **Longitudinal analysis:** The starting point of the cluster obtained from the contents of the stacks provides a method for a probability calculation. A shape identifier can be defined also when the contents of the three stacks are above the threshold.

- **Transverse analysis:** The separation between single and multi-gamma clusters is achieved from the transverse distribution from the existence of more than one storey with energy above a certain threshold within the cluster.

A cluster is called pure gamma if all identifiers yield a probability that it is due to a gamma > 0.1[54]. When applying the above algorithms for gamma identification in the overlap region the gamma energy is corrected according to the test run data and simulation. If the cluster is in a crack region the transverse analysis is essential. The impact point estimation leads to a correction of the measured energy.

4.5.5 Hadron Identification

The track is defined as a hadron if it fails the previous searches among the charged tracks for muons and electrons. Hence a candidate to be recognized as a hadron should not have:

- a shower in ECAL with energy deposition greater than 0.6 of that measured in the TPC, or

- dE/dx measurements compatible with those of an electron

The HCAL energy deposited and digital readout pattern are used for hadron/muon separation. Hadrons like pions, kaons and protons are separated using the dE/dx information from the TPC.

Chapter 5

Event Selection

5.1 Introduction

High energy beam collisions such as those of LEP can produce a complex of signatures according to the beam conditions and the outcome of the interaction between the colliding beams. Background signals can be detected as a result of, for example, beam-gas interactions, off-axis particles, Bhabha events, and two photon events. Some of these signals such as noise and signals generated from outside the detector are rejected by the data acquisition system described in chapter 4 while others remain and are eliminated in a sequence of cuts applied on the data according to the characteristics of different types of events. For example Bhabha events are rejected according to their small angle with the beam axis while the kinematics of the two photon events are used for their rejection. The interesting signals resulting from e^+e^- collisions in the LEP energy range occur mainly through Z^0 exchange. Subsequently these Z^0 particles decay into a pair of fermions which again leave different signatures in the detector. Of interest in this analysis is the decay $Z^0 \rightarrow \tau^+\tau^-$ followed by the decay of the tau lepton to a pion and a tau neutrino. In the first section of this chapter the procedure for the selection of the tau events from the Z^0 sample accumulated by the ALEPH detector is described. In the next section the selection of the decay $\tau \rightarrow \pi\nu$ from the tau sample is described.

5.2 Tau event selection

The reaction $e^+e^- \rightarrow \tau^+\tau^-$ has very distinct characteristics of special topology and kinematics of the τ pair final state. At LEP energies, and due to the small tau mass compared to the high centre of mass energy, decay products are contained in a narrow cone, and the multiplicity is low: more than 99% of tau decays result in one or three charged tracks,see Table (2.2). The tau candidate can not be detected directly as a result of its very short life time so it has to be detected through its decay products. The signature of the events in the ALEPH detector is a small number of charged tracks plus high energy deposition in the calorimeters. The tracking in ALEPH is done in the time projection chamber (TPC) and the inner tracking chamber (ITC). Momentum is measured in the TPC, while the energy can be measured by the calorimeters. Examples of typical events in the ALEPH detector are shown in Fig.(5.1). The selection philosophy is to achieve

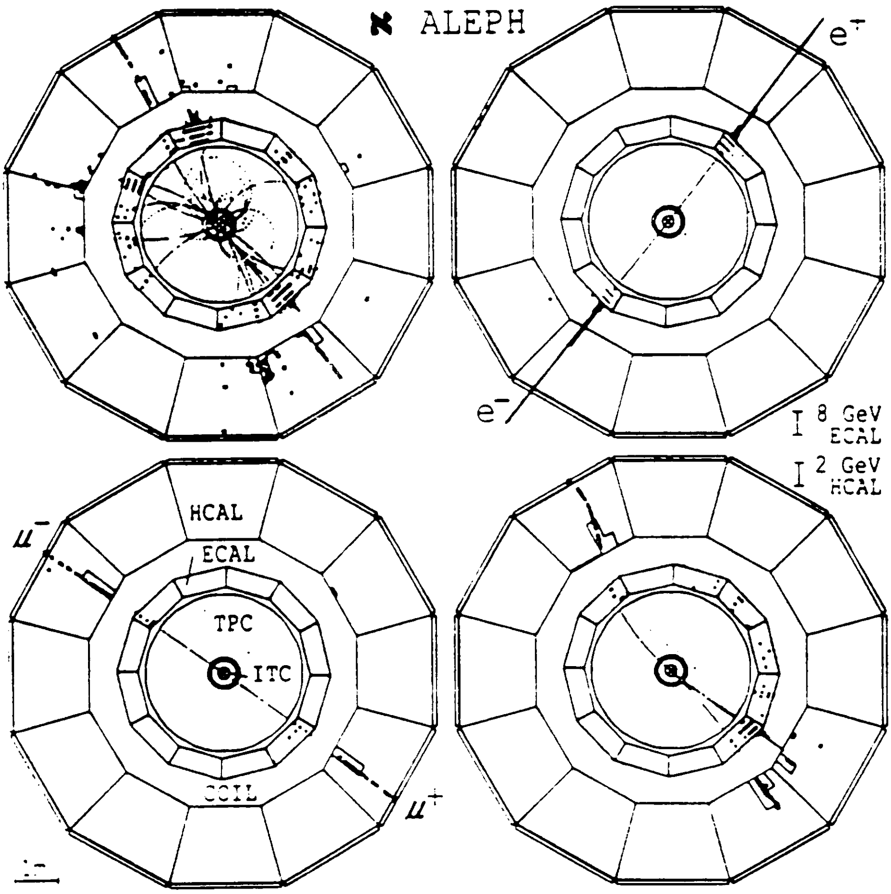

Figure 5.1: Typical events in ALEPH detector

high detection efficiency while being able to detect all tau decay modes, on which the understanding of tau decays is built. This depends on the detector particle identification capability which was discussed in section (4.5.1).

Other processes which can simulate a τ signature in the ALEPH detector are $e^+e^- \rightarrow q\bar{q}$, $e^+e^-f\bar{f}$, $e^+e^-(\gamma)$, $\mu^+\mu^-(\gamma)$ and $q\bar{q}(\gamma)$. Such backgrounds must be well known and carefully studied. There are uncertainties both in the theoretical cross-sections and in their MC simulation. To eliminate background events, cuts on multiplicity and energy content of the events are applied to select the tau sample. MC studies have been used to estimate the selection efficiency of the tau events and of the background processes. Luminosity calculations were done on a run by run basis in the standard manner used by the collaboration[57]. Trigger efficiencies for the selected tau sample have also been calculated[58]. In this analysis of 1989 and 1990 data in the vicinity of the Z^0 peak, those runs for which there were known, serious problems with some part of the detector were first discarded. The subsequent selection criteria fall into three steps: track selection , tau preselection and finally the selection of the tau pair sample. These steps are described in the following sections.

5.2.1 Track Selection Cuts

In any detector some deficiencies are to be expected in the performance of the tracking system, for example due to partially lost tracks, tracks splitting into two tracks which will lead to bad track momentum measurements and double track counting. As described in section (4.3.1) a number of measurable track parameters are determined from the ITC and TPC tracking detectors, including the polar angle θ of the track, the number of hits in the TPC, Z0, D0 and the χ^2 per degree of freedom for the track fits, using tracking algorithms described in[53]. These parameters are used as a basis for track selection. Good charged tracks were required to satisfy the following criteria :

1. The polar angle must be greater than 18.2^o ($cos\theta < 0.95$). This ensures that at least 6 TPC pad rows are traversed.

2. The distance of closest approach of the reconstructed tracks along the beam from the collision point (Z0) must be less than 10 cm, and that in a plane perpendicular to the beam line from the collision point (D0) must be less than 2 cm. More strict cuts of Z0 less than 5 cm and D0 less than 2 cm are applied if the event consists of only two tracks.

3. At least 4 reconstructed coordinates per track are required.

4. The track momentum must be greater than 0.1 GeV/c.

These limits on D0 and Z0 help to eliminate some background from cosmic rays, beam-gas and beam-wall interactions and photon conversions initiated at the ITC and TPC walls . Distributions of some of the above parameters for the data and Monte Carlo are shown

Cut	Value	Data Track rejection rate	Monte Carlo Track rejection rate
		10235	30849
TPC hits	4 hits	7205	27750
Vertex cut			
D0,Z0	2,10 cm	5005	23999
Track Angle	18.2°	4921	23543
Momentum	0.1 GeV	4921	23543
combined		4921	23543

Table 5.1: Effects of track cuts in the track selection criteria

in Fig.5.2. The effect of these cuts on track rejection is illustrated in Table 5.1. The reconstruction efficiency of isolated tracks was measured by selecting e^+e^- pair events defined by ECAL clusters of more than $35GeV$ energy with $|cos\theta| < 0.95$. The fraction of these for which both tracks were reconstructed was found to be $99.0 \pm 0.6\%$, in good agreement with the predicted fraction from a Monte Carlo simulation of $99.2 \pm 0.1\%$[56].

5.2.2 Tau Preselection Cuts

Through the physics run of LEP in 1989 and 1990, data from about 200K Z^0 decays were collected by the ALEPH detector. Most of the data were taken at the Z^0 peak energy, the remainder at 1, 2, and 3 GeV above or below the peak. The leptonic events are selected from the set of runs declared good for physics among the analysis groups in the ALEPH collaboration. All events must pass the ALEPH standard high voltage and trigger requirements. The distinctive features of l^+l^- pair production in Z^0 decays are low multiplicity and back-to-back topology. These are used as the basis of the "CLASS15" sample selection. To reduce the background from hadronic Z^0 decays, two-photon decays and cosmic rays, extra cuts are applied. The following cuts are applied to produce the lepton data sample of the tracks declared good from the previous section:

- **Multiplicity Cut:** The event is required to have from 2 to 8 good reconstructed tracks.
- **Two-Jet Topology Cut:**

  The event is divided into two hemispheres defined by a plane perpendicular to the thrust axis **T** where the unit vector **T** is chosen so as to maximise

$$\frac{\sum_{i=1}^{n} \mid \mathbf{T} \cdot \mathbf{p_i} \mid}{\sum_{i=1}^{n} \mid \mathbf{p_i} \mid} \tag{5.1}$$

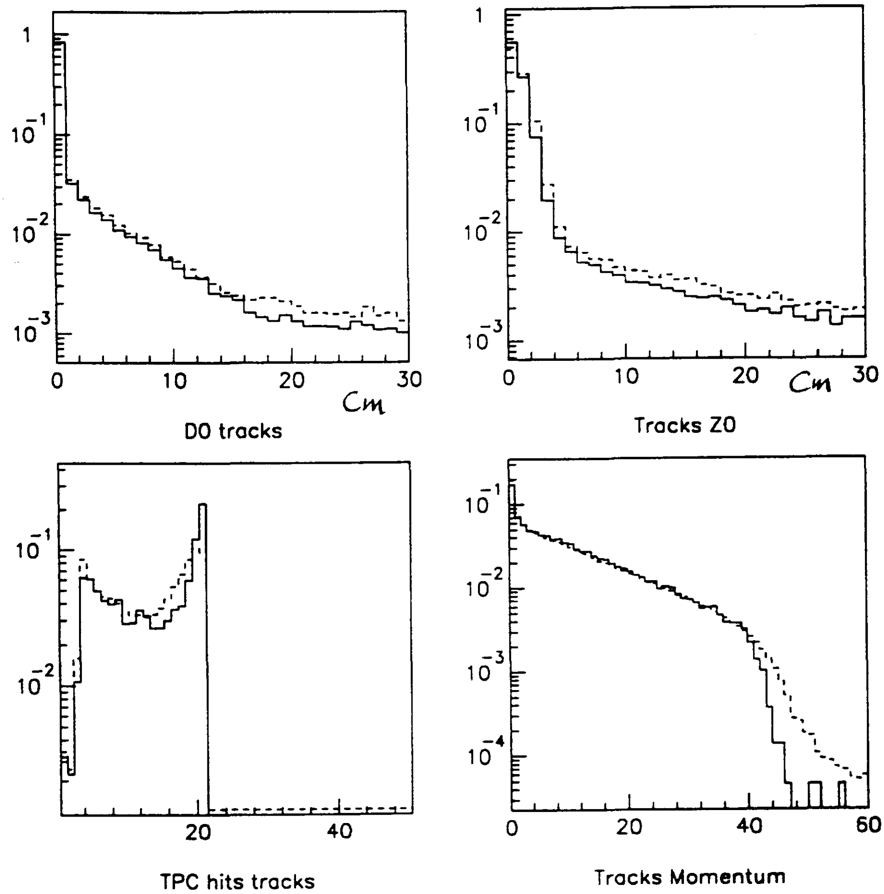

Figure 5.2: Track parameter distributions

where p_i is the momentum of the ith particle. The cut required the event to have at least one good track in each hemisphere.

- **Momentum Cut:** At least one good track in each hemisphere must have a reconstructed momentum greater than 5 GeV/c.

- **Jet Opening Angle:** Events with more than 4 tracks are rejected if any of the tracks has an angle greater than 18.1 degrees with respect to the vector sum of the track momenta in the same hemisphere.

- **Vertex Cut :** In the case when the event has only two tracks then they must originate from the beam crossing within 5 cm along the direction of the beam and 1 cm in the plane transverse to the beam direction.

- **Timing Cut :** For the 1990 data the event has to have 1 ITC z-coordinates associated to any good track. This ITC information was not available in the 1989 data.

- **Acollinearity Cut:** The acollinearity angle must be smaller than 20 degrees. The acollinearity angle(η) is defined to be complementary to the angle between the momentum vector sum of the charged tracks in each hemisphere.

- **Invariant Mass Cut:** The centre-of-mass energy of the reconstructed charged tracks, calculated assuming pion masses, must be larger than 4 GeV.

- **Angular Cut:** The event has to satisfy $-0.9 < cos\theta^* < 0.9$ where θ^* is the centre of mass scattering angle defined by

$$cos\theta^* = cos\frac{1}{2}(\theta_1 + \pi - \theta_2)/cos\frac{1}{2}(\theta_1 - \pi + \theta_2) \tag{5.2}$$

  where θ_1 and θ_2 are the polar angles of the vector sum of the track momenta in each hemisphere. The advantage of this variable is that the angular distribution of the final state becomes independent of whether or not radiation takes place in the initial state. The θ_1 and θ_2 polar angles are associated with the positive and negative charge of the produced lepton pair. The charge is computed by adding the track charges in each hemisphere. In case of ambiguity, the track with the highest momentum determines the charge of the hemisphere.

Details of the influence of preselection cuts are discussed in the next section.

5.2.3 τ pair Selection

The acceptance of the selection is defined by the acollinearity cut and the cut on the scattering angle θ^* of the τ^- with respect to the electron, computed in the centre-of-mass reference frame of the two incident particles (angular cut). This angle is computed on the assumption that at most one hard photon is emitted from initial lines; in this case it depends on the polar angle of the two taus measured in the laboratory frame, as described in the previous section.

The polar angles of the taus cannot be measured since they decay very close to the interaction point. Instead the "jets" of the charged particles produced in their decays are measured. The jet scattering angle is taken to be approximately the tau scattering angle.

This approximation does not affect the cross section, but introduces a correlation between the "acceptance" and the "selection efficiency" since the decay product of the taus cannot always be detected.

The angular acceptance of the TPC, described in Section 5.2, does not reduce the acceptance defined by the acollinearity and angular cuts since the largest possible value of $cos\theta$ for an event with $|cos\theta^*| < 0.9$ and $cos\eta < -0.9397$ is 0.94 and the $cos\theta$ track cut corresponds to $|cos\theta| < 0.96$.

Track selection cuts are very effective in eliminating the beam-gas, beam-wall and noise related background by requiring that the tracks come from the interaction region and have to have a momentum of at least 0.1 GeV/c. Further background reduction is achieved by the implementation of topology and momentum cuts.

Preselection cuts are designed to eliminate other backgrounds such as $Z^0 \to$ hadrons and $\gamma\gamma$ events. Hadronic events are rejected by requiring low multiplicity and small opening angle for events with more than 4 tracks. The $\gamma\gamma$ events are rejected by a set of kinematical cuts. Most of these events are eliminated by requiring that at least one track has a momentum greater than 5 GeV/c, Fig.5.3. An additional invariant mass

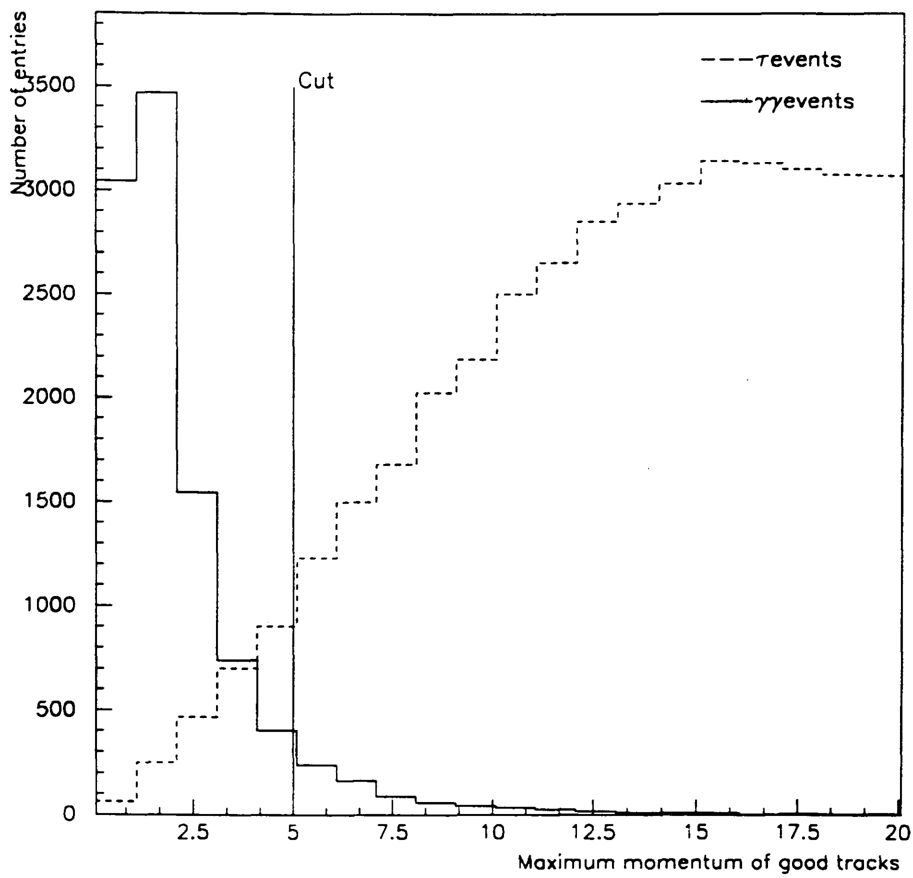

Figure 5.3: Maximum track momentum in the event

cut is also applied to the data since this cut is used in the Monte Carlo two-photon generator programs. Rejection of cosmic rays is accomplished through the implementation of various cuts, with a first reduction arising from vertex requirements for good tracks (track selection cuts). In addition more restrictive vertex requirements are applied for at least one of the tracks in two track events as given above. Also, the events are required to have at least 3 ITC coordinates associated to a track. This is a powerful tool for the rejection of cosmic ray events, since the gate of the ITC with respect to the beam crossing is quite tight , about 400 ns, much narrower than the $\sim 45\mu s$ gate of the TPC.

Finally the following three cuts are applied to eliminate $Z^0 \to \mu^+\mu^-$ and $Z^0 \to e^+e^-$ events.

(a) Missing Mass Cuts

1. **The total charged momentum cut**

The sum of energies of the tracks (assuming pion masses) has to be smaller than $100(2E_{beam}/m_Z)GeV$.

2. **The missing mass cut**

   The square of the missing mass calculated from the tracks, (assuming pion masses) and the known centre-of-mass energy is required to exceed $400GeV^2$

3. **The total ECAL wire energy cut**

   The ECAL energy measured with the wires must be smaller than 55 GeV. $E_{wires} < 55(2E_{beam}/m_Z)GeV$

The main cut is the missing mass cut. Tau events are identified through the large invariant mass of the two (unseen) neutrinos produced in the decay of the two taus. Moreover only charged tracks are used. Muon pair and e-pair events have missing mass ~ 0 even when one radiative photon is present in the initial or final state. The cut on the sum of the energies of the charged tracks provides a guarantee that large missing mass is not faked in events with badly measured tracks. A constant fraction of e^+e^- events has two photons in the final state. These events can have a large missing mass. To reduce this background to a negligible level the cut on the total ECAL energy is applied.

(b) Cuts on the opposite hemisphere

1. **Bhabha rejection:**

   The track is required first not to point into a crack or an overlap region in ECAL. The ECAL wire energy is summed over a hemisphere and if the ratio of the energy sum to the beam energy is greater than 75% then the event is rejected.

2. **Muon-pair rejection:**

   A track in a hemisphere is considered to be part of a muon pair if its momentum is greater than 90% of the beam energy or if it is a m.i.p. in ECAL, has a narrow shower in HCAL and has momentum greater than 90% of the beam energy.

The two cuts are described in more detail in the discussion of the background to the tau given in the next section.

5.2.4 Background to the tau event selection

The τ sample was selected using the cuts described in the previous sections with small background from other types of event. To measure the cross-section of the τ decays, and more importantly for the polarization measurement, it is important to assess possible contributions to the tau pair sample from events which are not due to Z^0 decays into τ pairs.

The possible background contribution from such sources is described below.

Hadronic background

Although the hadronic background which passes the cuts described in section 5.2 and 5.3 is expected to be very low, the background must be studied carefully due to the larger cross-section of the decay $Z^0 \rightarrow q\bar{q}$ which is nearly 21 times larger than that of the decay $Z^0 \rightarrow \tau^+\tau^-$. Possible contaminations have been estimated using Monte Carlo techniques. Hadronic events were generated with the LUND generator[55]. The generated events were passed through the GALEPH detector simulation and reconstructed with JULIA as described in chapter 4. These events were then subjected to the selection cuts used for tau sample selection.

Hadronic events can usually be easily distinguished from τ pairs from the large number of charged tracks associated with the hadronic events, see Fig.5.4, although an insignificant

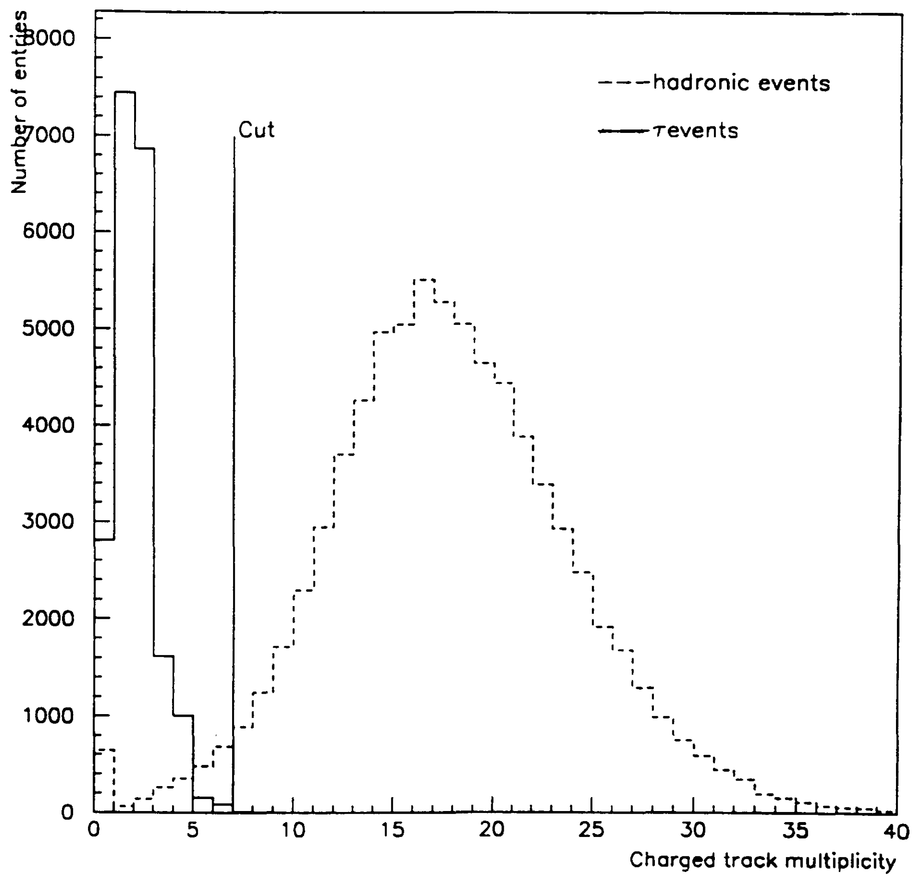

Figure 5.4: Charged tracks multiplicity cut

number of tau events with a large number of charged tracks have been observed in MC data, caused by pion scattering at the walls of the ITC and TPC, as shown in Fig.5.5.

By applying the multiplicity cut the background is cut significantly but the tau sample is still contaminated with low multiplicity hadronic events due to the large cross-section of the hadronic decays. The background from hadronic events is reduced to about 2%

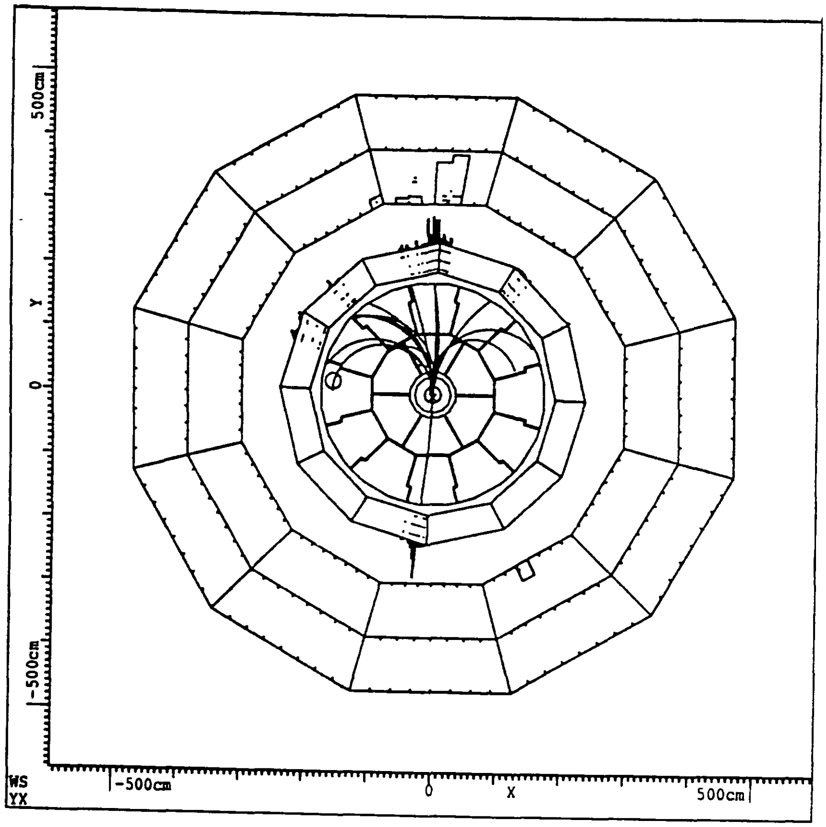

Figure 5.5: Pions scattering at the ITC and TPC walls

of the original hadronic events subjected to this cut. The background to 1 prong tau decay channels is reduced to a negligible level by introducing the same cut, this time on the individual hemispheres, where the event is divided into two hemispheres defined by the thrust axis described in section 5.2. Taking into acount the large cross-section of the hadronic decays, the level of background is very high. It is cut further, however, by the jet opening angle restrictions and the maximum track angle cut. At this stage only 128 hadronic events survived out of 76K. Further reduction is achieved through the rest of the tau preselection cuts and the tau selection cuts. Only 37 events survived all these cuts, so the percentage contamination to the tau sample from hadronic events is quite small, about$(0.9 \pm 0.14)\%$.

Muon-pair background

These events are expected to show a signature in the ALEPH detector of a back-to-back pair of particles with very high momenta. This is due to the fact that muons cross the detector almost without any interaction, and the energy they deposit in the calorimeters is that of a minimum ionizing particle (m.i.p.). Accordingly, such events are rejected from the tau sample. First a search is made for the candidate of the highest momentum in the event. If it has characteristics compatible with those of a muon, (e.g. penetrating HCAL with a narrow shower width and m.i.p.-compatible energy in ECAL) and if in the opposite hemisphere a track has a momentum greater than 0.9 of the beam energy then the event is classified as a muon pair. The background was calculated using both Monte Carlo(MC) and real data and it was found to be (0.1 ± 0.02) in MC while it was (0.13 ± 0.09) using the real data.In the second sample both muon candidates had to have passed the penetration cuts in HCAL in addition to having hits in muon chambers.

Electron-pair background

Since electrons start showering much earlier than other particles on hitting a material they are expected to deposit a large fraction, if not all of their energy in the electromagnetic calorimeter. Since the ECAL energy measurement is the main requirement for the rejection, the event to be defined as an electron pair should not have a track pointing to an ECAL crack or overlap region. To insure that all radiative photons will be detected by ECAL the impact point of straight line extrapolation of the track direction to the ECAL region must not be in a crack or overlap region. Finally the energy measured with ECAL wires must be less than 80% of the beam energy. The background was calculated using both Monte Carlo(MC) and real data and it was found to be (0.1 ± 0.04) in MC while it was (0.1 ± 0.06) using the real data.

Two Photon Background

Background from two-photon interactions is expected to be very small due to the stringent requirements on topology and the cuts on the transverse momentum, acollinearity and invariant mass. Adding the last cut is important because the Monte Carlo data files were generated with centre of mass greater than 4 GeV. Possible contamination from different types of two photon events was investigated using Monte Carlo techniques. Monte Carlo events of the type $e^+e^- \rightarrow e^+e^-(f^+f^-)$ were generated using the generator PHOT01. Two-photon backgrounds to the tau sample were studied using these MC data. The same set of cuts applied for the tau selection was applied here. The results from different types of two photon processes are listed in table 5.2.

The cross-section for the two-photon process is large, but most particles are produced with small angles relative to the beam and never enter the detector. The contribution from the process $e^+e^- \rightarrow e^+e^-q\bar{q}$ is negligible, but there is a small contamination from the process $e^+e^- \rightarrow e^+e^-l\bar{l}$. TPC cuts are quite effective in the rejection of the two-photon events, the number of events passing these cuts drops to less than 40% of the total number of events used. The strict vertex cut applied to events with two tracks combined with minimum momentum, jet opening angle and acollinearity cuts reduces the background to an insignificantly low level. Tau selection cuts are not very effective to cut this type of event. The total number of events surviving the cuts from the process $e^+e^- \rightarrow e^+e^-l\bar{l}$

Source of Background	Selected Events	Cross section(pb)
$e^+e^- \rightarrow e^+e^-e^+e^-$	66	3.3 ± 0.41
$e^+e^- \rightarrow e^+e^-\mu^+\mu^-$	137	6.8 ± 0.58
$e^+e^- \rightarrow e^+e^-\tau^+\tau^-$	62	3.1 ± 0.39
$e^+e^- \rightarrow e^+e^-q\bar{q}(u,d)$	0	0.0
$e^+e^- \rightarrow e^+e^-q\bar{q}(s)$	0	0.0
$e^+e^- \rightarrow e^+e^-q\bar{q}(c)$	0	0.0

Table 5.2: Two photon Background

was found to be 224 events from 60k. The Monte Carlo set of events was composed of 20K of each type of lepton, equivalent to cross sections of 3.706 nb, 2.0569 nb, and 0.4984 nb for electron, muon, and tau types respectively.

5.2.5 Selection Efficiency

The selection aim is to get the efficiency of selecting tau events as high as possible with a minimum of background events from other processes as described in detail in the previous sections. The efficiency is estimated using a MC data set of 90K tau events generated by KORALZ, passed through the detector simulation program GALEPH and reconstructed by JULIA. Similar sets of MC data were produced for the estimation of background from other processes as described before, using the appropriate MC generators. All sets of events were generated over the same range of energies in the vicinity of the Z^0 peak. Inefficiencies from the detector acceptance are included in the selection efficiency. The tau event selection efficiency was found to be $(71.1 \pm 0.81)\%$. The overall efficiency which determines the tau cross section depends on the selection efficiency, trigger efficiency and the track efficiency. The last two were measured and were found to be very close to unity; $(99.3 \pm 0.7)\%$ and $(99.85 \pm 0.05)\%$ respectively.

5.2.6 Selection of the decay $\tau \rightarrow \pi\nu_\tau$

The pion sample is extracted from the tau sample selected according to the criteria discussed in the previous section. Pions may leave various signatures in the ALEPH detector depending on the way they interact. They may start to produce a hadronic shower as early as the beginning of ECAL, and all the way to the end of HCAL.

Accordingly the pion could fake the signatures of both electrons and muons, so the separation of pions from electrons and muons in the tau sample is not an easy task. In addition to these two leptonic decay channels, there is ambiguity between the pion and some other one prong tau decay products such as $\tau \rightarrow \rho\nu$, $K^*\nu$, as we shall see later in this chapter. To achieve maximum purity of the pion sample, various cuts are implemented on the signals coming from almost all of the ALEPH subdetectors. These cuts must not create any bias against pions when separating them from other decay channels which could contaminate the pion sample, mainly $\tau \to e\nu\nu, \mu\nu\nu, \rho\nu$, and $K^*\nu$. The pion candidate is defined according to the pattern of energy deposition in the calorimeters. The track to be selected as a pion candidate before applying any cuts must satisfy the following requirements:

Charged Track Selection

1. There must be only one good charged track per hemisphere which satisfies the good charged track requirements described in section 5.2.1, and no other bad tracks within 52^o of the good track. This cut leads to a loss of 2% of the pion signal as measured from MC.

2. The track must not point to a crack between ECAL modules or into the overlap region between the barrel and the endcaps. A further loss of 10% of the pion signal is caused by this cut, but neither cut biases the pion energy spectrum. The latter loss was also measured from MC data.

3. There must be at least one track in the event with a momentum ratio to the beam energy greater than 0.1.

The first two cuts described above are very effective against multi-prong tau decay channels and also decays like $\pi^{\pm} n\pi^o$ where one or more of the π^o photons has converted. The last cut reduces the 2γ background to a negligible level.

Calorimetry Selection

Tracks passing the above criteria represent the one prong tau decay channels $\tau \to e\nu\nu, \mu\nu\nu, \pi\nu, K\nu, K^*\nu, \rho\nu(\pi\pi^o\nu)$, and $\pi n\pi^o$. In this analysis no attempt is made to distinguish between the the decay modes $\pi\nu$ and $K\nu$. Decay modes which include electrons and π^o's (photons) in their decay products can be easily detected by the presence of a shower which develops in the first few radiation lengths in ECAL. For the decay mode $\mu\nu\nu$, with the high penetration capability of the muons, HCAL will be perfect for their recognition. Certain cuts were implemented in ECAL and HCAL for the separation of the pion decay channel from the above group as described below.

1. **ECAL Cuts**

   The high granularity of the electromagnetic calorimeter allows the precise measurement of the longitudinal and transverse shower profiles in the calorimeter, so it can detect and distinguish between different energy profiles of showers. The point where the shower started can be easily determined. ECAL is segmented in depth into 45 layers (sections of $\sim 0.5X_o$), where the wire planes are read out separately. To determine the shower starting point in ECAL, the track is first extrapolated to the ECAL modules and the wire profiles of the ECAL module hit by the track and its neighbours are examined. Summing the signals over such a wide angle will ensure the detection of any photons accompanying the charged track. The shower starting point is defined by the first three adjacent wire planes having signals greater than 2.5 MIP, where MIP is the energy deposition expected from a minimum ionizing particle. Typical shower starting depths for e, μ, and π simulated data are shown in (Fig.5.6 a-c), while the same distribution measured in a pion test beam is shown in (Fig.5.6 d). Electrons and ρ events are removed by requiring a shower starting

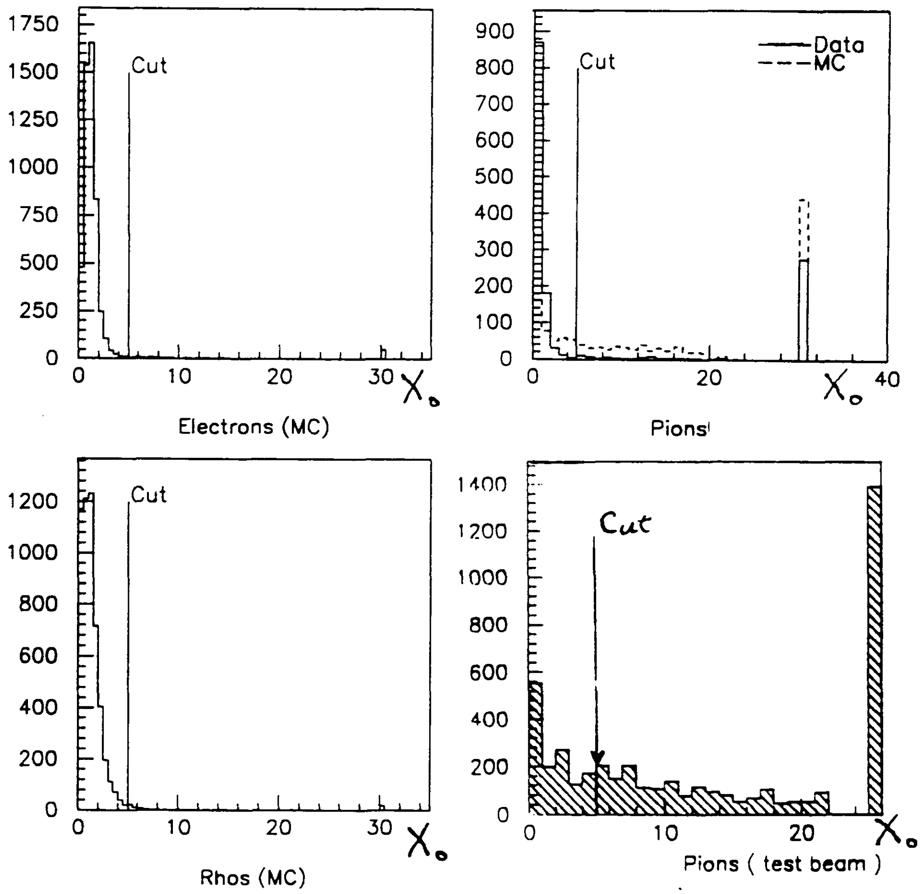

Figure 5.6: Shower Starting point in ECAL

point for the pion candidate to be at a depth greater than $5X_o$. Events passing this cut are contaminated by less than 0.15% of electrons and $(1.6 \pm 0.2)\%$ of the ρ events. The latter is mainly due to photons going into ECAL cracks and due to late development of electromagnetic showers or to their having too little energy to pass the threshold.

2. **HCAL Cuts**

   The digital readout of the HCAL is used to reject the muon decay mode of the tau. The track is extrapolated through HCAL taking into account the effect of multiple scattering and the magnetic field in the iron. Two "roads" of different widths are opened around the extrapolated track,(c.f. Fig5.7). The narrow road is used to reject muons depending on their penetration capability, while the other is used to

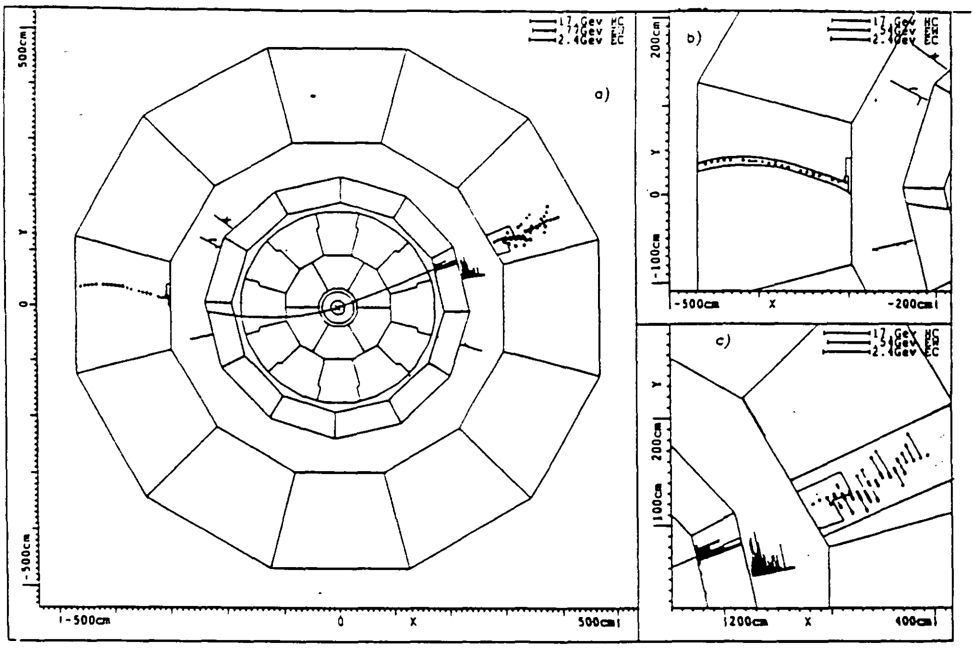

Figure 5.7: Road width around the extrapolated charged track in HCAL

measure the shower width in HCAL.

The main cut against muons uses their characteristic penetration without interaction to the last layers of HCAL. In the narrow road a search is made for the tube hits in the last five planes of HCAL.

In the wide road ($\pm 50cm$), in each plane the distance between the most widely separated pair of hit tubes is measured. The mean distance of the track from the hits in the last 5 planes is calculated (D_{far5}), providing that the number of planes is greater than one. The mean is expected to be large for a particle interacting in HCAL such as the pion and to be narrow for muons. Such behaviour is displayed in (Fig.5.8a and b). D_{far5} is required to be greater than $3 \times (1cm + \sigma_{MS})$. Also the fraction of all hit planes in which there is a pair of hits separated by more than 6 cm, F_{wide}, is measured , then a cut of F_{wide} greater than 0.2 is applied Fig.5.9. This cut is applied only if the sum of energy deposited in the four towers of ECAL nearest to the track in stacks 2 and 3 E_{23}, is less than 1.2 GeV as illustrated in Fig.5.10. It relies on the fact that most of the low energy pions deposit their energy in ECAL before reaching HCAL and so do not have enough energy to penetrate through

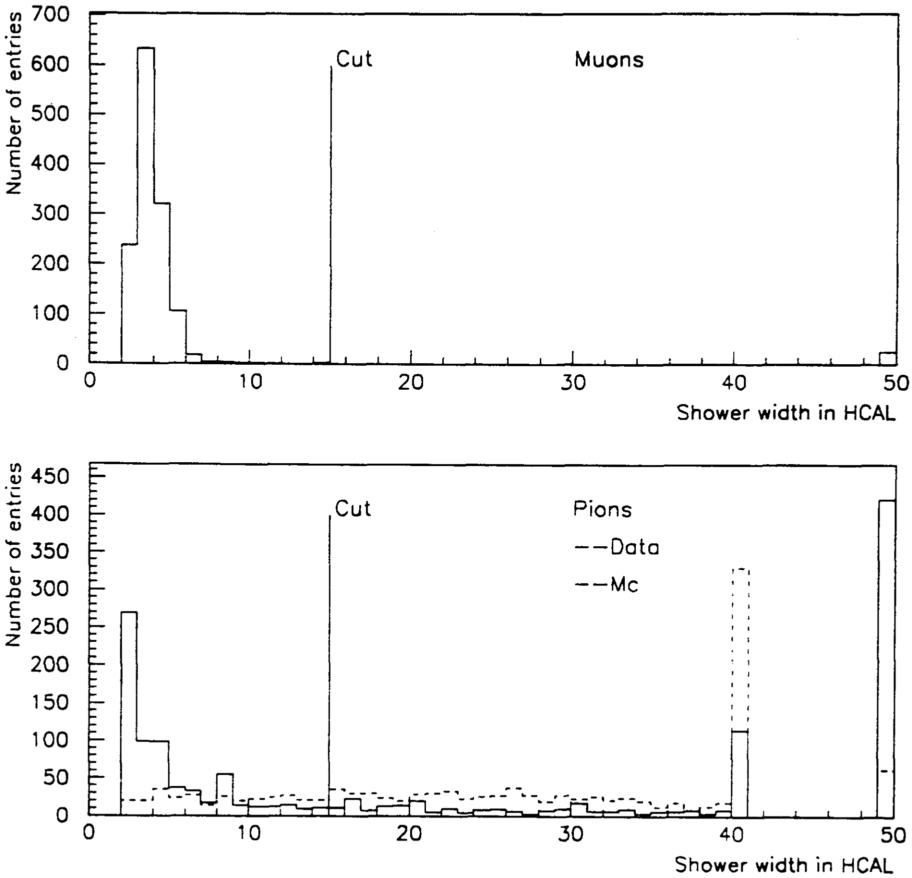

Figure 5.8: Shower width in the last 5 HCAL planes

HCAL. These cuts were varied to optimize pion efficiency and muon rejection.

3. **Energy Balance Cut**

   The aim of this cut is to reduce further the background from the decay modes $\rho\nu$ and $K^*\nu$ using the summed energy of all HCAL clusters associated with the track and the ECAL energy measured with the wires, (E_{calo}). The ratio of E_{calo} to the track momentum must be less than 2.0 for the pion candidate. This is displayed in Fig.5.11.

4. **Cuts on the opposite hemisphere**

   These cuts are used to reject electron and muon pairs, as described in section 5.1.3. The distributions of ECAL wire energy opposite the pion candidate and that of the muon momentum are shown in Fig. 5.12,13.

The effects of these cuts, implemented on both Monte Carlo and real data, are shown in Table5.3.

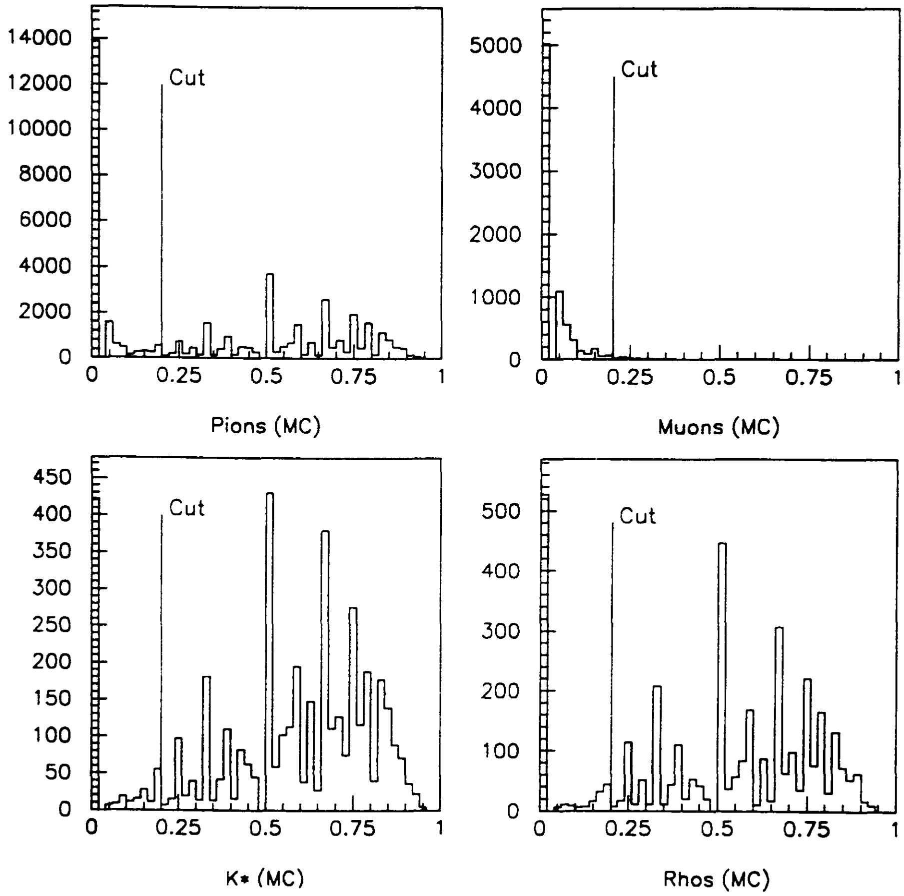

Figure 5.9: F_{wide} in HCAL

List of the cuts	Data	MC π	MC ρ	MC K^*	MC μ	MC others
Class15 (data)	35448					
Generated (MC)		10818	20664	1440	16182	40950
TPC and opposite hemisphere cuts	8775	7659	12708	782	8674	134316
$x_\pi > 0.1$	7731	6999	10683	652	7427	11302
No ECAL crack or overlap	5561	6258	9650	590	6651	9828
Shower start $> 5X_0$	1737	4370	145	131	6198	11
$E_{calo} < 2.0$	1728	4316	124	66	6198	6
Muon penetration	910	4197	112	63	388	5
Muon width	706	4002	106	62	16	5

Table 5.3: Tau mode rejection in the tau pion selection procces

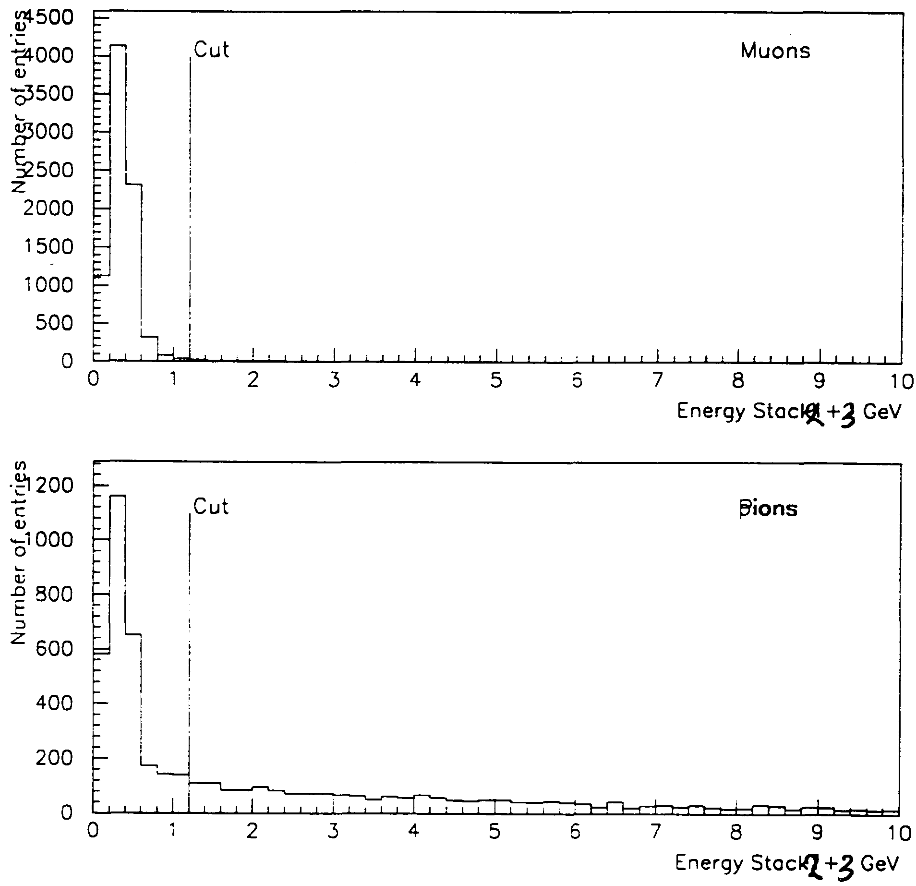

Figure 5.10: Shower energy in stack 2 and 3

5.2.7 Radiative Effects

In the tau decay to a pion plus neutrino, the energy of the tau is slightly lower than that of the beam energy due to initial and final state radiative effects. ECAL cuts applied for the pion candidate selection are very effective in eliminating the final state radiative effects and also in eliminating photons from initial state radiation. To study any remaining effects from the initial state radiation, Monte Carlo data at the generated level are used. Events are generated with KORALZ for a range of beam energies. Cuts similar to those for the pion selection are applied, the most important being the acollinearity and the scattering angle cuts (section 5.2.2) and demanding that there be no photon with energy greater than 0.2 GeV in ECAL within 1 radian of the pion direction. The ratio E_τ/E_{beam} is plotted in Fig.5.14 before and after the cuts. The mean value of E_τ is used for x_π calculations.

5.2.8 Systematic Effects

It has been shown that the cuts applied to select the tau event sample do not bias the pion momentum spectrum. More important are the cuts implemented to select the pion

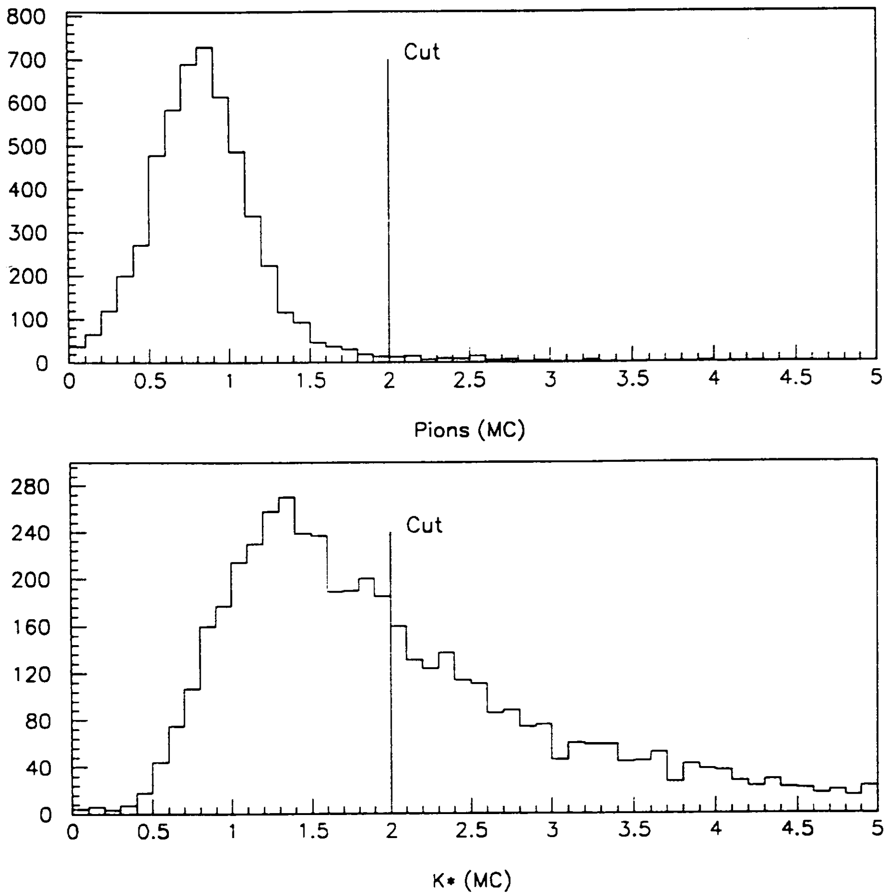

Figure 5.11: Energy balance E_{calo}/P

candidate, from which the decision is taken on the tau decay mode. These cuts are described in section 5.2.6. The most effective are the ECAL and HCAL cuts. Due to the fact that the pions do not have a unique signature in the ALEPH detector, background is expected from other decay channels which are wrongly identified as pions, in addition to the pion misidentification itself. These cuts change the percentage of background contamination in the pion sample. The ratio of the number of correctly identified pions to the the number of generated pions, the pion acceptance, is estimated as a function of momentum using Monte Carlo simulated data. This acceptance has to be checked with real data. There is evidence that pions with low energies are not well simulated, for example the shape of the R_3 estimator described in section 4.5.2. There are also some defects in the simulation of low momentum muons in tau decay.

There are two sources of real pions from which the acceptance can be checked

- **Test Beam Data**

  In 1987 and 1988 some ECAL and HCAL modules were tested using a beam of pions covering a range of energy from (3-30)GeV. The performance of some modules from both calorimeters was checked, and pion acceptance measurements made[60].

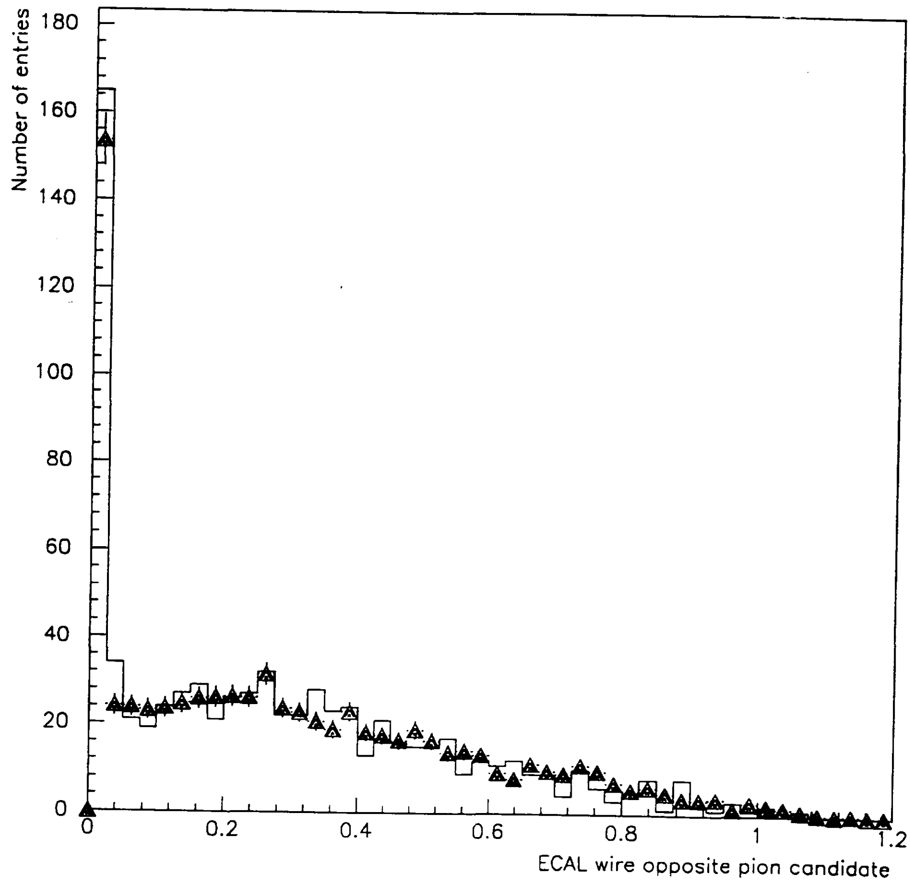

Figure 5.12: ECAL wire opposite pion candidate

- **Pions from the decay** $\tau \rightarrow \rho\nu_\tau$

  These events are selected from the tau sample by requiring what is expected from such a decay, a single charged track accompanied by a pair of γ's. So events must have a single charged track well associated with an ECAL cluster in one hemisphere and in addition there must be one or two neutral clusters identified as photons[61]. The invariant mass of the charged track and the photons must be compatible with that of the ρ meson. The invariant mass of the ρ events from which the test pions were taken is displayed in Fig.5.15

  Two different photon identification criteria[61, 62] produce the same sample of clean pions from the ρ.

Since the polarization is extracted from the pion momentum spectrum, the energy calibration will affect the final results. Detailed studies of momentum distortions have been made[63]. Systematic displacements of the track sagitta are observed for positive and negative particles at different angles. The overall shift in the pion momentum distribution is negligible. The systematic effects of the calorimeter cuts on the pion acceptance are described separately in the following two sections.

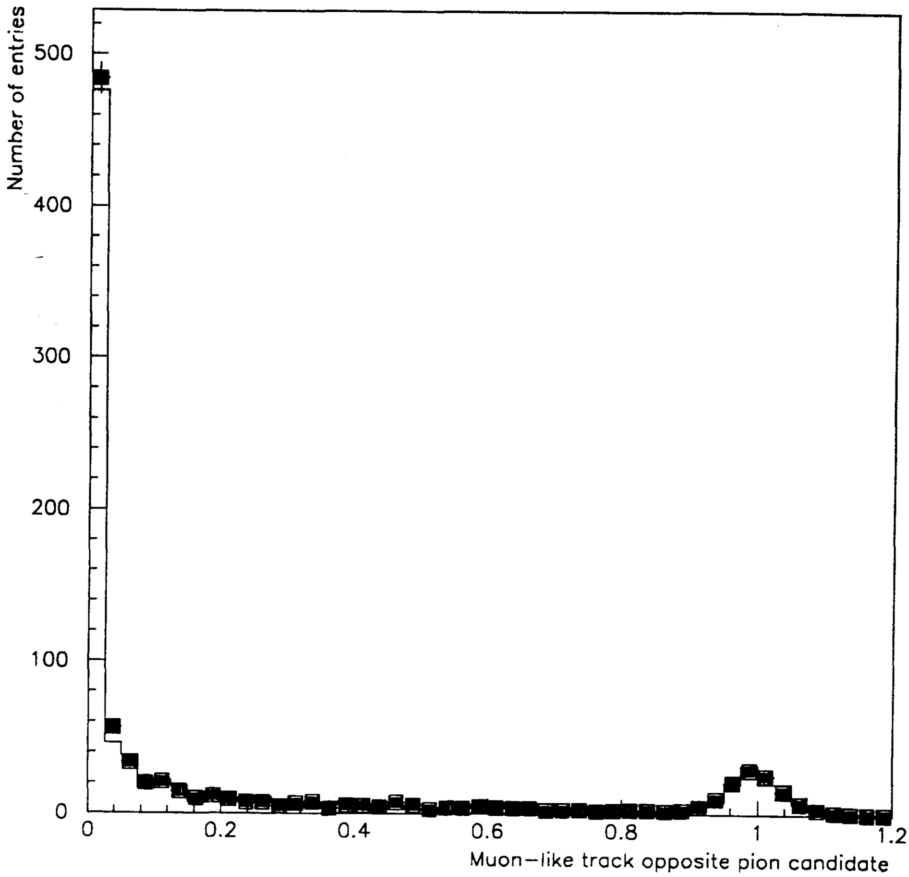

Figure 5.13: Muon-like tracks opposite pion candidate

ECAL Cuts

The effect of these cuts on the acceptance is studied using the test beam data, compared to MC data simulated with GALEPH under the same circumstances. Results were found to be in good agreement, especially for x_π greater than 0.2, where $x_\pi = E_\pi/E_{beam}$. It is believed that the disagreement at low energies is due to the low energy behaviour of the pion interactions in ECAL which is not well simulated. Clean pion samples from the ρ decay mode can not be used to check the ECAL acceptance of this cut since photons produce showers early in ECAL. From the comparison of the acceptance from data and MC, the systematic error on the polarization is ± 0.033[59].

HCAL Cuts

Two cuts use HCAL digital readout for pion selection, the first is completely HCAL dependent while the second uses ECAL readout in addition and is applied only if the energy of an ECAL cluster was less than 1.2 GeV. The probability of passing the first cut from data is compared to that of MC in Fig.5.16. The acceptance is good except at low energies, for which the penetration cut would result in a poor acceptance. For this

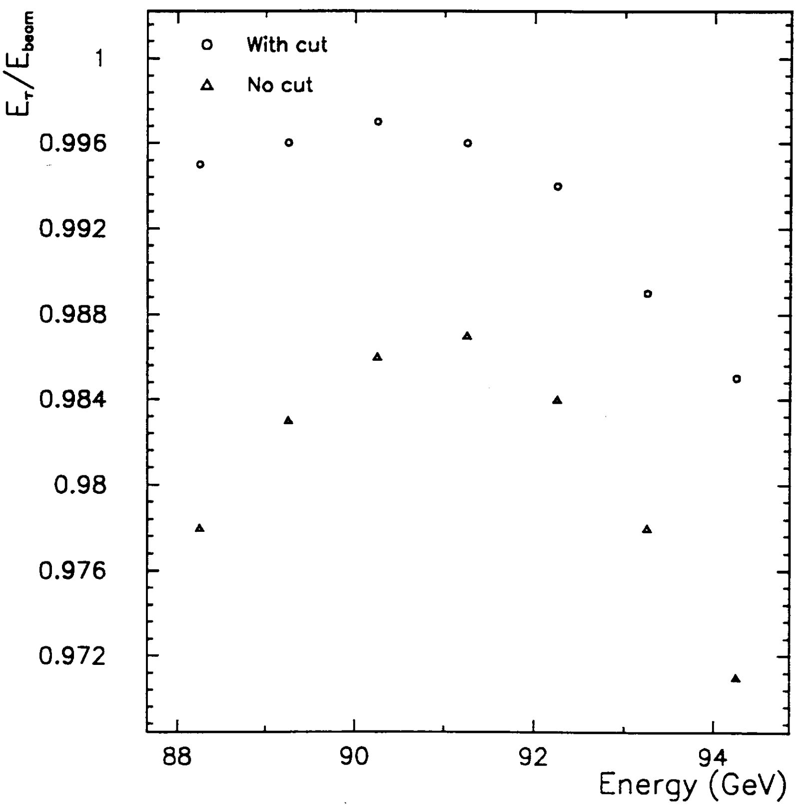

reason, the second cut was implemented. It depends on the fact that low energy pions interacting in ECAL will have only a small amount of energy to release in HCAL. The acceptance variation was checked for the penetration cut only through a straight line fit to the DATA/MC ratio versus momentum. This resulted in a slope of (-0.039 ± 0.092). Since this is compatible with zero, no correction was made but the uncertainty is taken as a measure of the corresponding systematic error.

Systematic errors in the Background

The cuts described in the previous sections do not eliminate completely the contamination to the pion sample from other decay channels, which are the main source of the background. In addition, a very small background results from electron and muon pairs. The background from such sources must be taken into account. Systematic effects of such a background are summarized below:

1. **Background from the decay $\tau \to \mu\nu\nu$**

   Muons are rejected using the HCAL cuts described before. The systematic error due to this cut is estimated from the probability of muon misidentification. The

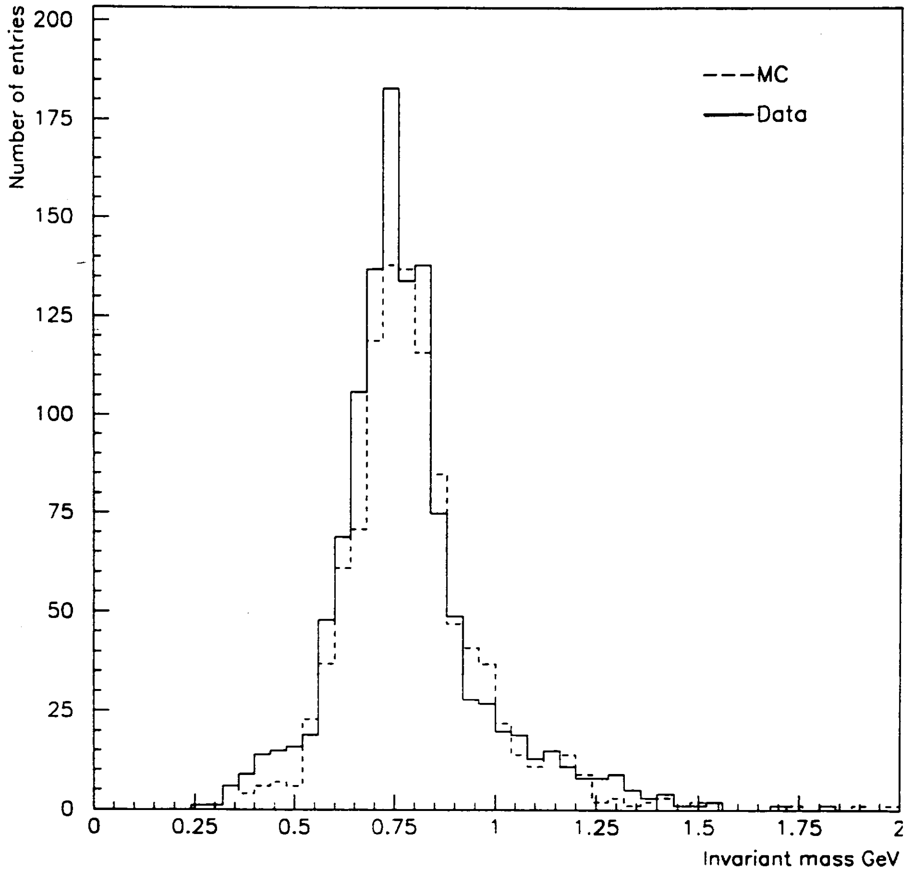

Figure 5.15: The invariant mass of the ρ candidate

efficiency of the cuts used against muons is measured with muon tracks tagged by the presence of a muon above 40 GeV in the opposite hemisphere. Such an efficiency is not well described by MC. The fractional discrepancy between MC and data is of the order of (0.007 ± 0.001) in 1989 and 1990 data. The muon misidentification probabilities were found to be $(0.629 \pm 0.059)\%$ and $(0.312 \pm 0.029)\%$ in the MC and data respectively. Scanning of the events shows that one source of misidentification is HCAL noise which adds an extra background of $(0.4 \pm 0.08)\%$. This changes the muon background to the pion sample from 0.33 to 0.86%.

2. **Background from the decay $\tau \to \rho\nu$**

   This background is rejected by the ECAL cut, which requires a shower starting point for a pion candidate to be greater than $5X_o$ in depth in ECAL. The reliability of this cut in the data was checked using MC data. When the cut was varied by $\pm 0.5X_o$ in the Monte Carlo, the contamination of the pion sample varied from 1.9 to 3.3%. The uncertainty in the $\tau \to \rho\nu$ branching ratio introduces an additional uncertainty in the polarization.

3. **Background from the decay $\tau \to K^*\nu$**

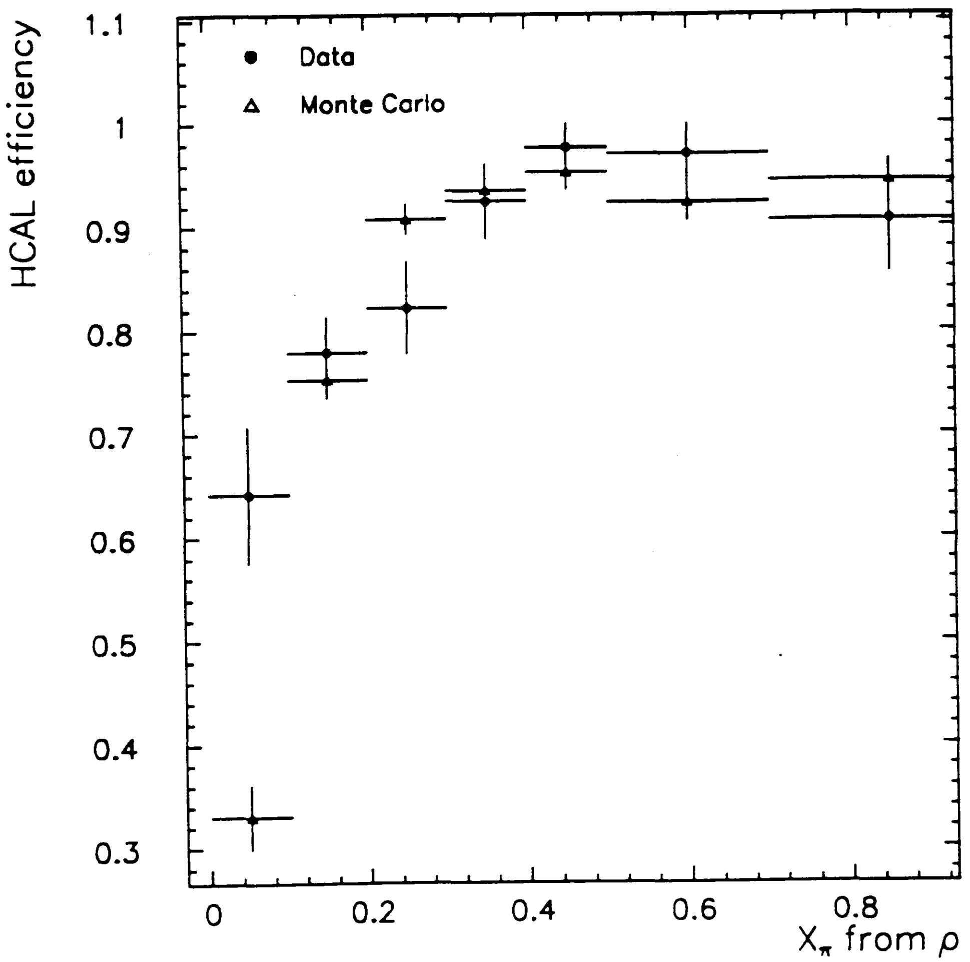

Figure 5.16: HCAL efficiency for the rho pions in data and Monte Carlo

The only cut directed specifically to reduce the background from the decay $\tau \to K^*\nu_\tau$ required the pion candidate to have the ratio of the total calorimeter energy to the track momentum be less than 2. Comparing the mean value for this distribution displayed in Fig.5.17, in the data to that from MC it was found that they differ by 10%. A variation of the cut position changes the background due to both ρ and K^* by a factor of 1.36 from 1.1 to 1.5. Uncertainty in the branching ratio of the decay $\tau \to K^*\nu_\tau$ introduces an additional uncertainty in the polarization.

4. **Background from other τ decay modes**

   The contamination to the pion sample from other tau decay modes is insignificant and their contribution to the systematic error in the polarization measurement is also negligible.

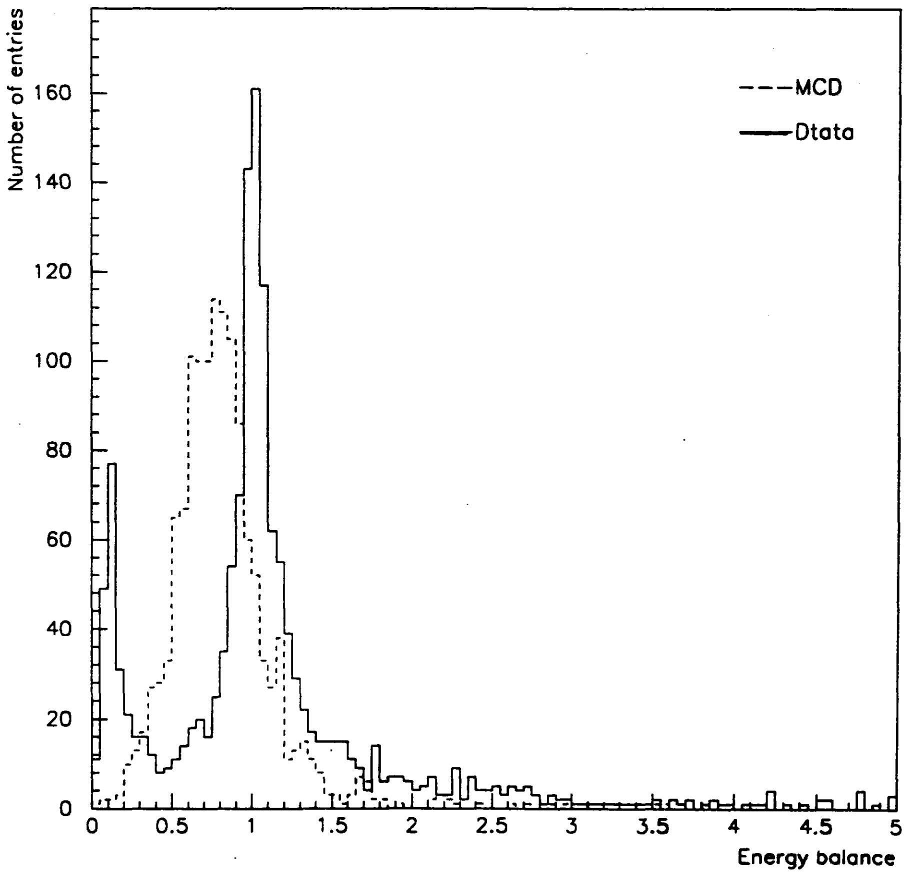

Figure 5.17: Energy balance distribution pions

Chapter 6

Electroweak Analysis

6.1 Polarization Measurements

The measurement of τ polarization depends on the momentum distribution of the decay product. In this analysis the polarization is deduced from the pion spectrum in the decay $\tau \rightarrow \pi\nu$. Previous measurements have performed a least squares fit to the pion momentum spectrum in tau decay[22]. This approach was also used at an early stage of the present analysis to deduce the polarization from equation 2.28, using the raw spectrum of Fig.6.1 corrected to take into account the acceptance and background. The latter is mainly from other tau decay channels. Final results presented below were obtained, however, with a different, maximum likelihood fit described later in this chapter. The maximum likelihood fit was preferred because it enabled a more satisfactory treatment of helicity-dependent background due to misidentified τ-decay channels. The most significant background contributions to the pion spectra from other decay channels are due to ρ,K^* and μ decay channels, in decreasing order of importance.

The acceptance is defined as

$$Acceptance = \frac{N_\pi^{rec}}{N_\pi^{gen}} \tag{6.1}$$

where N_π^{rec} is the number of tracks reconstructed with momentum in bin x, which are correctly identified as pions, and N_π^{gen} is the number of pions generated with momentum in bin x.

The acceptance is plotted as a function of x_π in Fig.6.2. The fraction of background events in the pion sample coming from decay mode m, f_m, is defined as the ratio of (number of events generated as mode m but reconstructed as mode π)/(total number of events reconstructed as mode π). The value of f_m estimated from Monte Carlo was corrected to take into account the systematic effects described in the previous chapter. After subtraction of the background from Bhabha events and muon pairs, the pion momentum spectrum was corrected according to

$$N_{corr} = N_{data} \times \frac{1 - f_\mu - f_\rho - f_{K^*}}{\text{acceptance}} \tag{6.2}$$

The contributions to the background from other tau decay modes are listed in table 6.1. Pions with x_π less than 0.2 are not included in the fit because:

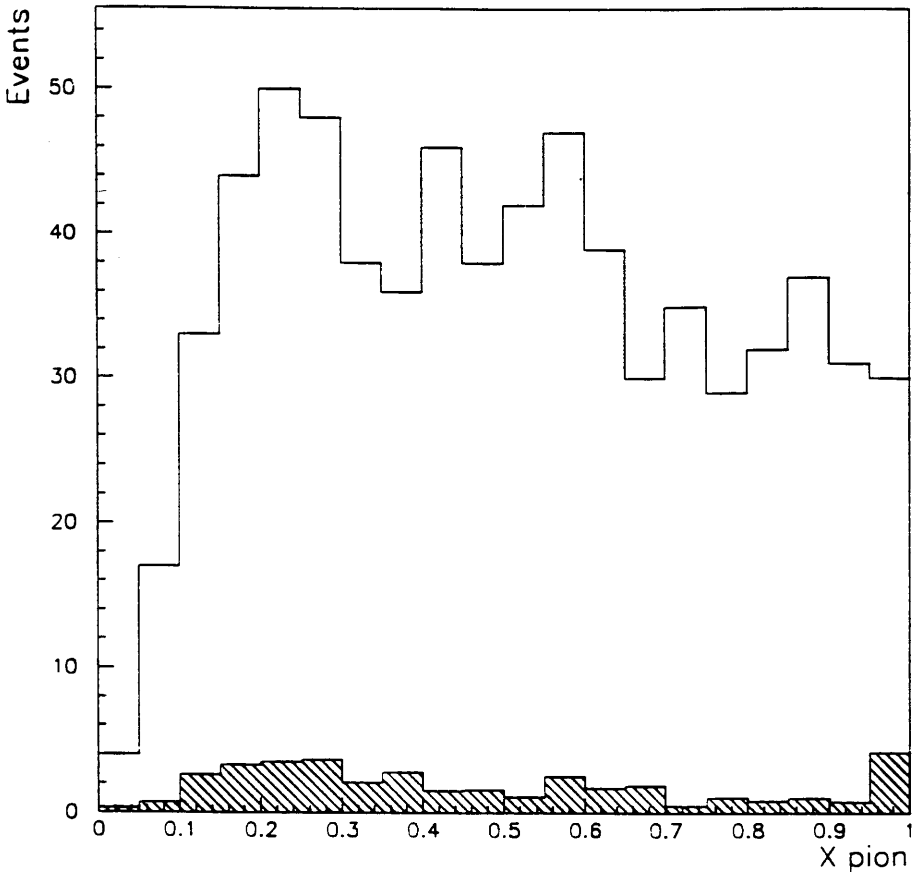

Figure 6.1: Raw pion spectrum,the solid line represents the pion spectrum and shaded area the background

Source of Background	Percentage Background
$\tau \rightarrow e\nu\nu$	0.003
$\tau \rightarrow \mu\nu\nu$	0.05
$\tau \rightarrow K^{*}\nu$	1.3
$\tau \rightarrow \rho\nu$	2.9
Electron pair	0.004 ± 0.001
Muon pair	0.067 ± 0.006

Table 6.1: Percentage Background to the pion sample

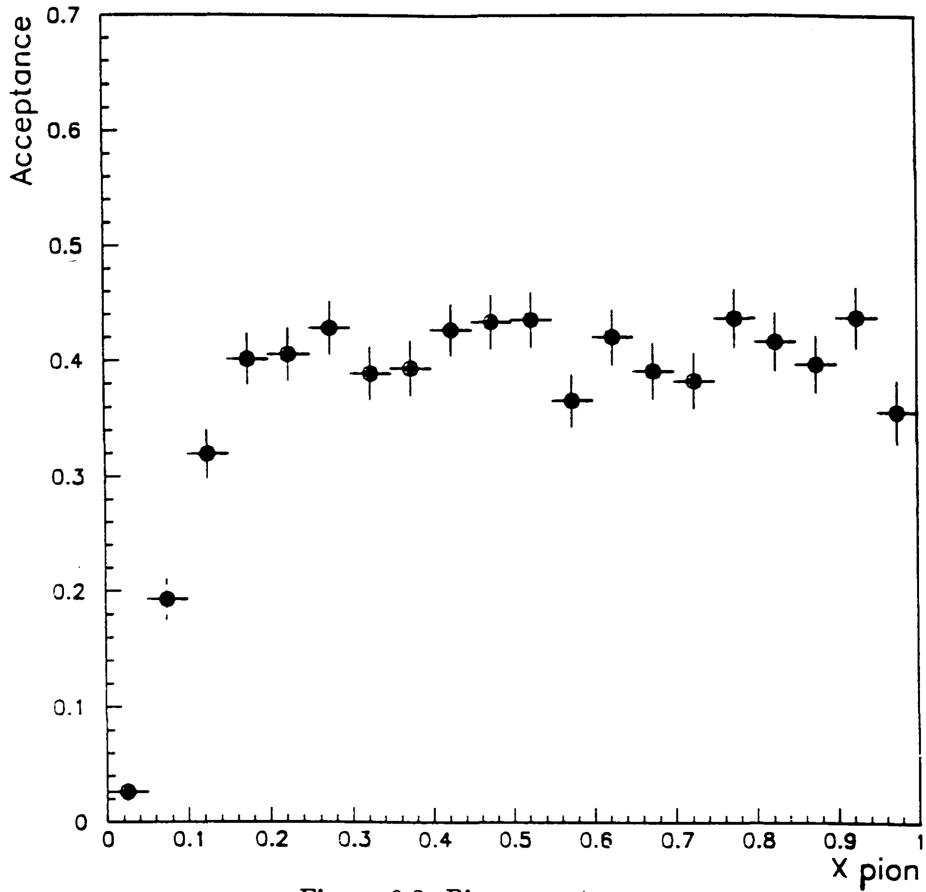

Figure 6.2: Pion acceptance

- in this region there is a high background and the acceptance is low and rapidly changing,
- low energy pions are not as correctly simulated as others

The polarization was obtained from a linear fit to the using the formula

$$\frac{1}{N}\frac{dN}{dx_\pi} = 1 + 2P(x_\pi - \frac{1}{2}). \tag{6.3}$$

The corrected pion spectrum and linear fit to the spectrum are shown in Fig.6.3. The resulting polarization was found to be -0.210 ± 0.075 where the quoted error is due to statistics only.

The maximum likelihood fitting procedure

The reconstructed pion spectra ($\frac{1}{n}\frac{dn}{dx_\pi}$) for both negative and positive helicities can be obtained from Monte Carlo data.

$$\frac{1}{n}\frac{dn_+(x_\pi)}{dx_\pi} = \psi_+(x_\pi) \qquad ; \qquad \frac{1}{n}\frac{dn_-(x_\pi)}{dx_\pi} = \psi_-(x_\pi)$$

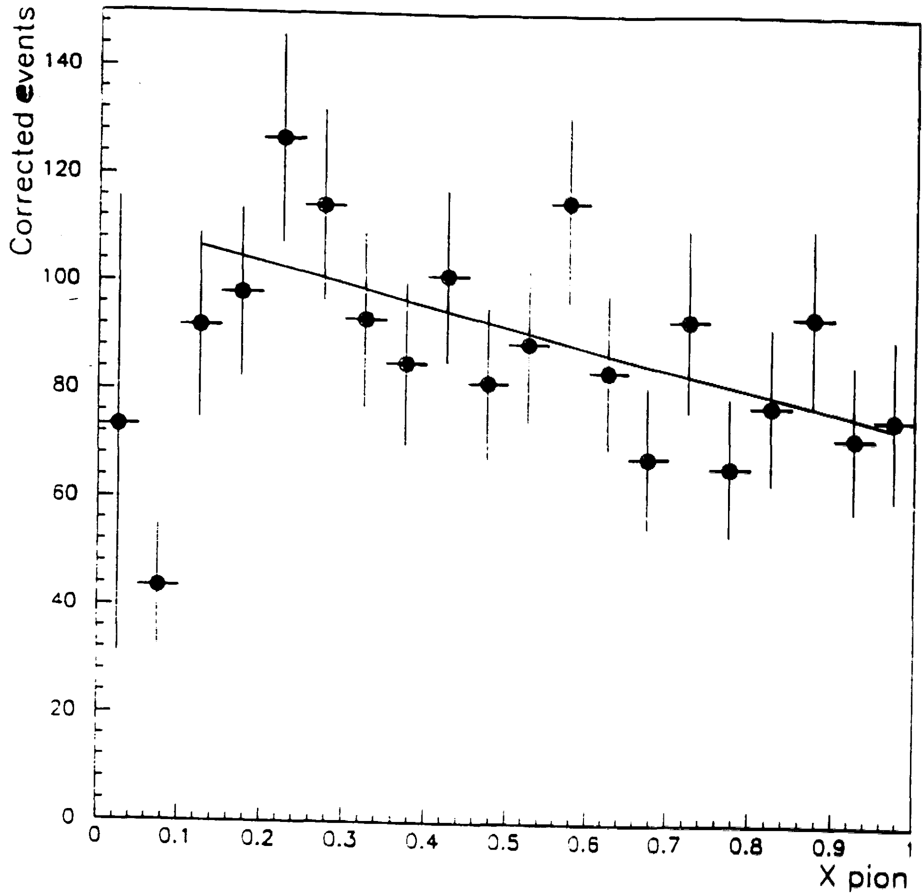

Figure 6.3: The corrected pion fractional momentum spectrum

Monte Carlo samples of $Z^0 \to \tau^+\tau^-$ events were generated at different beam energies and weighted according to the number of $Z^0 \to hadrons$ observed at each energy in the data.

The positive and negative helicity contributions to the reconstructed x_π-distributions, $\psi_+(x_\pi)$ and $\psi_-(x_\pi)$ respectively, are related to the experimental distribution $\chi(P, x_\pi)$ through the following formula[59]:

$$\chi(P, x_\pi) = N(P)\left(\frac{1+P}{1+P_0}\psi_+(x_\pi) + \frac{1-P}{1-P_0}\psi_-(x_\pi)\right) \tag{6.4}$$

where P_0, the tau polarization value in the Monte Carlo ($P_0 = -0.152$), is defined as

$$P_0 = \frac{N^+_{gen} - N^-_{gen}}{N^+_{gen} + N^-_{gen}} \tag{6.5}$$

Here N^+_{gen}, N^-_{gen} are the number of generated events with positive and negative helicities respectively,

$$N(P) = \frac{1}{\sum_{x_\pi \geq 0.2} \chi(P, x_\pi)}$$

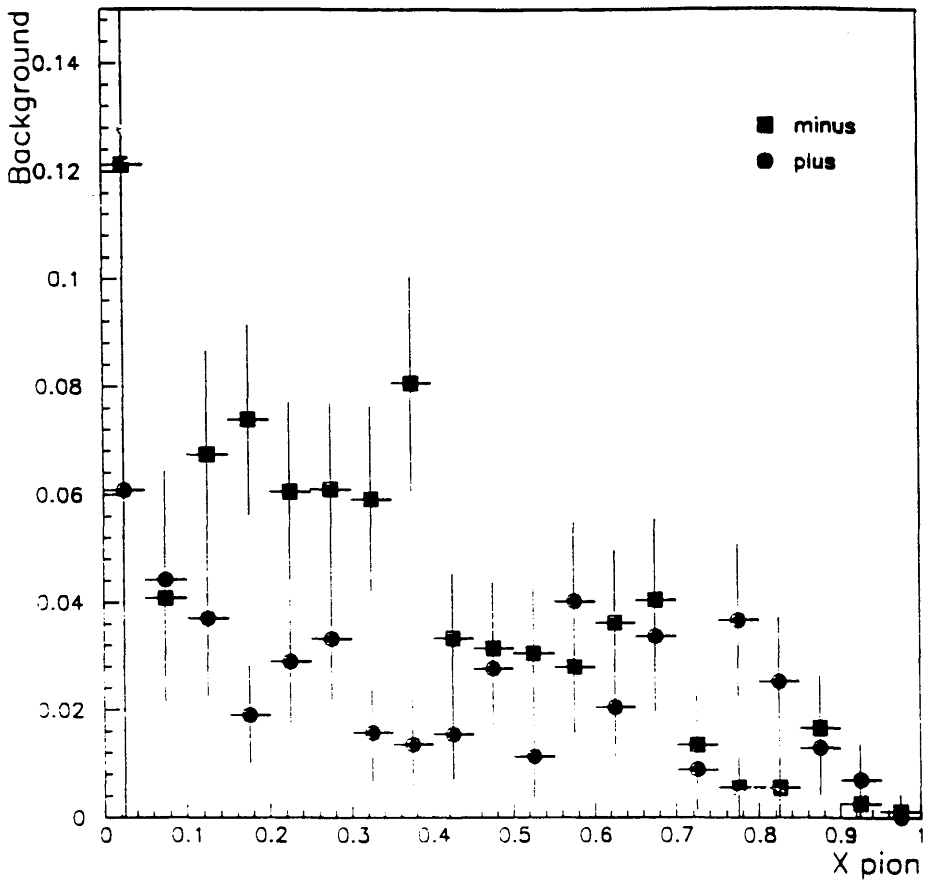

Figure 6.4: Background fraction to the pion positive and negative helicity spectra

is the normalization. The Monte Carlo distributions after pion selection, $\psi_+(x_\pi)$ and $\psi_-(x_\pi)$, include background,acceptance and radiative correction effects. The background is plotted separately for the two distributions in Fig.6.4. There is a clear indication that the fractional background in $\psi_-(x_\pi)$ is higher than that in $\psi_+(x_\pi)$, particularly at low x_π. A possible explanation for such a difference is the fact that the background from misidentified tau decays is polarized, and for leptonic decays the contribution to the momentum spectra from negative is higher than that from positive helicity. This background was estimated from Monte Carlo simulation for each tau helicity possibility.

In the data the pion spectrum is corrected by subtraction of contributions from electron and muon pairs. Background from misidentified tau decay channels is kept, assuming it to be polarized as expected, unlike that from electron and muon pairs. A maximum likelihood fit of the data to the sum of the two reconstructed spectra of positive and negative helicities described above yielded a polarization of -0.140 ± 0.077. The three distributions are displayed in Fig.6.5. Adding in quadrature the statistical and systematic errors which are summarized in table 6.2 gives a total error of ± 0.093.

The pion selection criteria are mainly based on two important calorimetric cuts applied to the ECAL and HCAL data. The errors were estimated using real pions from test beam

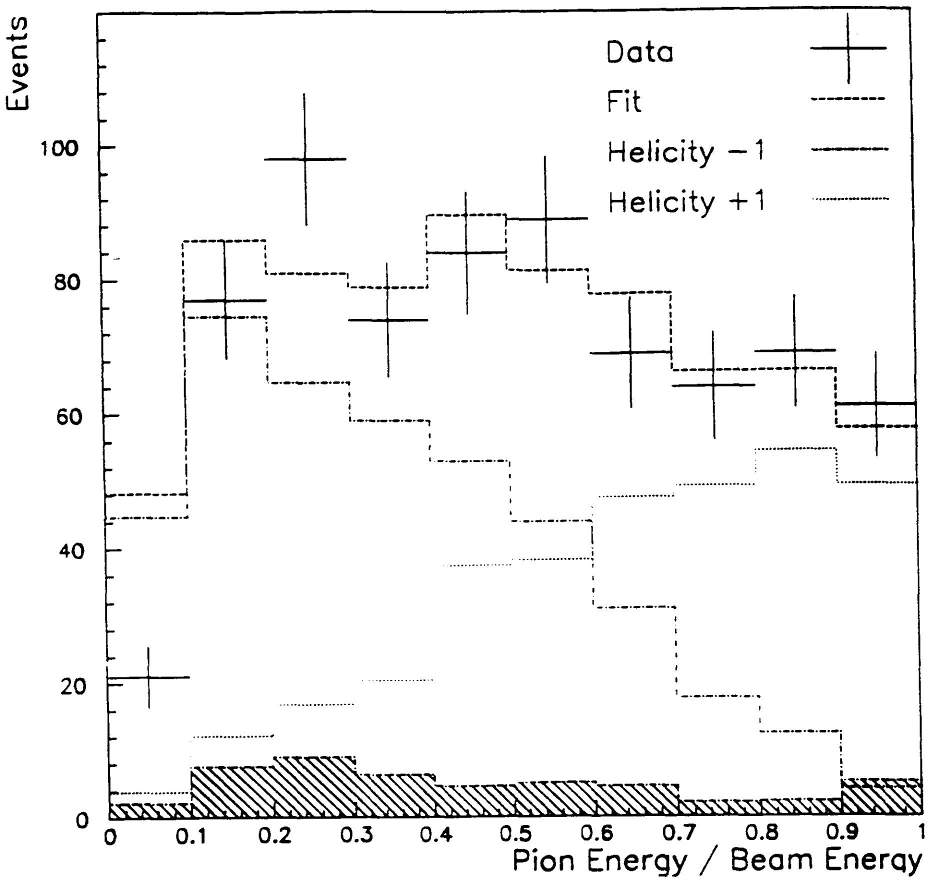

Figure 6.5: Pion spectra with the fit, the shaded area represents the background

Source of systematic error	Value
ECAL cut	0.033
HCAL cuts	0.021
Background	0.030
MC statistics	0.021
Combined	0.053

Table 6.2: Summary of the systematic errors in the polarization P

data for ECAL and those from the decay $\tau \rightarrow \rho\nu$ for HCAL. Both ECAL and HCAL errors were estimated from the acceptances using both data and Monte Carlo events. Checks were made of the sensitivity to the cuts by varying the cuts by $\pm 10\%$. The systematic error in the background is estimated by determining the effect of the variation on the resulting polarization. Systematic errors resulting from uncertainties in the branching ratios are included in the background variation and its effect on polarization.

The reported value of tau polarization from the ALEPH tau group, averaging over all

Experiment	Decay mode	Polarization
ALEPH	$\tau \to e\nu_e\nu_\tau$	$-0.36 \pm 0.17 \pm 0.06$
	$\tau \to \mu\nu_\mu\nu_\tau$	$-0.19 \pm 0.13 \pm 0.06$
	$\tau \to \pi(K)\nu_\tau$	$-0.130 \pm 0.065 \pm 0.044$
	$\tau \to \rho\nu_\tau$	$-0.124 \pm 0.047 \pm 0.051$
	$\tau \to A1\nu_\tau$	$-0.15 \pm 0.15 \pm 0.07$
Combined		-0.152 ± 0.045
OPAL	$\tau \to e\nu_e\nu_\tau$	$+0.20 \pm 0.13 \pm 0.08$
	$\tau \to \mu\nu_\mu\nu_\tau$	$-0.17 \pm 0.16 \pm 0.10$
	$\tau \to \pi(K)\nu_\tau$	$-0.08 \pm 0.10 \pm 0.07$
Combined		-0.01 ± 0.09
CELLO	$\tau \to \pi\nu_\tau$	-0.01 ± 0.22
MAC	$\tau \to \pi\nu_\tau$	-0.02 ± 0.06
This analysis	$\tau \to \pi\nu_\tau$	$-0.140 \pm 0.077 \pm 0.053$

Table 6.3: Summary of the polarization measurements

τ-decay channels, is -0.152 ± 0.045 [71]. A summary of results from different experiments is given in table 6.3.

6.2 The Extraction of the Standard Model Parameters

In the framework of the improved Born approximation[64], the tau polarization can be expressed in terms of the running coupling constants $v_\tau(\mu^2)$ and $a_\tau(\mu^2)$ at $\mu = m_z$, replacing v_τ and a_τ in the tree level formula

$$P = -2\frac{v_\tau/a_\tau}{1+(v_\tau/a_\tau)^2} \tag{6.6}$$

Using $P = -0.140 \pm 0.093$ one obtains

$$v_\tau(M_Z^2)/a_\tau(M_Z^2) = 0.071 \pm 0.045. \tag{6.7}$$

The relation $v_\tau(M_Z^2)/a_\tau(M_Z^2) = 1 - 4(sin^2\bar{\theta}_W(M_Z^2) + C)$, where $C = 0.0007$ accounts for the flavour dependent weak corrections[65], and $\bar{\theta}_W$ is the effective value of θ_W, results in a value

$$sin^2\bar{\theta}_W(m_Z^2) = 0.232 \pm 0.009. \tag{6.8}$$

Combining this result for v_τ/a_τ with the measurements of the partial width of the decay $Z \to \tau^+\tau^-$ from this experiment, $\Gamma_\tau = (82.3 \pm 1.6) MeV$[66], one can separate v_τ and

Experiment	$sin^2\theta_W$	v_τ/a_τ	v_τ	a_τ
ALEPH	0.2302 ± 0.0058	0.076 ± 0.023	-0.038 ± 0.012	-0.497 ± 0.005
OPAL	0.237 ± 0.009	0.01 ± 0.04		
Lower energies			$-0.09^{+0.25}_{-0.28}$	-0.484 ± 0.034
This analysis	0.232 ± 0.009	0.071 ± 0.045	-0.035 ± 0.021	-0.497 ± 0.005

Table 6.4: Summary of the electroweak parameter measurements

a_τ. Using the partial width formula

$$\Gamma_\tau = \frac{G_F M_Z^3}{6\sqrt{2}\pi}(v_\tau^2(M_Z^2) + a_\tau^2(M_Z^2)) \tag{6.9}$$

and assuming a_τ is negative , one obtains

$$\begin{aligned} v_\tau(M_Z^2) &= -0.035 \pm 0.021 \\ a_\tau(M_Z^2) &= -0.497 \pm 0.005 \end{aligned} \tag{6.10}$$

Chapter 7

Summary and Conclusions

The tau polarization in the decay $Z^0 \to \tau^+\tau^-$ and subsequent tau decays in the $\tau \to \pi\nu$ channel has been studied using the ALEPH detector at the LEP collider. The polarization in general is a result of parity violation in the weak interactions. Polarization in tau lepton decays is reflected in the momentum spectrum of the tau decay products. The motivation for its measurement is the confirmation of the Standard Model predictions.

A sample of tau events was first selected according to the topology and kinematics of the tau lepton decays. An efficiency of 71% was achieved with a background of 5%. In the analysis of the pion decay channel, sources of the background were mainly from other tau decay modes, principally K^*, ρ and μ modes. The overall pion acceptance was 37% with a background of less than 5% (see chapter 5). The τ polarization

$$P = \frac{\sigma_R^\tau - \sigma_L^\tau}{\sigma_R^\tau + \sigma_L^\tau} \tag{7.1}$$

measured from the corrected spectrum of the pion momentum, yielded a result of $-0.140 \pm 0.077 \pm 0.053$ for the tau polarization where the first error is statistical while the second is systematic.

Detector effect contributions to the measured tau polarization were found to be small compared to the statistical errors.

The present results based on about 200K Z^0 events are in good agreement with the official ALEPH results for the decay $\tau \to \pi\nu$ [71], and with those reported by OPAL [72]. Previous polarization measurements reported by the MAC and CELLO collaborations were performed at much lower energies than those of LEP, where the virtual Z^0 exchange is not dominant over the photon exchange in the $e^+e^- \to \tau^+\tau^-$ interaction. The relatively small event samples in these measurements prevent a precise measurement for the lepton couplings to the weak neutral current represented by the Z^0 boson.

The dominant contribution to the error in this measurement comes from the uncertainties of pion misidentification. The error in the polarization measurement can be reduced further through continuing improvements in the particle identification. A better control of systematic errors will probably be achieved from correlation studies in tau decays, particularly in tau polarization measurements which include such correlations between the τ^+ and τ^- decay products. The additional Z^0 data collected by the ALEPH detector will provide much better statistics and will increase the chances of success of such studies.

The ALEPH value differs from zero by more than three standard deviations when the value of polarization is averaged over all tau decay channels. This observation of a non-zero polarization in e^+e^- interactions implies

- parity is violated in the process $e^+e^- \rightarrow \tau^+\tau^-$,
- parity is violated in the decay $\tau \rightarrow \pi\nu_\tau$, without which the τ polarization could not be observed.

This finding in τ decays confirms the recent observation in the decay $\tau \rightarrow 3\pi\nu_\tau$[67]. Parity violation in weak neutral currents has been observed in inelastic polarized electron scattering[68] and in atomic transitions[69]. Its observation in charged tau decays is in agreement with the universality of the electroweak theory.

In the framework of the Standard Model, the polarization is directly related to the ratio of the vector and axial vector couplings of the tau lepton to the Z^0, and hence to the effective electroweak mixing angle $sin^2\bar{\theta}_W$.

$$sin^2\bar{\theta}_W = 0.232 \pm 0.009 \tag{7.2}$$

A smaller error was achieved by ALEPH by combining the results from all tau decay channels. Hence, $sin^2\bar{\theta}_W$ was measured with better sensitivity and higher statistics than in other measurements with which it is, however, in good agreement[66]. The overall error will be reduced further with the analysis of data collected in 1991 (320K Z^0 events). Since these data will probably also provide more understanding of systematic effects, a reduction of the systematic error seems likely. For an improvement in systematic error in the measured polarization from 0.053 to 0.03, say, the limiting precision in the value of $sin^2\bar{\theta}_W$ would be ± 0.0039. With only 3M Z^0 events, say, the statistical error in P of 0.02 would increase this error in $sin^2\bar{\theta}_W$ to $\pm 0,0046$.

The ultimate accuracy for $sin^2\theta_W$ will come from its measurement using polarized beams at LEP. For example, a 50% longitudinal polarization of the colliding beams has been claimed to be sufficient to determine $sin^2\theta_W$ to ± 0.00035 [73].

The consistency of values for $sin^2\bar{\theta}_W$ obtained from a varied range of experimental studies including deep inelastic neutrino scattering lend ever stronger support to the Standard Model. (Detailed comparison of the different measured $sin^2\bar{\theta}_W$ values is often complicated by the variety of definitions of $sin^2\theta_W$.

Combining the value of $sin^2\bar{\theta}_W$ with the partial width of Z^0 decay into tau leptons the vector and axial vector couplings of the tau leptons are measured and found to be $v_\tau = -0.035 \pm 0.021$ and $a_\tau = -0.497 \pm 0.005$. The combined analysis of all experiments at lower energies yields $v_\tau = -0.09^{+0.25}_{-0.28}$ and $a_\tau = -0.484 \pm 0.034$[70]. Comparing the LEP results to similar measurements at lower energies, the improvement in precision in the present experiment is therefore about an order of magnitude.

Bibliography

[1] M. Breidenbach et al., Phys. Rev. Lett. 23(1969)935

[2] P.B.Schwinberg, R.S. Van Dyck and H. G. Dehmelt, Phys. Rev. Lett. 47(1981)1679

[3] T.Kinoshita and W.B. Lindquist, Phys. Rev. Lett. 47(1981)1573

[4] F.J. Hasert et al., Phys. Lett. 46B(1973)121, Phys. Lett. 46B(1973)138

[5] G.Arnison et al., Phys. Lett. 112B(1983)103, Phys. Lett. 126B(1983)398

[6] M. Banner et al., Phys. Lett.122B (1983) 476, P. Bagnaia et al., Phys. Lett. 129B(1983)130
S.L. Glashow, Nucl. Phys. 22, 579(1961)
S.Weinberg, Phys. Rev. Lett. 19, 1264(1967)
A.Salam, in Elementary Particle Theory, ed. N.Svartholm(Almqvist and Wiskell, Stockholm, 1968), p.367.
S.L.Glashow, J.Illiopoulos, L.Maiani, Phys. Rev. D2,(1970)1285

[7] E. Fermi, Z. Phys. 88(1934)161

[8] C.S.Wu et al., Phys. Rev. 105(1957)1413

[9] R.P. Feynman and M.Gell-Mann, Phys. Rev. 109(1958)193
R.P. Feynman and M.Gell-Mann, Theory of Fermi interaction, Phys. Rev. 110(1958)1178

[10] T.D.Lee and C.N. Yang, Phys. Rev. 104(1956)254

[11] G. Gamow and E. Teller, Phys. Rev. 49 (1936)895

[12] C.H.Llewellyn-Smith, Phys. Rep. 3(1972)261

[13] F. Halzen and A. Martin "Quarks and Leptons", (John Wiley and Sons 1984)
I.J.R. Aitchison and A.J.G. Hey, "Gauge Theories in Particle Physics", (Adam Hilger, Bristol, 1982)

[14] N. Cabibbo , Phys. Rev. Lett., 10(1963)531

[15] M. Kobayashi and T. Maskawa, Prog. Theo. Phys. Japan 49(1973)652

[16] S.Glashow, Nucl. Phys. 22(1961)579

[17] P.W.Higgs Phys. Rev. 13(1964)508

[18] G. t′ Hooft, Nucl. Phys. B33,175,1971, Phys. Rev. D4,(1971)2821

[19] E.S.Abers and B.W.Lee, Phys. Rep. 9C(1)(1973)1.

[20] F. Berends and A. Bohm, in "High Energy Electron-Positron Physics", eds.A. Ali, P. Soding (World Scientific, Singapore 1988)27

[21] M.L.Perl et. al, Phys. Rev. lett. 35(1975)1489

[22] Y.S. Tsai, Phys. Rev. D4(1971)2821

[23] H.B. Thacker and J.J. Sakurai, Phys. Lett. 36B(1971)103

[24] F.J.Gilman and S.H. Rhie, Phys. Rev. D31(1985)1066

[25] M. Derrick et al., Phys. Lett. 189B(1987)260

[26] H. Albrecht et al., DESY preprint 87-148, 1987

[27] Christian Kiesling, in "High Energy Electron-Positron Physics", eds.A. Ali, P. Soding (World Scientific, Singapore 1988)177

[28] B.C.Barish and R. Stroynowski, Phys. Rep., 157, No.1(1988)1

[29] K.K. Gan, Proc. of the Fifteenth SLAC Summer Institute on Particle Physics (1987) P573

[30] The Particle Data Group, Review of Particle Properties 1990, Phys. Lett. B239(1990)

[31] B.G. Bylsma et al.,(HRS collaboration), Phys. Rev. D35(1987)2269

[32] J. Field and B.Richter, CERN 76-18(1976)

[33] J. Augustin, F. Renard, Nucl. Phys. B 162,(1980)109

[34] CELLO Collaboration, H.J.Behrend et al., Phys. Lett. B127(1983)
MAC Collaboration, W.T. Ford et al., Phys. Rev. D36(1987)1971
AMY Collaboration, M.H.Lee et al., KEK Preprint 90-70(1990)

[35] S.Jadach and Z.Was, "Z Physics at LEP", CERN 89-08, Volume 1 (1989)235

[36] G.Goggi, "Proceedings of the LEP Summer Study", CERN 79-01(1979)499

[37] Z.Was, Acta Physica Polonica B18(1987)12.

[38] F. Boillot and Z. Was, Z. Phys. C 43 (1989)109

[39] Z line shape, "Z physics at LEP" Volume 1 (1989)89

[40] "Measurements of tau branching ratios", ALEPH Collaboration, To be submitted to Z Physics

[41] P.Holl et al., Nucl. Instr. and Meths., A257(1987)587

[42] G.J. Barber et al., Nucl. Instr. and Meths., A279(1989)212

[43] S.R. Amendolia et al., Nucl. Instr. and Meth. A252(1986)392

[44] D. R. Nygren, PEP198(1975)

[45] "The ALEPH Collaboration Handbook", ALEPH Internal note, 89-77(1989)

[46] D. Decamp et al., Nucl. Instr. and Meths., A249(1990)121

[47] W.Atwood et al., CERN PPE 91-24(1991) Submitted to Nucl. Instr. and Meths., A

[48] W. von Ruden, "The ALEPH DAQ system", contributions to the "real Time, 89" Conference, Williamsburg, Virginia(May 1989), ALEPH Internal note 89-116 (1989).

[49] "The BOS system Dynamic Memory Management", DESY Internal report R1-88-01, (1988)

[50] ALEPH Internal note 86-110(1986)

[51] ALEPH Internal note 87-53(1987),88-119(1988)

[52] S. Jadach, et al., "The Monte Carlo Program KORALZ, version 3.8 for lepton and quark pair production at LEP/SLC energies", CERN-TH-4994/91 1991

[53] J. Knobloch and P. Norton, ALEPH Internal note, 88-46(1988)

[54] ALEPH Internal note 87-9(1987)

[55] M.Bengtsson and T. Sjöstrand, Phys. Lett. B 185(1987)121

[56] H. Meinhard, Presentation at the electroweak meeting note in preparation

[57] D.Decamp et al., Phys. Lett. 235B(1990)399.

[58] G.Bagliesi and L. Silvestris, "The Tau Trigger", ALEPH internal note 91-2, (1991)

[59] ALEPH Internal note, ALEPH 90-188(1990), ALEPH 90-15(1990)

[60] G.Bagliesi et al., Nucl. Inst. and Meth., A286(1990)61

[61] ALEPH internal comunications

[62] ALEPH internal comunications

[63] W.Wiedenmann, ALEPH analysis meeting, Oct. 1990.

[64] M.Consoli, W.Hollik, and F.Jegerlehner, in "Z Physics at LEP", CERN Report 189-08 Volume 1 (1989)7

[65] D.Bardin, W. Hollik, and T. Riemann, Z. Phys. C49(1991)485

[66] ALEPH Collaboration, D.Decamp et al., Submitted to Z. Phys. C.

[67] H. Albrecht et al., Phys. Lett. B250(1990)164

[68] C.Prescott et al., Phys. Lett. B77(1978).

[69] L.M. Barkov and M.S. Zolotrev, JETP Lett. 31(1978)357, Phys. Lett. B85 (1979)308

[70] S.Odaka, Workshop on Tau Lepton Physics, Orsay, 24-27 September 1990;see also KEK Preprint 90-164(1990)

[71] ALEPH Collaboration, D.Decamp, Submitted to Phys. Lett. B.

[72] OPAL Collaboration,G. Alexander, et al., Submitted to Phys. Lett. B.

[73] A.Blondel, Polarization at LEP, CERN-EP/90-21(1990)